UNIVERSITÀ DEGLI STUDI DI BERGAMO
FACOLTÀ DI INGEGNERIA
Corso di dottorato di ricerca in **Meccatronica e tecnologie innovative**
$XXIII^{\circ}$ Ciclo

Investigation on the dynamic performances of piezoelectric multilayer actuators

Coordinatore

Chiar.mo Prof. Riccardo Riva

Tutor

Chiar.mo Prof. Roberto Strada

Tesi di Dottorato di

Mauro FORLANI

Matr. 26621

Anno Accademico 2010/2011

A Sara

AKNOWLEDGEMENTS:

This work is the result of slightly more than three years of research, during which several people gave their contribution. First and foremost I would like to thank my tutor Prof. Roberto Strada who has been providing constant support and encouragement, besides precious advice and help. He has been definitely more than a tutor. My gratitude goes to Prof. Paolo Righettini, the main inspirer of this work. His observations, comments, and suggestions shaped this work more than anything else. I would like to thank Prof. Vittorio Lorenzi for his patience in removing all my doubts about finite elements techniques, I know I have been exhausting and I apolgize for that. The contribution of Prof. Giacomo Gigante in the analytical modelling has been foundamental too: thank you very much.

A special mention must be made for all the colleagues and fellow students who made these three years of PhD a memorable experience. In particular I would like to thank Prof. Riccardo Riva, Prof. Bruno Zappa, Alberto, Michele, Paolo, Andrea e Fabio.

Un grazie incommensurabile va alla mia famiglia, che mi è sempre stata vicina supportandomi, spronandomi, consigliandomi e stimolandomi. Qui non ci sono arrivato con le mie sole gambe: ho montato sulle vostre spalle.

Questo lavoro è dedicato a Sara, per lei un grazie non basta.

Contents

Introduction **17**

Nomenclature **25**

1 Piezoelectric thin plates **27**

1.1 Single plate dynamics 28

1.1.1 Unconstrained plate 30

1.1.2 Inertially loaded unconstrained plate 31

1.1.3 Constrained plate 33

1.1.4 Inertially loaded constrained plate 34

1.2 Driving circuit 35

1.3 Simulations and commentary 36

2 Finite difference modelling **43**

2.1 Numerical analysis of single plate dynamics 43

2.2 Boundary and initial conditions formulation 46

2.2.1 Unconstrained plate 46

2.2.2 Inertially loaded unconstrained plate 47

2.2.3 Constrained plate 48

2.2.4 Inertially loaded constrained plate 49

2.3 Simulations and commentary 49

2.3.1 FRF estimation 50

3 Piezoelectric multilayer actuators **57**

3.1 Multilayer actuator modelling 57

3.1.1 Multilayer statics 58

3.2 System's description 59
3.3 Hypotheses 59
3.4 Formulation of the equations 60
  3.4.1 Dynamic equations 60
  3.4.2 Boundary and initial conditions 60
  3.4.3 Boundary equations formulation 61
3.5 Solution 63
  3.5.1 Positive parameter 64
3.6 Physical quantities 67
  3.6.1 Stress 68
  3.6.2 Electric displacement, charge, and current 68
3.7 Electric circuit 68
3.8 Parametric analysis 70
  3.8.1 Parameters estimation 70
  3.8.2 Influence of system's parameters 72
  3.8.3 Comparison with bulk modelling 77

4 Finite difference modelling of piezoelectric MLAs 83

4.1 Multilayer dynamics 84
4.2 Constrained actuator 85
  4.2.1 Electric circuit for multilayer actuator 86
4.3 Transient dynamics of a piezoelectric MLA 87

5 Test bench design 93

5.1 Test bench model 93
  5.1.1 Test bench simulations 95
5.2 Amplifier design 96
  5.2.1 Calibration 99
5.3 Sensors 102
5.4 Mechanical load 103

6 Experimental analysis and models validation 105

6.1 Experimental set-up 105
  6.1.1 Description of the instrumentation 105
  6.1.2 Measuring methodology 106
6.2 Static behavior 106

6.3 Quasi-static behaviour . . . 108
6.4 Dynamic behaviour . . . 110
6.5 Comparison with numerical data . . . 114

Conclusions **121**

A Non-linear theory of electroelasticity for strong fields **125**
A.1 Kinematics of a deformable body . . . 127
A.1.1 Coordinate systems . . . 127
A.1.2 Displacements . . . 128
A.1.3 Velocity and acceleration . . . 131
A.2 Balance laws . . . 132
A.2.1 Interactions . . . 132
A.2.2 Gauss's law . . . 133
A.2.3 Faraday's law . . . 133
A.2.4 Conservation of mass . . . 134
A.2.5 Conservation of linear momentum . . . 134
A.2.6 Conservation of angular momentum . . . 135
A.2.7 Conservation of energy . . . 136
A.2.8 Electrostatic stress tensor and total stress tensor . . . 136
A.2.9 Free energy . . . 137
A.2.10 Material form of the balance laws . . . 138
A.3 Constitutive equations . . . 141
A.4 Initial-boundary-value problem . . . 141

B Linear Piezoelectricity **143**
B.1 Constitutive equations . . . 143
B.2 Dynamic equations . . . 143
B.3 Compressed matrix representation . . . 144
B.4 Relation between material constants . . . 145
B.5 The elasto-piezo-dielectric matrix . . . 145
B.6 Constitutive and dynamic equations . . . 146
B.7 Slender rod in axial mode . . . 147
B.7.1 Electromechanical coupling coefficient . . . 148
B.8 Thin plate in stretch mode . . . 152
B.8.1 Coupling coefficient of a thin plate . . . 152

C Piezoelectric ceramics **157**

Bibliography **159**

List of Figures

1 Articles regarding smart materials - 2008/2010 comparison 19
2 Smart materials employed in actuation - 2008/2010 comparison 20
3 Example of piezoelectric multilayer actuator. Courtesy of [23]. 21

1.1 Unconstrained plate model 27
1.2 Unconstrained plate with inertial load model 32
1.3 Constrained plate 33
1.4 Constrained plate with additional mass 34
1.5 Driving circuit of the piezoelectric actuator 36
1.6 Strain FRF for different constraints and loading conditions 37
1.7 Current FRF for different constraints and loading conditions 38
1.8 Strain FRF when considering an electric resistance 39
1.9 Current FRF when considering an electric resistance 40
1.10 Current FRF comparison: with and without resistive load 40
1.11 Voltage across piezoelectric actuator FRF 41

2.1 Thin plate spatial discretization 44
2.2 Thin plate model convergence 50
2.3 CPU time as element number increases 51
2.4 1 V half sine pulse 52
2.5 1 V half sine pulse - FFT 53
2.6 Unloaded constrained plate - Strain FRF comparison between BKM and FDM 53
2.7 Unloaded constrained plate - Current FRF comparison between BKM and FDM 54
2.8 Inertially loaded constrained plate - Strain FRF comparison between BKM and FDM 54

2.9 Inertially loaded constrained plate - Current FRF comparison between BKM and FDM 55

3.1 Plate-electrode configurations 58

3.2 Solutions for relieving stress and electric field concentrations 58

3.3 Multilayer actuator and loading conditions 59

3.4 Driving circuit for a piezoelectric actuator 69

3.5 Multilayer actuator cross-sectional view. Please notice that this image is only qualitative. 72

3.6 Frequency response as electrodes mass varies: the solid line shows the frequency response when the influence of electrode mass is disregarded. The dashed and dash-dotted ones are the result of the actuator's dynamics when the electrodes thickness is respectively one tenth and one fifth of the layer thickness. In these simulations the load stiffness k and the load mass m were set to zero. 73

3.7 Frequency response as load stiffness varies: the solid line shows the frequency response of the unloaded actuator's dynamics when the stiffness constant k was set to zero. The dashed and dash-dotted ones are the result of the actuator when k is set to respectively 0.1 k_{MLA} and k_{MLA}, being k_{MLA} the axial stiffness of the piezoelectric actuator at constant electric field. 74

3.8 Frequency response to a sinusoidal voltage as the actuator length varies: the red areas are found in correspondence of the resonance peaks. 75

3.9 First natural frequency of the piezoelectric actuator versus the actuator length H; several curves are plotted for various values of the normalized inertial load mass k_m. 76

3.10 First natural frequency of the piezoelectric actuator versus the normalized inertial load mass k_m; several curves are plotted for various values of the actuator length H. 76

3.11 Frequency response of an unloaded multilayer actuator: the solid line shows the frequency response of the MLA modelled by BKM. The dashed line is the result of the MLM. 77

3.12 Frequency response of a loaded multilayer actuator: the solid line shows the frequency response of the MLA modelled by BKM. The dashed line is the result of the MLM. The actuator is loaded by an inertial load whose mass equals that of the actuator. 78

3.13 First natural frequency of the piezoelectric actuator as the number of layers L and the normalized inertial load mass k_m vary. 79

3.14 Second natural frequency of the piezoelectric actuator as the number of layers L and the normalized inertial load mass k_m vary. 80

3.15 Third natural frequency of the piezoelectric actuator as the number of layers L and the normalized inertial load mass k_m vary. 80

3.16 Reduction of frequency range of use of the piezoelectric actuator due to stress limitations. The curves shows the frequency reduction with respect to the 1^{st} natural frequency versus the actuator length H; several curves are plotted for various values of the normalized inertial load mass k_m. 81

4.1 Discretization in finite elements of a piezoelectric multilayer actuator 83

4.2 Model of a constrained multilayer actuator; the figure shows the loading conditions, featuring stiffness, damping, and inertia. Furthermore a time-dependent force can be applied. 85

4.3 Convergence of MLA dynamics: first resonance frequency and amplitude of displacement 88

4.4 Response to a step voltage as load mass varies. The normalized load mass coefficient k_m in the three cases is 0.1, 1, and 10. The circuit resistance R is set to zero. 89

4.5 Displacement response to a step voltage as load mass varies. The circuit resistance R is set to 1 Ω. 90

4.6 Capacitance response to an input step voltage as load mass varies. $V_s = 1$ V, $R = 1\ \Omega$ 91

4.7 Current response to a step voltage as load mass varies. The circuit resistance R is set to 1 Ω. 92

5.1 Test bench model 94

5.2 Displacement/Acceleration FRF, $k_m = 0.25, 10$ 95

5.3 Current/stress on piezo FRF, $k_m = 0.25, 10$ 96

5.4 Amplifier electric scheme 97

5.5 Amplifier 98

5.6 Voltage measuring set-up 99

5.7 Open loop output voltage 100

5.8 Open loop voltage readings 100

5.9 Voltage dividers gain 100
5.10 Current measuring set-up 101
5.11 Current flowing into circuit 101
5.12 Frequency response function of supplied voltage 102
5.13 Frequency response function of supplied current 103
5.14 Test bench set-up 104

6.1 MLA displacement under large voltage excitation. Sampling frequency 2048 Hz 107
6.2 Half period of MLA displacement under large voltage excitation. Sampling frequency 2048 Hz 107
6.3 Relation between voltage and displacement for large signal excitation 108
6.4 Electrical quantities in a 24 V p-p 10 Hz sine excitation 109
6.5 Relation between capacitance and voltage at low frequencies 109
6.6 Current FRF in the range 200 Hz - 20 kHz, $k_m = 0.25$. Voltage amplitude 0.12 V, sampling frequency 102.4 kHz, sweep time 10 s. 111
6.7 Current FRF in the range 200 Hz - 20 kHz, $k_m = 0.63$. Voltage amplitude 0.12 V, sampling frequency 102.4 kHz, sweep time 10 s. 112
6.8 Current FRF in the range 200 Hz - 20 kHz, $k_m = 6.3$. Voltage amplitude 0.15 V, sampling frequency 102.4 kHz, sweep time 10 s. 113
6.9 Acceleration FRF in the range 200 Hz - 1 kHz, $k_m = 0.63$. Voltage amplitude 1 V, sampling frequency 20.48 kHz, sweep time 15 s. 113
6.10 Acceleration FRF in the range 200 Hz - 1 kHz, $k_m = 6.3$. Voltage amplitude 1 V, sampling frequency 20.48 kHz, sweep time 15 s. 114
6.11 Acceleration FRF in the range 1 kHz - 20 kHz, $k_m = 0.63$. Voltage amplitude 0.12 V, sampling frequency 102.4 kHz, sweep time 10 s. 115
6.12 Acceleration FRF in the range 1 kHz - 20 kHz, $k_m = 6.3$. Voltage amplitude 0.15 V, sampling frequency 102.4 kHz, sweep time 10 s. 115
6.13 Current FRF - no external inertial load ($k_m = 0.25$) 117
6.14 Current FRF - external inertial load $m = 2$ g, ($k_m = 0.63$) 118
6.15 Current FRF - external inertial load $m = 70$ g, ($k_m = 6.3$) 118

A.1 Description of a deformable body 127
A.2 Simplified description of a deformable body 129

B.1 The `4mm` elasto-piezo-dielectric matrix non-zero entries 146
B.2 Rod model 147

B.3 Mechanically loaded piezoelectric rod 149
B.4 Electrically loaded piezoelectric rod 150
B.5 Thin plate model 152
B.6 Mechanically loaded piezoelectric thin plate 153
B.7 Electrically loaded piezoelectric thin plate 155

Introduction

Created to improve men's ability to exploit the surrounding environment, machines contributed to differentiate men from the other living creatures who roamed planet Earth. Machines gave men an edge over competiting species, allowing them to secure more food and water, to travel long distances, to make clothes, weapons, etc. The evolution of machines is thus strickly connected with that of mankind.

The question whether machines were the result of an active process of human thinking or the fortunate outcome of some coincidence is not relevant: either ways the ability of men was to make use of that finding in order to solve a problem and to reduce the daily burden for survival. Early machines were conceived to be operated by men themselves: first and foremost the lever comes into mind, a powerful mean to amplify human force.

As soon as men became organized in larger groups technology and machines underwent a formidable evolution thanks to the possibility of having specialized professional figures who spent their time working on technological improvements [6]. New developments see the machines interacting with the environment, harvesting energy from natural power sources such as wind and water. These machines had no longer to be man (or horse) -sized, since input power was not provided anymore from men nor animals. This change is of paramount importance because introduces the concept of scaling and paves the way to modern machines: once energy can be introduced, it does not matter what size the system is. Another step in machine evolution was taken when the capability of storing and of producing energy on demand was developed. As an example, spring loaded machines made use of elastically accumulated mechanical energy; steam engines employed the energy trapped into the wood's chemical bonds, made readily available by combustion. This improvement reduced the role of the available natural energy, since it allowed machines to work even when this was not readily available due to geographic, climatic, and/or meteorological conditions. In this respect, the discovery of electrical energy and the means of its generation and use constitutes probably one of the greatest achievements of mankind and it is certainly one that bears the largest consequences. There is nearly no human activity related to making or processing goods that does not employ electrical energy. Electrical energy has become the primary source of energy in many applications thanks to ease of trasportation and the great performances of electric motors and actuators.

In contemporary times global markets and the competition between companies play a central role in the development of new machines. Efficiency, reliability, ease of use, durability, and cost are the keywords around which innovation spins. Indeed all machines are subject to market's laws (in this sense machines are a product not a tool), thus only machines that are economically sustainable survive.

Recent technological trends see an increasing concern in energy efficiency and miniaturization: the former is related to global worries regarding the falling short of planet Earth raw materials, especially in terms of fossil fuels; the latter is the result of the great advances made in the fields of micro- and nano- technologies. These technologies made possible reducing the size and efficiency of many devices, first and foremost electronic circuits that became integral parts of many devices such as sensors and actuators. The two trends are somehow related in the sense that smaller and lighter systems tend to require less energy in carrying out their functions.

Reducing the context of this introduction to the field of actuators and in particular to that of actuators that convert electrical energy into mechanical energy, a new class of materials and actuators made their appearance in recent times: the so called smart materials and actuators. Some materials present "unusual" couplings between their physical properties (and consequently external fields); because of their peculiarity they were named smart. "Usual" couplings include elasticity (relation between external forces and body deformation), thermal expansion (deformation due to temperature variation), permeability (variations in magnetization related to external magnetic fields), dielectricity (charge accumulation due to external electric field), and many more. "Unusual" couplings are for example deformations induced by a magnetic field (magnetostriction), or by incident light (photostriction); other well-known couplings are those that occurs in shape memory alloys (thermally or magnetically activated phase transition causing deformation), in piezoelectric materials (electric field induced deformations), and in pyroelectric materials (electric field induced heating). For many

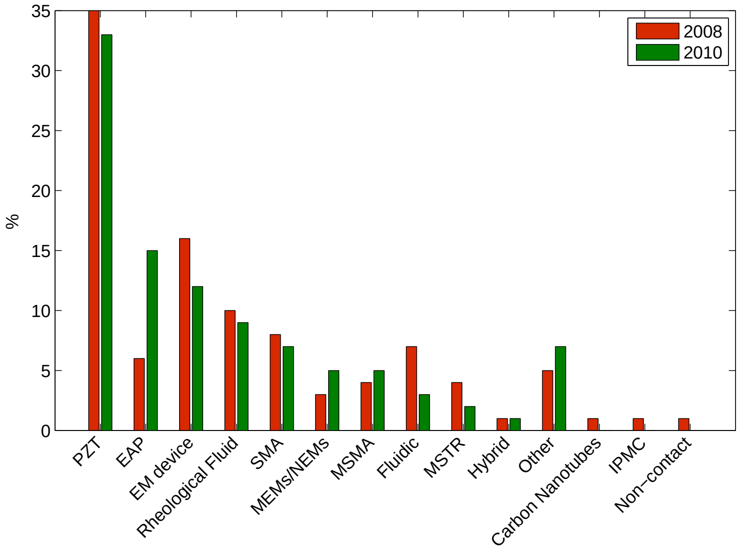

Figure 1: Articles regarding smart materials - 2008/2010 comparison

this process is reversible and allows exploiting the material's peculiar characteristics for designing both sensors and actuators. Among the smart materials, the piezoelectric ones are widely employed in industrial applications of many sorts. Piezoelectric actuators are widely used components that can be found in several everyday objects, from mobile phones to inkjet printers, as well as in more sophisticated devices such as medical equipments and car injection systems [30].

The bi-annual conference "ACTUATOR" is a good place to capture the trends in microactuation and smart material applications; last edition was held in 2010. Figure 1 shows the number of articles presented at the last two conferences divided by technology; it is really interesting to notice that piezoelectric materials are by far the most written about materials, with approximately 35 % of the articles. Furthermore the piezoelectric actuators gather, in the field of small actuators, more interest than EM (electromagnetic) devices such as electric motors. The reason behind this interest is that the efficiency of piezoelectric devices is quite independent on size while that of electric motors decreases sensibly as the motor diameter gets smaller [31]. Of all the piezoelectric devices motors, multilayer actuators, and bulk portion of the material are the most studied (see Fig. 2). In the last conference some motor solutions incorporating piezoelectric multilayer actuators were proposed as well. A comparison between the last two editions see a quite stable trend, as shown in Fig. 1: the interest towards

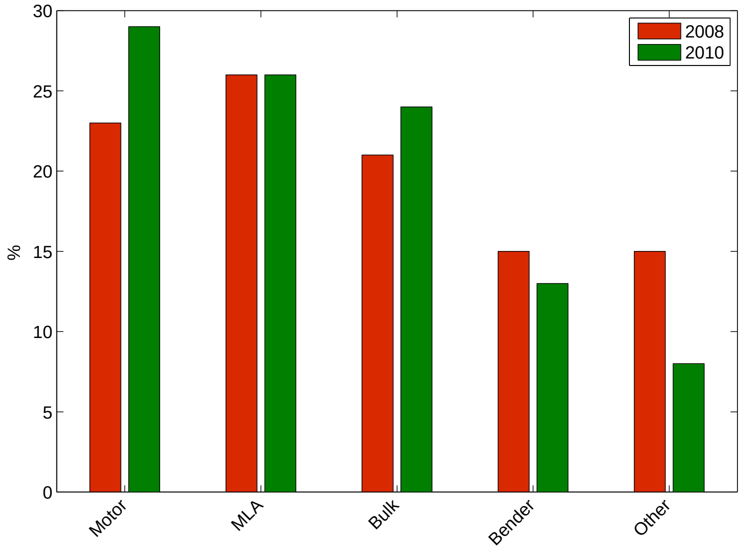

Figure 2: Smart materials employed in actuation - 2008/2010 comparison

piezoelectric devices is constant and motors are coming out as they are more and more suitable for industrial applications, outperforming the electromagnetic counterparts.

A particular type of piezoelectric actuator consists of alternating layers of piezoelectric material and conducting electrodes (see Fig. 3). All the layers are stuck together by glueing or are made in one piece during the manufacturing process (co-firing techniques). The electrodes are connected in parallel to a voltage source: when an electric tension is applied the induced deformation of each layer contributes to the overall displacement of the actuator. Such device, usually referred to as multilayer actuator or MLA, presents the remarkable advantage of producing relatively large displacements with a considerably low driving voltage. The amplitude of such displacement is nevertheless very small for many applications (it rarely exceeds 0.3 mm), thus forcing engineers to design motion amplifiers. The latter is often a viable solution given the high force produced by MLAs.

As it frequently happens when high performances are requested, understanding of the dynamic behaviour is of paramount importance. Only with a complete comprehension of the role each component plays when interacting with the rest of the system, performances can be optimized exploiting each component's capabilities. It is customary to estimate the response speed of a piezoelectric actuator on the basis of its first resonance frequency. When a mechanical system driven by a piezoelectric MLA is analysed the resonance frequency of the whole system must be considered. This

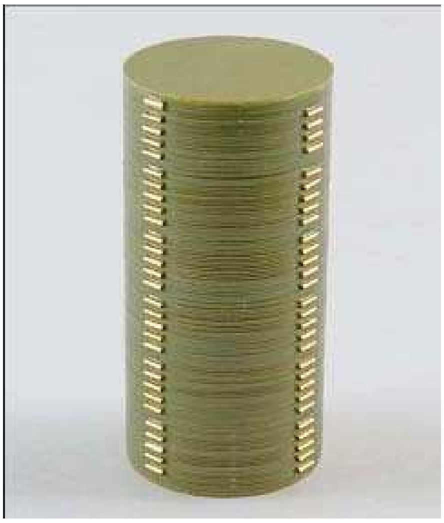

Figure 3: Example of piezoelectric multilayer actuator. Courtesy of [23].

calculation might prove to be a difficult task. Should the driven system be non-linear, appropriate approximations must be carried out. Nevertheless, the dynamic behaviour of the whole system is due not only to its piezo-mechanical characteristics but also to those of the electric driving circuit [31]. From the electrical point of view, piezoelectric actuators can be seen as capacitors, therefore the power source has to supply enough current to charge their capacitance, and that turns into inducing deformation in the piezoelectric actuator. Beside current requirements, the speed of charging a piezo actuator's capacitance depends on the equivalent RC circuit's time constant. A further difficulty is constituted by the fact that the capacitance of a piezoelectric actuator is not constant, on the contrary it varies with its deformation. It is therefore clear how the performances of a system driven by a piezoelectric multilayer actuator are deeply dependent on all the components and their mutual interaction. For such a system a mechatronic approach must be employed in the design process to obtain high dynamic performances.

Mathematical modelling of multilayer piezoelectric devices dates back to at least half a century ago: intensive research on transducer applications along with the limited processing power of computers made researchers concentrate their efforts in predicting the behaviour of such devices through mathematical modelling. The analytical basis for the modelling of piezoelectric continua were set by the former *Institute of Radio Engineers* who issued standards later published by the *Institute of Electrical and Electronics Engineers* as IEEE Std 176-1959 and IEEE Std 178-1958 [13]. In the year 1978 the IEEE Std 176-1978 Standard on Piezoelectricity was published, then revised in 1987 [1]. Both standards report an analytical approach to model the behaviour of piezoelectric materials whichever purpose they are intended for. The standards contain also methods for parameters identifications and measurements.

The first thorough work encountered in literature on mathematical modelling of piezoelectric multilayer devices is that by Brunot [4], a very detailed article on the modelling of "piezoelectric multilayered structures" dating back to 1976, based on previous research on multilayer transducers. Brunot's work aims at formulating a general mathematical model for piezoelectric multilayer structures that could be used either for analysing resonators or transducers. The model presents several layers that may show piezoelectric effect. Each layer material is thus characterised by its own thickness, mass density, viscosity, piezoelectric properties, and conductivity. The resulting equations are very complex and furthermore they are not very well suited for analysing actuators since external mechanical loads cannot be taken into account.

The equations presented in [1], strictly speaking valid only for a piezoelectric continuum, were later adopted for the analysis of multilayer actuators. Intensive research has been carried out at the *Center for Intelligent Material Systems and Structures* of the *Virginia Polytechnic and State University*. In 1994 Liang et al. showed a method for the dynamic analysis of a piezoelectric actuator driving a spring-mass-damper system [14]. The model developed consider the piezoelectric multilayer actuator as constituted by a bulk piezoelectric active part. Therein emphasis was put on impedance matching. The adoption of complex elastic and dielectric material constants allows calculating losses in the actuator [15, 10]. Although treated as a monolithic element, the layered structured of the actuator was taken into account for the electric circuit calculation in [8].

The aforementioned works never ventured the field of non-linear behaviour, a necessary step to take into account hysteresis and to analyse large deformations. The motivation of research in this field can be easily ascribed to the need for micropositioners and relative control algorithms, as well as accurate computation of energy dissipation in ultrasonic motors. Works in this area tackled the subjects of modeling non-linearities (i.e. [11, 25, 28]). Another issue related to non-linearities is the influence of the actual internal electrodes configuration on overall behaviour. Some analytical approaches were proposed [32] although very often numerical simulation and finite element modelling were preferred (as in [12, 3]).

Notwithstanding the remarkable efforts put in for an accurate modelling of the MLA, often researchers who need to integrate an MLA into a mechanical system do use very simple models [20, 5, 16]. The more accurate available analytical models are either extremely complex to implement or do not allow introducing external loads. Non-analytical models lack synthesis capabilities, thus proving not to be a valid early design tool.

The models presented in this dissertation achieve the remarkable objective of providing more information on the dynamics of mechanical systems driven by piezoelectric MLAs without increasing the complexity of the mathematical model. Such accomplishment is made considering the actual distribution of the piezoelectric layers. The additional information obtained includes a more complete description of the dynamic behaviour at higher-than-first-resonance frequencies. Piezoelectric multilayer actuators are very fast devices that find wide use in high precision and/or high dynamics mechanical systems, such as injection systems, inkjet printers, resonators, vibration control systems, energy harvesting devices, etc. Ongoing studies on active vibration control employ piezoelectric MLAs for actuating purposes, given their high load capabilities and resonant frequency (see [24]). Furthermore, piezoelectric MLAs are used as components in ultrasonic motors, thus they are driven near either resonance ot anti-resonance frequencies [2]. In such cases the knowledge of the frequency response function is of paramount importance.

Nomenclature

Table 1 shows the main symbols and units used in the following paper, all in compliance with IEEE Std 176-1987.

Symbol	**Description**	**SI Unit**
c_{ijkl}, c_{pq}	Elastic stiffness constant	N/m^2
C	Capacitance	F
d_{ijk}, d_{ip}	Piezoelectric (strain) constant	m/V, C/N
D_i	Electric displacement	C/m^2
e_{ijk}, e_{ip}	Piezoelectric (stress) constant	C/m^2
E_i	Electric field	V/m
f	Frequency	Hz
g_{ijk}, g_{ip}	Piezoelectric (voltage) constant	$V \cdot m/N$, m^2/C
I	Electric current	A
j	Imaginary unit	-
Q	Electric charge	C
R	Resistance	Ω
s_{ijkl}, s_{pq}	Elastic compliance constant	m^2/N
S_{ij}, S_p	Strain	-
t	Thickness	m
T_{ij}, T_p	Stress	N/m^2
V_p	Electric tension	V
v	Sound speed	m/s
ε_{ij}	Permettivity	F/m
ϕ	Scalar electric potential	V
τ	Time	s
ω	Angular frequency	Hz
The field symbols D, E, S, and T can be used as superscripts of constants meaning that the quantity has been measured at constant values of the specified field		

Table 1: Piezoelectricity symbols and units

Chapter 1

Piezoelectric thin plates

A thin plate of piezoelectric material is generally used either in the so-called d_{33} mode or d_{13} mode. The former exploits the material's property of undergoing deformation in the same direction along which the electric field is applied (this direction is the poling direction as well); the latter mode makes use of the in-plane deformation due to an electric field whose lines are perpendicular to the plate surface.

The plate considered is so thin that three dimensional effects can be neglected. Its dimensions are t (thickness), and A (area). A coordinate system is placed at its very center (see Fig. 1.1) and the direction 3 is normal to the plate surface (in the figure the coordinate x is along this direction). At the upper and lower surfaces are placed two electrodes that induce an electric field along the axis 3 when connected to a voltage source.

Pertinent constitutive and dynamic equations as derived from Eq. B.18 and Eq. B.19 are

$$\begin{cases} T = c^E S - eE \\ D = eS + \varepsilon^S E \end{cases} \tag{1.1}$$

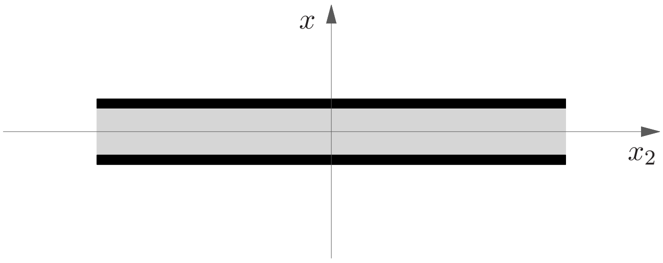

Figure 1.1: Unconstrained plate model

$$\begin{cases} c^E u_{,xx} + e\varphi_{,xx} = \rho u_{,\tau\tau} \\ e u_{,xx} - \varepsilon^S \varphi_{,xx} = 0 \end{cases} \tag{1.2}$$

based on the hypothesis that strains S_1, S_2, S_4, S_5 and S_6 are negligible, as well as the electric fields along directions 1 and 2. The subscript 3 has been dropped for clarity's sake and substituted by an x in case of differentiation with respect to the coordinate x_3 [1].

1.1 Single plate dynamics

The dynamics of a thin plate can be efficiently studied employing Eq. 1.1 and 1.2. Given the same assumptions on displacements and fields, the dynamic equations can be simplified in

$$\begin{cases} \left(c^E + \frac{e^2}{\varepsilon^S}\right) u_{,xx} = \rho u_{,\tau\tau} \\ u_{,xx} = \frac{\varepsilon^S}{e}\varphi_{,xx} \end{cases} \tag{1.3}$$

The first of the two equations models the dynamics of the mechanical part of the thin plate while the second connects the mechanical domain to the electric field domain. The first equation is formally equal to the wave equations, therefore it will be re-written as

$$u_{,xx} = \frac{1}{v^2} u_{,\tau\tau} \tag{1.4}$$

where $v = \sqrt{\frac{c^E + \frac{e^2}{\varepsilon^S}}{\rho}}$ is the speed of sound in the piezoelectric medium. The periodic solution to the wave equation is very well known and it assumes the generic expression of

$$u(x,\tau) = \left(A_1 \cos\left(\frac{\omega}{v}x\right) + A_2 \sin\left(\frac{\omega}{v}x\right)\right)\sin(\omega\tau) \tag{1.5}$$

The second equation of Eq. 1.3 can be integrated in time yielding

$$\varphi(x,\tau) = \frac{e}{\varepsilon^S} u(x,\tau) + B_1(\tau)x + B_2(\tau) \tag{1.6}$$

Since electric potential is only defined up to an additive constant, $B_2(\tau)$ can be set arbitrarily to zero.

---

[1] The partial derivative of the function X with respect to a variable Y are expressed in this paper as $X_{,Y}$. A repetition of the variable indicates higher order derivative.

The integration constants A_1, A_2, and B_1 can be found imposing boundary conditions to the mechanical and electrical variables. From the constitutive equations Eq. 1.1 the explicit expression of the mechanical stress and the electric displacement can be found:

$$\begin{cases} T(x,\tau) = c^E u_{,x} + e\varphi_{,x} \\ D(x,\tau) = eu_{,x} - \varepsilon^S \varphi_{,x} \end{cases} \tag{1.7}$$

Substituting Eq. 1.5 into Eq. 1.7 yields

$$\begin{cases} T = \frac{\omega}{v}\left(c^E + \frac{e^2}{\varepsilon^S}\right)\left(-A_1 \sin\left(\frac{\omega}{v}x\right) + A_2 \cos\left(\frac{\omega}{v}x\right)\right) + eB_1 \\ D = -\varepsilon^S B_1 \end{cases} \tag{1.8}$$

where the time dependent part of Eq. 1.5 has been left out for clarity's sake, given that

$$\begin{cases} T(x,\tau) = T\sin(\omega\tau) \\ D(x,\tau) = D\sin(\omega\tau) \\ B_1(\tau) = B_1 \sin(\omega\tau) \end{cases} \tag{1.9}$$

The electric displacement D allows a simple calculation of the charge Q accumulated on the electrodes by integration over the plate surface of area A

$$Q(\tau) = -\int_A D(x,\tau)\ \mathrm{d}A = \int_A \varepsilon^S B_1(\tau)\ \mathrm{d}A_A = \varepsilon^S A B_1 \sin(\omega\tau) \tag{1.10}$$

It is easy then to calculate the electric current I flowing out of the electrode by differentiating the explicit expression of Q once the integration constant $B_1(\tau)$ is found

$$I(\tau) = \varepsilon^S A\omega B_1 \cos(\omega\tau) \tag{1.11}$$

It is worth noticing that in this formulation the displacement is always in phase with the electric tension applied to the electrodes while the current is always 90° shifted. In this respect the piezoelectric actuator behaves electrically as a capacitor whose capacitance is frequency dependent. The value of the capacitance can be calculated easily as

$$C_{\mathrm{PZT}} = \varepsilon^S A \frac{B_1}{V_p} \tag{1.12}$$

1.1.1 Unconstrained plate

An unconstrained plate is free to vibrate in space and it may be subject to an electric field given by a voltage V_p applied to the electrodes. Boundary conditions express the potential difference among the upper and lower surface of the piezoelectric plate and the zero stress condition at the aforementioned surfaces. It must be noticed that this statement is true if and only if the electrodes mass is negligible. Boundary equations are

$$\begin{cases} \varphi\left(\frac{t}{2},\tau\right)-\varphi\left(-\frac{t}{2},\tau\right)=V_p\sin\left(\omega\tau\right) \\ T\left(\frac{t}{2},\tau\right)=0 \\ T\left(-\frac{t}{2},\tau\right)=0 \end{cases} \tag{1.13}$$

Substituting Eq. 1.6 and 1.8 into Eq. 1.13 yields the integration constants A_1, A_2, and B_1

$$\begin{cases} 2\frac{e}{\varepsilon^S}A_2\sin\left(\frac{\omega}{v}\frac{t}{2}\right)+tB_1=V_p \\ \frac{\omega}{v}\bar{c}^E A_2\cos\left(\frac{\omega}{v}\frac{t}{2}\right)+eB_1=0 \\ \frac{\omega}{v}\bar{c}^E A_1\sin\left(\frac{\omega}{v}\frac{t}{2}\right)=0 \end{cases} \tag{1.14}$$

having defined $\bar{c}^E=c^E+\frac{e^2}{\varepsilon^S}$. The system of equations can be solved as

$$\begin{cases} A_2=\frac{V_p}{2\frac{e}{\varepsilon^S}\left(\sin\left(\frac{\omega}{v}\frac{t}{2}\right)-\frac{\varepsilon^S\bar{c}^E}{e^2}\left(\frac{\omega}{v}\frac{t}{2}\right)\cos\left(\frac{\omega}{v}\frac{t}{2}\right)\right)} \\ B_1=\frac{V_p}{t\left(1-\frac{e^2}{\varepsilon^S\bar{c}^E}\frac{\tan\left(\frac{\omega}{v}\frac{t}{2}\right)}{\frac{\omega}{v}\frac{t}{2}}\right)} \\ \frac{\omega}{v}\bar{c}^E A_1\sin\left(\frac{\omega}{v}\frac{t}{2}\right)=0 \end{cases} \tag{1.15}$$

The last equation of the set presents non-trivial solution if and only if $A_1=0$, otherwise the driving angular frequency ω must satisfy the following relation

$$\omega^{(n)}=2n\pi\frac{v}{t} \qquad n=0,1,2,\ldots$$

Resonance

The amplitude of the displacement u depends on the driving voltage, on the material constants, on the plate dimensions, and on the driving frequency. In particular, for a given piezoelectric plate, there are values of driving frequency for which the denominators of Eq. 1.15 tend to infinity or zero. In correspondence of such values, resonance or anti-resonance conditions are found.

In resonance conditions the electric source introduces energy in the system continuously and this energy is converted both in mechanical energy, that is both kinetic and deformation energy. The resonance condition implies therefore an increase in deformation and displacement; such condition is reached when the denominator of the first equation of the set Eq. 1.15 is zero. Introducing the variable $\xi = \frac{\omega}{v}\frac{t}{2}$, the resonance condition is met when

$$\sin\left(\xi\right) - \frac{\varepsilon^S \bar{c}^E}{e^2}\xi\cos\left(\xi\right) = 0 \tag{1.16}$$

This equation is implicit and thus requires numerical method to be solved. Furthermore, it can be easily shown that the denominator of the second equation of the set Eq. 1.15 is zero in the same conditions. In a physical perspective, that means the current tends to infinity in resonance conditions.

On the contrary, anti-resonance conditions are reached when there is no energy transmission from the source to the system. In this situation there is no displacement nor deformation and the current is not flowing at all. From a mathematical point of view, anti-resonance condition is reached when the denominators of Eq. 1.15 tends to infinity, that is

$$\tan\left(\xi\right) \rightarrow \pm\infty \qquad \omega^{(n)} = 2\left(\frac{\pi}{2} + n\pi\right)\frac{v}{t} \qquad n = 1, 2, \ldots \tag{1.17}$$

1.1.2 Inertially loaded unconstrained plate

In the previous investigation the influence of the electrode mass was dismissed, on the ground that it can be regarded as negligible. In this section the influence of a symmetric inertial load is taken into account, and it will be shown that, for reasonably thin electrodes, their mass does not influence consistently the values of the resonance frequencies.

The symmetric inertial load is constituted by two rigid bodies of mass m_l fixed to the electrodes' outer surfaces (green body in Fig. 1.2). The boundary conditions will be written as

$$\begin{cases} \varphi\left(\frac{t}{2},\tau\right) - \varphi\left(-\frac{t}{2},\tau\right) = V_p\sin\left(\omega\tau\right) \\ T\left(\frac{t}{2},\tau\right) = -\frac{m_l+m_e}{A}u_{,\tau\tau}\left(\frac{t}{2},\tau\right) \\ T\left(-\frac{t}{2},\tau\right) = \frac{m_l+m_e}{A}u_{,\tau\tau}\left(-\frac{t}{2},\tau\right) \end{cases} \tag{1.18}$$

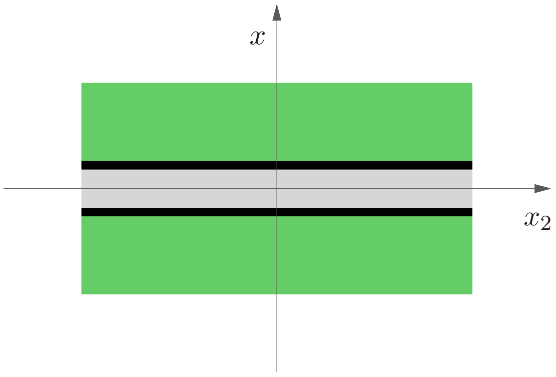

Figure 1.2: Unconstrained plate with inertial load model

where m_e is the electrode mass. Substituting Eq. 1.6 and 1.8 into Eq. 1.18 allows finding the integration constants A_1, A_2, and B_1. The system of equations is

$$\begin{cases} 2\frac{e}{\varepsilon^S} A_2 \sin\left(\frac{\omega}{v}\frac{t}{2}\right) + tB_1 = V_p \\ A_2 \frac{\omega}{v} \bar{c}^E \cos\left(\frac{\omega}{v}\frac{t}{2}\right) + eB_1 = A_2 \frac{m_l+m_e}{A} \omega^2 \sin\left(\frac{\omega}{v}\frac{t}{2}\right) \\ \frac{\omega}{v} \bar{c}^E A_1 \sin\left(\frac{\omega}{v}\frac{t}{2}\right) = -A_1 \omega^2 \frac{m_l+m_e}{A} \cos\left(\frac{\omega}{v}\frac{t}{2}\right) \end{cases} \tag{1.19}$$

which can be solved as

$$\begin{cases} B_1 = \frac{\left(\frac{2\bar{c}^E \varepsilon^S}{\rho t e^2} \frac{m_l+m_e}{A} \left(\frac{\omega}{v}\frac{t}{2}\right) \sin\left(\frac{\omega}{v}\frac{t}{2}\right) - \frac{\varepsilon^S \bar{c}^E}{e^2} \cos\left(\frac{\omega}{v}\frac{t}{2}\right)\right)\left(\frac{\omega}{v}\frac{t}{2}\right)}{\left(\frac{2\bar{c}^E \varepsilon^S}{\rho t e^2} \frac{m_l+m_e}{A} \left(\frac{\omega}{v}\frac{t}{2}\right)^2 + 1\right) \sin\left(\frac{\omega}{v}\frac{t}{2}\right) - \frac{\varepsilon^S \bar{c}^E}{e^2} \left(\frac{\omega}{v}\frac{t}{2}\right) \cos\left(\frac{\omega}{v}\frac{t}{2}\right)} \frac{V_p}{t} \\ A_2 = \frac{V_p}{2\frac{e}{\varepsilon^S}\left(\left(\frac{2\bar{c}^E \varepsilon^S}{\rho t e^2} \frac{m_l+m_e}{A} \left(\frac{\omega}{v}\frac{t}{2}\right)^2 + 1\right) \sin\left(\frac{\omega}{v}\frac{t}{2}\right) - \frac{\varepsilon^S \bar{c}^E}{e^2} \left(\frac{\omega}{v}\frac{t}{2}\right) \cos\left(\frac{\omega}{v}\frac{t}{2}\right)\right)} \\ A_1 \left(\frac{\omega}{v} \bar{c}^E \sin\left(\frac{\omega}{v}\frac{t}{2}\right) + \omega^2 \frac{m_l+m_e}{A} \cos\left(\frac{\omega}{v}\frac{t}{2}\right)\right) = 0 \end{cases} \tag{1.20}$$

As previously found, the integration constant A_1 should be set to zero in order not to introduce additional constraints to the angular frequency ω that would leave the value itself of A_1 discretionary.

Resonance

The resonance and anti-resonance conditions can be found respectively when the coefficients A_2 and B_1 go to infinity or zero. From the formulation found in Eq. 1.20, the resonance condition implies

$$\left(\frac{2\bar{c}^E \varepsilon^S}{\rho t e^2} \frac{m_l+m_e}{A} \xi^2 + 1\right) \sin(\xi) - \frac{\varepsilon^S \bar{c}^E}{e^2} \xi \cos(\xi) = 0 \tag{1.21}$$

where the variable ξ has been employed replacing $\frac{\omega}{v}\frac{t}{2}$. The anti-resonance condition can be found when the numerator of the expression of B_1 is null, that is

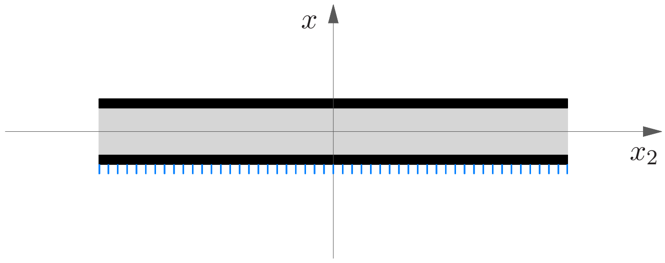

Figure 1.3: Constrained plate

$$\frac{2}{\rho t}\frac{m_l+m_e}{A}\xi\sin\left(\xi\right)-\cos\left(\xi\right)=0 \tag{1.22}$$

Both Eq. 1.21 and 1.22 are implicit and require numerical methods to be solved.

1.1.3 Constrained plate

A more meaningful configuration, in the perspective of actuation, sees one surface of the plate constrained to a fixed reference (see Fig. 1.3). In such a condition, when the piezoelectric plate is excited by a driving voltage, the free surface moves and can interact with a load. This configuration is that of an actuator. The boundary conditions can be formulated as

$$\begin{cases} \varphi\left(\frac{t}{2},\tau\right)-\varphi\left(-\frac{t}{2},\tau\right)=V_p\sin\left(\omega\tau\right) \\ T\left(\frac{t}{2},\tau\right)=0 \\ u\left(-\frac{t}{2},\tau\right)=0 \end{cases} \tag{1.23}$$

and more explicitly as

$$\begin{cases} 2\frac{e}{\varepsilon^S}A_2\sin\left(\frac{\omega}{v}\frac{t}{2}\right)+tB_1=V_p \\ -\frac{\omega}{v}\bar{c}^EA_1\sin\left(\frac{\omega}{v}\frac{t}{2}\right)+\frac{\omega}{v}\bar{c}^EA_2\cos\left(\frac{\omega}{v}\frac{t}{2}\right)+eB_1=0 \\ A_1\cos\left(-\frac{\omega}{v}\frac{t}{2}\right)+A_2\sin\left(-\frac{\omega}{v}\frac{t}{2}\right)=0 \end{cases} \tag{1.24}$$

The solution to the system is

$$\begin{cases} B_1=\frac{1}{1-\frac{e^2}{\varepsilon^S\bar{c}^E}\frac{\tan\left(2\frac{\omega}{v}\frac{t}{2}\right)}{\left(2\frac{\omega}{v}\frac{t}{2}\right)}}\frac{V_p}{t} \\ A_2=\frac{-\frac{\varepsilon^S}{e}\cos\left(\frac{\omega}{v}\frac{t}{2}\right)}{\frac{\bar{c}^E\varepsilon^S}{e^2}\left(2\frac{\omega}{v}\frac{t}{2}\right)\cos\left(2\frac{\omega}{v}\frac{t}{2}\right)-\sin\left(2\frac{\omega}{v}\frac{t}{2}\right)}V_p \\ A_1=\frac{-\frac{\varepsilon^S}{e}\sin\left(\frac{\omega}{v}\frac{t}{2}\right)}{\frac{\bar{c}^E\varepsilon^S}{e^2}\left(2\frac{\omega}{v}\frac{t}{2}\right)\cos\left(2\frac{\omega}{v}\frac{t}{2}\right)-\sin\left(2\frac{\omega}{v}\frac{t}{2}\right)}V_p \end{cases} \tag{1.25}$$

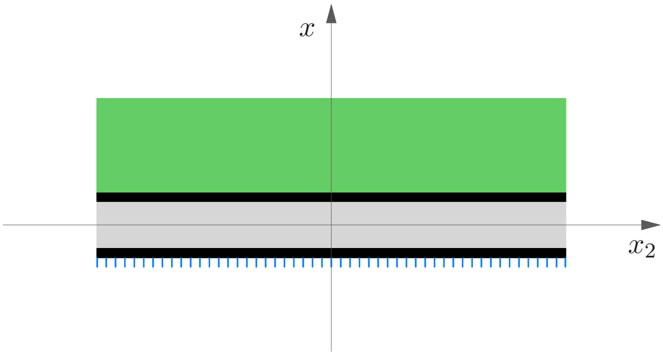

Figure 1.4: Constrained plate with additional mass

In this case it is interesting to calculate the maximum displacement $u_{\max}$, that obviously occurs at $x = \frac{t}{2}$. Substituting the values found for A_1 and A_2 in Eq. yields

$$u_{\max} = \frac{\frac{\varepsilon^S}{e}}{1 - \frac{\bar{c}^E \varepsilon^S}{e^2}\left(2\frac{\omega}{v}\frac{t}{2}\right)\cot\left(2\frac{\omega}{v}\frac{t}{2}\right)} V_p \tag{1.26}$$

Resonance

Resonance conditions can be found by analysing the maximum displacement formula (Eq. 1.26). Resonance is found when

$$\frac{\varepsilon^S \bar{c}^E}{e^2}(2\xi)\cot(2\xi) = 1 \tag{1.27}$$

is satisfied. On the contrary anti-resonance frequencies satisfy the relation

$$\cot(2\xi) \to \pm\infty$$

that is

$$\omega^{(n)} = n\pi\frac{v}{t} \qquad n = 1, 2, \ldots \tag{1.28}$$

1.1.4 Inertially loaded constrained plate

The influence of an inertial load on the system (see Fig. 1.4) can be analysed considering the following boundary conditions

$$\begin{cases} \varphi\left(\frac{t}{2}, \tau\right) - \varphi\left(-\frac{t}{2}, \tau\right) = V_p \sin(\omega\tau) \\ T\left(\frac{t}{2}, \tau\right) = -\frac{m_l + m_e}{A} u_{,\tau\tau}\left(\frac{t}{2}, \tau\right) \\ u\left(-\frac{t}{2}, \tau\right) = 0 \end{cases} \tag{1.29}$$

which can be written, thanks to Eq. 1.23 and 1.19

$$\begin{cases} 2\frac{e}{\varepsilon^S} A_2 \sin\left(\frac{\omega}{v}\frac{t}{2}\right) + tB_1 = V_p \\ -\frac{\omega}{v}\bar{c}^E A_1 \sin\left(\frac{\omega}{v}\frac{t}{2}\right) + \frac{\omega}{v}\bar{c}^E A_2 \cos\left(\frac{\omega}{v}\frac{t}{2}\right) + eB_1 = \frac{m_l+m_e}{A}\omega^2 \left(A_1 \cos\left(\frac{\omega}{v}\frac{t}{2}\right) + A_2 \sin\left(\frac{\omega}{v}\frac{t}{2}\right)\right) \\ A_1 \cos\left(-\frac{\omega}{v}\frac{t}{2}\right) + A_2 \sin\left(-\frac{\omega}{v}\frac{t}{2}\right) = 0 \end{cases} \tag{1.30}$$

The solution to such boundary conditions is

$$\begin{cases} B_1 = \dfrac{\frac{\varepsilon^S \bar{c}^E}{e^2} - \frac{m_l+m_e}{A}\frac{\varepsilon^S v^2}{te^2}\left(2\frac{\omega}{v}\frac{t}{2}\right)\tan\left(2\frac{\omega}{v}\frac{t}{2}\right)}{\frac{\varepsilon^S \bar{c}^E}{e^2} - \left(1+\frac{m_l+m_e}{A}\frac{\varepsilon^S v^2}{te^2}\left(2\frac{\omega}{v}\frac{t}{2}\right)^2\right)\frac{\tan\left(2\frac{\omega}{v}\frac{t}{2}\right)}{\left(2\frac{\omega}{v}\frac{t}{2}\right)}}\dfrac{V_p}{t} \\ A_2 = \dfrac{-\frac{\varepsilon^S}{e}V_p\cos\left(\frac{\omega}{v}\frac{t}{2}\right)}{\frac{\varepsilon^S \bar{c}^E}{e^2}\left(2\frac{\omega}{v}\frac{t}{2}\right)\cos\left(2\frac{\omega}{v}\frac{t}{2}\right) - \left(1+\frac{m_l+m_e}{A}\frac{\varepsilon^S v^2}{te^2}\left(2\frac{\omega}{v}\frac{t}{2}\right)^2\right)\sin\left(2\frac{\omega}{v}\frac{t}{2}\right)} \\ A_1 = \dfrac{-\frac{\varepsilon^S}{e}V_p\sin\left(\frac{\omega}{v}\frac{t}{2}\right)}{\frac{\varepsilon^S \bar{c}^E}{e^2}\left(2\frac{\omega}{v}\frac{t}{2}\right)\cos\left(2\frac{\omega}{v}\frac{t}{2}\right) - \left(1+\frac{m_l+m_e}{A}\frac{\varepsilon^S v^2}{te^2}\left(2\frac{\omega}{v}\frac{t}{2}\right)^2\right)\sin\left(2\frac{\omega}{v}\frac{t}{2}\right)} \end{cases} \tag{1.31}$$

The maximum displacement occurs at the upper surface and it is

$$u_{\max} = \frac{\frac{\varepsilon^S}{e}}{1 + \frac{m_l+m_e}{A}\frac{\varepsilon^S v^2}{te^2}\left(2\frac{\omega}{v}\frac{t}{2}\right)^2 - \frac{\varepsilon^S \bar{c}^E}{e^2}\left(2\frac{\omega}{v}\frac{t}{2}\right)\cot\left(2\frac{\omega}{v}\frac{t}{2}\right)} V_p \tag{1.32}$$

Resonance

Resonance conditions can be found by analysing the maximum displacement formula (Eq. 1.32). Resonance is found when

$$1 + \frac{m_l + m_e}{A}\frac{\varepsilon^S v^2}{te^2}(2\xi)^2 - \frac{\varepsilon^S \bar{c}^E}{e^2}(2\xi)\cot(2\xi) = 0 \tag{1.33}$$

is satisfied. On the contrary anti-resonance frequencies satisfy the relation

$$\cot(2\xi) \to \pm\infty$$

that is

$$\omega^{(n)} = n\pi\frac{v}{t} \qquad n = 1, 2, \ldots \tag{1.34}$$

1.2 Driving circuit

The model presented in the previous sections does not include losses of whatever nature, mechanical, dielectrical, or piezoelectrical. A way to include losses that naturally occurs in all the aforementioned domains is to introduce a dissipative element in the driving

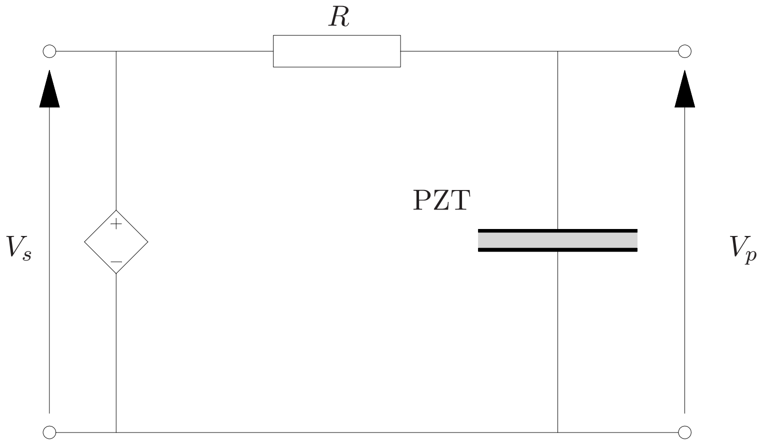

Figure 1.5: Driving circuit of the piezoelectric actuator

electric circuit. The driving circuit is constituted by a controllable voltage source V_s, a resistor R, and the piezoelectric actuator (see Fig. 1.5).

As previously pointed out, the piezoelectric actuator can be analysed in an electric circuit as a capacitor with a frequency-dependent capacitance. With the definition of capacitance of Eq. 1.12, the driving ciruict can be analysed as a standard RC circuit for which the following relations hold

$$\begin{cases} \theta = \arctan\left(RC_{\mathrm{PZT}}\ \omega\right) \\ V_p = V_s \cos\theta \end{cases} \tag{1.35}$$

In order to evaluate the expressions of Eq. 1.35, a configuration must be chosen for the system. Considering the constrained plate with an inertial load the capacitance can be written as

$$C_{\mathrm{PZT}} = \frac{\frac{\varepsilon^S \bar{c}^E}{e^2} - \frac{m_l+m_e}{A}\frac{\varepsilon^S v^2}{te^2}\left(2\frac{\omega}{v}\frac{t}{2}\right)\tan\left(2\frac{\omega}{v}\frac{t}{2}\right)}{\frac{\varepsilon^S \bar{c}^E}{e^2} - \left(1 + \frac{m_l+m_e}{A}\frac{\varepsilon^S v^2}{te^2}\left(2\frac{\omega}{v}\frac{t}{2}\right)^2\right)\frac{\tan\left(2\frac{\omega}{v}\frac{t}{2}\right)}{\left(2\frac{\omega}{v}\frac{t}{2}\right)}}\frac{\varepsilon^S A}{t} \tag{1.36}$$

1.3 Simulations and commentary

The equations shown in the previous sections allow a straightforward calculation of the system's frequency response function (FRF). The frequency response function gives an insight about the dynamic behaviour of the system when excited by a periodic signal.

First of all the material's constants need be known. From most piezoelectric material's datasheets the values of c_{33}^E, e_{33}, and ε_{33}^S are not found, while the values of s^E, d, and ε^T are more common. Thus the relations of Eq. B.4 must be employed. In particular:

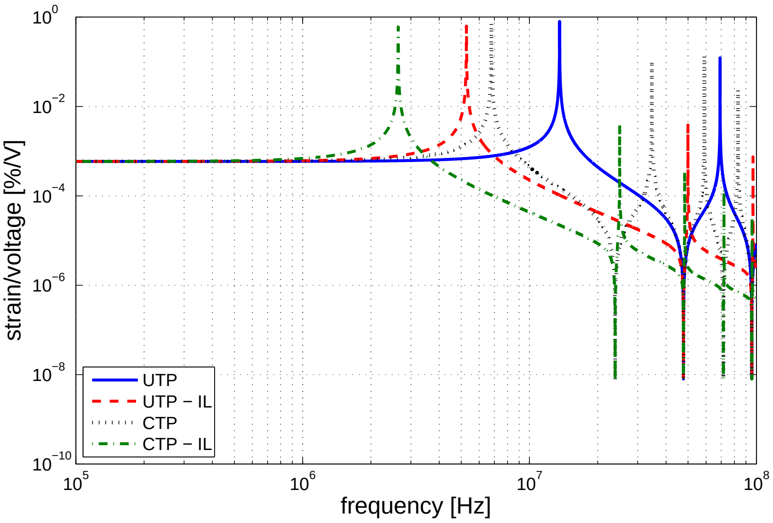

Figure 1.6: Strain FRF for different constraints and loading conditions

$$\begin{cases} c^E_{pr} s^E_{qr} = \delta_{pq} \\ \varepsilon^T_{pq} = \varepsilon^S_{pq} + d_{pr} e_{qr} \\ e_{pq} = d_{pr} c^E_{rq} \end{cases}$$

which can be solved as

$$\begin{cases} \left[c^E\right] = \left[s^E\right]^{-1} \\ [e] = [d] \cdot \left[c^E\right] \\ \left[\varepsilon^S\right] = \left[\varepsilon^T\right] - [e] \cdot [d]^{\mathrm{T}} \end{cases} \tag{1.37}$$

It must be noticed that the inverse of the matrix $\left[s^E\right]$ might not exist due to null rank, condition that often occurs because some coefficients of $\left[s^E\right]$ might not be given by the manufacturer. In this case the matrix $\left[c^E\right]$ shall be calculated with the Moore-Penrose pseudoinverse algorithm ([19], [21]).

This is the case for the material considered for the following simulations. The manufacturer's datasheets reports the values of s^E_{11}, s^E_{33}, ε^T_{11}, ε^T_{33}, d_{31}, d_{15} and d_{33} (see Tab. C.1 in appendix C), besides many more parameters that are not employed in the modelling presented, such as aging stability, temperature stability, current constants, etc. Table 1.37 shows the material's parameter necessary for the present simulation calculated with the above-mentioned procedure.

Figure 1.6 shows the strain FRF with different constraints and loading conditions. The acronim "UTP" stands for *unconstrained thin plate* while "CTP" stands for *con-*

PIC 151		
piezoelectric stress constant	e	29.5 C/N
stiffness constant	c^E	$5 \cdot 10^{10}$ N/m^2
dielectric permettivity constant	ε^S	$6.8192 \cdot 10^{-9}$ F/m
mass density	ρ	$7.8 \cdot 10^3$ kg/m^3

Table 1.1: PI Ceramic - PIC 151 characteristics [22]

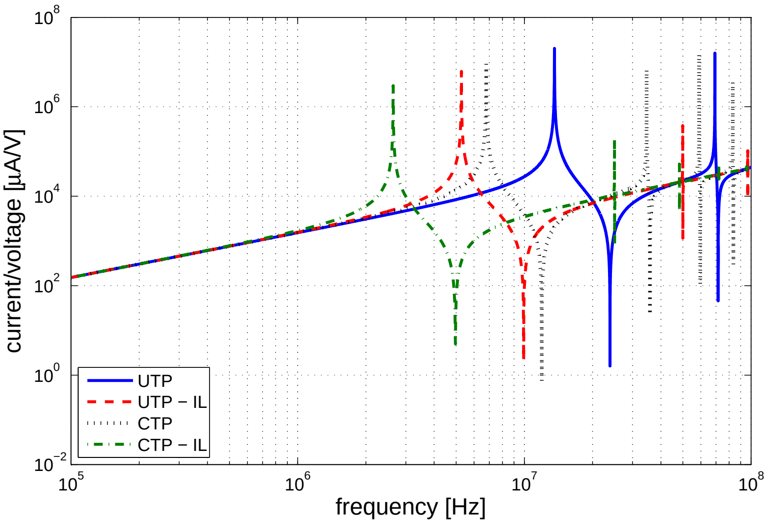

Figure 1.7: Current FRF for different constraints and loading conditions

strained thin plate. The unconstrained thin plate is free to vibrate about its centre of mass; in other word it behaves as if it had a fixed centre of mass. The constrained configuration sees the thin plate constrained on one side to a fixed frate. When labeled with an additional "IL", the thin plate is loaded with and inertial load. In these simulations the load mass has been chosen to be equal to the thin plate mass itself. The normalized load mass coefficient k_m, defined as the ratio between the load mass and the piezoelectric material mass, is introduced in order to better define the inertial loading condition on the piezoelectric device.

The FRF of the strain shows a flat part up to a certain value of frequency, than the strain amplitude increasases, peaking in correspondence of the first the resonance frequency. In the reported range, a second resonance frequency and two anti-resonance frequencies can be seen. As easily predictable, the values of the resonance frequency is lower when an inertial load is considered. The resonance frequencies are 13.58 MHz, 6.78 MHz, 5.28 MHz, and 2.64 MHz respectevly for UTP, UTP-IL, CTP, and CTP-IL. It is really interesting to point out that the anti-resonance frequencies do not depend on

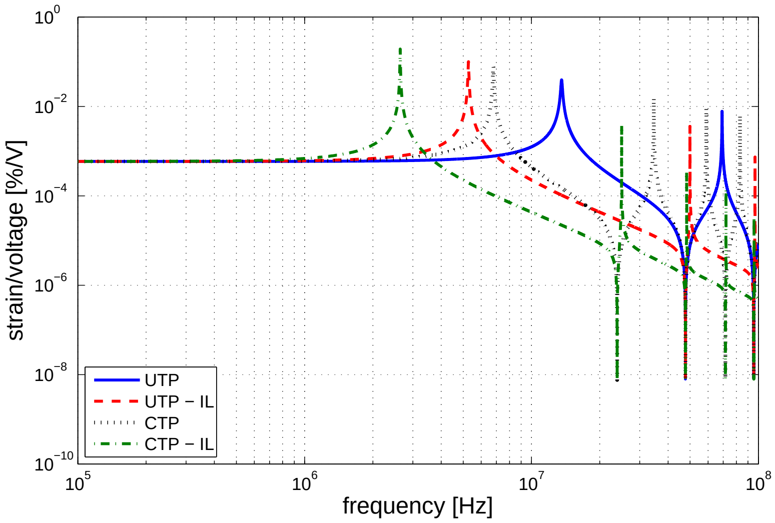

Figure 1.8: Strain FRF when considering an electric resistance

inertial loading: both the simulations for the unloaded and the loaded plate show equal anti-resonance frequencies (47.72 MHz and 23.86 MHz for the unloaded and inertially loaded thin plate).

The current FRF (Fig. 1.7) shows a gain of one order of magnitude per decade in the low frequency region. At high frequencies resonances occurs; it is very interesting to notice that anti-resonances are found in correspondence of lower frequencies than those of Fig. 1.6. Values for the four anti-resonance frequencies are 4.97 MHz, 9.92 MHz, 11.93 MHz, and 23.86 MHz.

When the driving circuit includes a resistor, the strain and current FRF changes as shown in Fig. 1.8 and 1.9. The results for the current at low frequencies is very much in accordance with the analysis of an electric RC circuit of given capacitance: the current FRFs at low frequencies match. The inclusion of the resistor changes to a limited extent the FRF plots. To quantify the difference, the FRF plots have been magnified and superposed (see Fig. 1.10). As expected, the calculated gain does not go to infinity anymore but is limited to 0.2 %/V and 1 A/V for respectively the strain and the current.

A look on the voltage across the piezoelectric plate shows that in this case the current at low frequencies is really negligible. Figure 1.11 shows the FRF of the voltage V_p over the driving voltage V_s. It can be noticed that the downwards peaks of the plot are generally quite narrow. The higher the inertial loading (due to either constraining or to the load mass itself) the narrower the peak is. The lower part of Fig. 1.11 shows

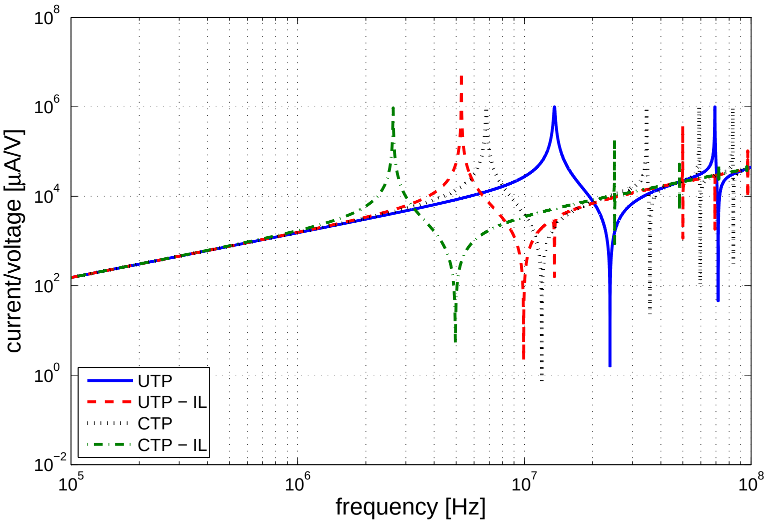

Figure 1.9: Current FRF when considering an electric resistance

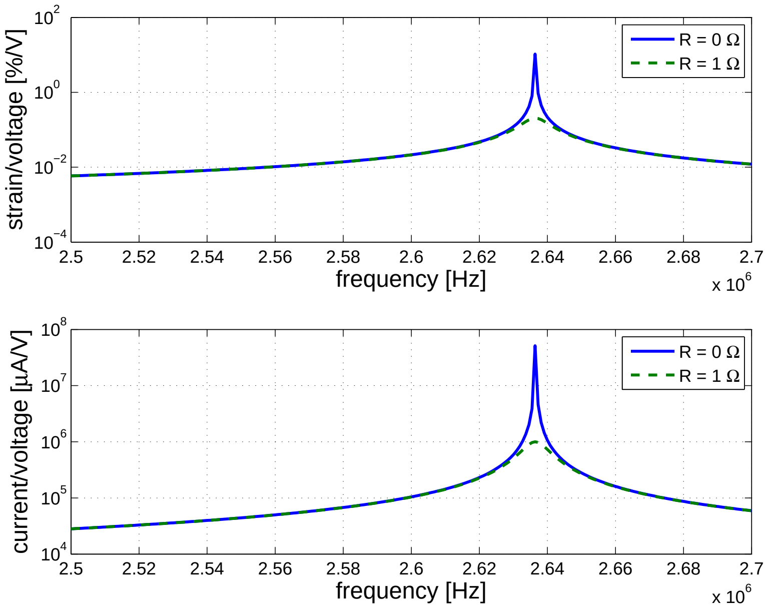

Figure 1.10: Current FRF comparison: with and without resistive load

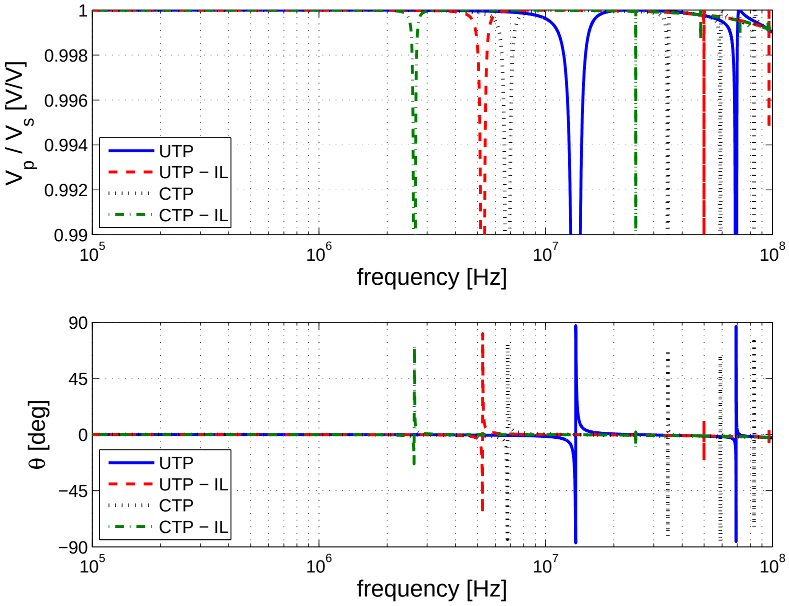

Figure 1.11: Voltage across piezoelectric actuator FRF

the phase plot of V_p/V_s, which is the same for the displacement/strain as well. The current FRF phase plot has the same frequency dependence with values 90° shifted.

Chapter 2

Finite difference modelling

The analytical model presented in the previous chapter is best suited for the evaluation of the system's dynamics in some peculiar conditions. First of all transient dynamics is not included in the analysis and secondly the load dynamic behaviour of the load must be reduced to that of a point mass. Obviously more complex loads and driving signals can be analysed by superposition of different load masses and input signals. Nevertheless, non-linear behaviour cannot be taken into account.

A way to overcome such problems is to implement a numerical model of the piezoelectric plate. The finite difference method is a powerful tool for the analysis of any kind of system, either mechanical, electrical, fluid-dynamic, or a combination thereof. A finite difference technique for modelling piezoelectric plate in stretch mode had been already presented in [26]: the model includes the driving circuitry as well. It is a straightforward method to implement and allows the analysis of transient phenomena, such as the response to a step voltage.

The finite difference modelling of a piezoeletric thin plate will be presented in the following sections. Some loading and constraining conditions will be taken into account, as well as the electric driving circuit.

2.1 Numerical analysis of single plate dynamics

Considering a single free plate, the pertinent constitutive and dynamic equations are those reported in the first chapter (see Eq. 1.1 and 1.1). Employing finite difference methods, the displacement $u(x,\tau)$ can be discretized in space and time above the two intervals $\left[-\frac{t}{2},\frac{t}{2}\right]$ and $[0,\tau_f]$ (see Fig. 2.1). Introducing two indexes i and j, the following variable substitutions hold

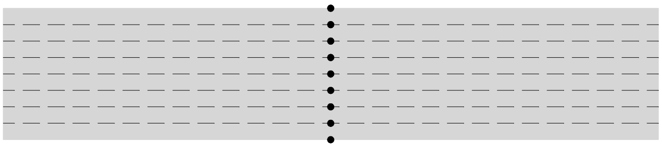

Figure 2.1: Thin plate spatial discretization

$$\begin{cases} x = -\frac{t}{2} + \frac{t}{M-1}(i-1) = -\frac{t}{2} + \delta(i-1) \\ \tau = \frac{\tau_f}{N-1}(j-1) = \chi(j-1) \end{cases} \tag{2.1}$$

where $i = 1, \dots, M$ and $j = 1, \dots, N$. The spatial and time coordinates of a grid point (i, j) could be expressed as x_i and τ^j. The plate is thus divided into $M-1$ elements of thickness δ and time is split in $N-1$ time steps of duration χ. Based on this definition, the displacement $u(x_i, \tau^j)$ can be written also as u_i^j. Displacements around a point of this grid can be found by Taylor's expansion (as shown in [18]) as

$$\begin{cases} u_i^{j+1} = u_i^j + \chi\left(\frac{\partial u}{\partial \tau}\right)_i^j + \frac{1}{2}\chi^2\left(\frac{\partial^2 u}{\partial \tau^2}\right)_i^j + \frac{1}{6}\chi^3\left(\frac{\partial^3 u}{\partial \tau^3}\right)_i^j + \frac{1}{24}\chi^4\left(\frac{\partial^4 u}{\partial \tau^4}\right)_i^j + \dots \\ u_i^{j-1} = u_i^j - \chi\left(\frac{\partial u}{\partial \tau}\right)_i^j + \frac{1}{2}\chi^2\left(\frac{\partial^2 u}{\partial \tau^2}\right)_i^j - \frac{1}{6}\chi^3\left(\frac{\partial^3 u}{\partial \tau^3}\right)_i^j + \frac{1}{24}\chi^4\left(\frac{\partial^4 u}{\partial \tau^4}\right)_i^j + \dots \\ u_{i+1}^j = u_i^j + \delta\left(\frac{\partial u}{\partial x}\right)_i^j + \frac{1}{2}\delta^2\left(\frac{\partial^2 u}{\partial x^2}\right)_i^j + \frac{1}{6}\delta^3\left(\frac{\partial^3 u}{\partial x^3}\right)_i^j + \frac{1}{24}\delta^4\left(\frac{\partial^4 u}{\partial x^4}\right)_i^j + \dots \\ u_{i-1}^j = u_i^j - \delta\left(\frac{\partial u}{\partial x}\right)_i^j + \frac{1}{2}\delta^2\left(\frac{\partial^2 u}{\partial x^2}\right)_i^j - \frac{1}{6}\delta^3\left(\frac{\partial^3 u}{\partial x^3}\right)_i^j + \frac{1}{24}\delta^4\left(\frac{\partial^4 u}{\partial x^4}\right)_i^j + \dots \end{cases} \tag{2.2}$$

These forward and backward expansions can be summed and rearranged, according to Eq. 1.4, yielding

$$\begin{aligned} \frac{1}{v^2}\left(\frac{\partial^2 u}{\partial \tau^2}\right)_i^j - \left(\frac{\partial^2 u}{\partial x^2}\right)_i^j = \frac{u_i^{j+1} - 2u_i^j + u_i^{j-1}}{v^2\chi^2} - \frac{u_{i+1}^j - 2u_i^j + u_{i-1}^j}{\delta^2} - \\ - \frac{1}{12}\frac{\chi^2}{v^2}\left(\frac{\partial^4 u}{\partial \tau^4}\right)_i^j + \frac{1}{12}\delta^2\left(\frac{\partial^4 u}{\partial x^4}\right)_i^j + \dots = 0 \end{aligned} \tag{2.3}$$

A useful relation between even-order derivatives of u can be found by differentiation of Eq. 1.4. For example, finding a relation between $u_{,xxxx}$ and $u_{,\tau\tau\tau\tau}$

$$\begin{cases} u_{,xxxx} = \frac{1}{v^2}u_{,\tau\tau xx} \\ u_{,\tau\tau\tau\tau} = v^2 u_{,xx\tau\tau} \end{cases} \Rightarrow u_{,xxxx} = \frac{1}{v^4}u_{,\tau\tau\tau\tau} \tag{2.4}$$

It must be noted that the process can be iterated and the relation between higher even-order derivatives can be found. Substituting Eq. 2.4 into Eq. 2.3 yields

$$\frac{1}{v^2}\left(\frac{\partial^2 u}{\partial \tau^2}\right)_i^j - \left(\frac{\partial^2 u}{\partial x^2}\right)_i^j = \frac{u_i^{j+1} - 2u_i^j + u_i^{j-1}}{v^2\chi^2} - \frac{u_{i+1}^j - 2u_i^j + u_{i-1}^j}{\delta^2} - \\ - \frac{1}{12}\left(\frac{\chi^2}{v^2} - \frac{\delta^2}{v^4}\right)\left(\frac{\partial^4 u}{\partial \tau^4}\right)_i^j + \cdots = 0$$

Choosing suitable values for h and χ, so that the relation

$$\chi^2 v^2 = \delta^2 \tag{2.5}$$

is satisfied, makes the truncation error null and therefore Eq. 2.3 can be written in a more compact form as

$$u_i^{j+1} = u_{i+1}^j + u_{i-1}^j - u_i^{j-1} \qquad i = 1, \ldots, M;\ j = 1, \ldots, N \tag{2.6}$$

Equation 2.6 allows calculating explicitly the displacement of all grid points at the following time step τ^{j+1} once the displacements at the time τ^{j-1} and τ^j are known for all grid points. Furthermore it must be noticed that the displacement of two more points are required for the solution of Eq. 1.4: those are u_0^j and u_{M+1}^j. These two points do not exist physically but are required for the computation of the spatial derivatives at the boundaries of the plate. They will be called hereafter ghost points, since they do not influence the dynamics of the system. The electric potential can be written as

$$\varphi_i^j = \frac{e}{\varepsilon^S} u_i^j + B_1^j x_i \tag{2.7}$$

based on Eq. 1.6. Imposing a voltage difference V_p^j between the electrodes, Eq. 2.7 allows expressing the integration constant B_1^j as

$$\varphi_M^j - \varphi_1^j = \frac{e}{\varepsilon^S}\left(u_M^j - u_1^j\right) + B_1^j t = V_p^j$$

$$B_1^j = \frac{V_p^j}{t} - \frac{e}{\varepsilon^S t}\left(u_M^j - u_1^j\right) \tag{2.8}$$

Mechanical stress and electric displacement at a grid point (i, j) can be written as

$$\begin{cases} T_i^j = \frac{\bar{c}^E}{2\delta}\left(u_{i+1}^j - u_{i-1}^j\right) - \frac{e^2}{\varepsilon^S t}\left(u_M^j - u_1^j\right) + \frac{e}{t}V_p^j \\ D^j = -\frac{\varepsilon^S}{t}V_p^j + \frac{e}{t}\left(u_M^j - u_1^j\right) \end{cases} \tag{2.9}$$

where it is well clear that the electric displacement is only time-dependent. The expression of charge Q, electric current I, and electric capacitance C are

$$\begin{cases} Q^j = \varepsilon^S \frac{A}{t} V_p^j - e\frac{A}{t}\left(u_M^j - u_1^j\right) \\ I^j = \varepsilon^S \frac{A}{2\chi t}\left(V_p^{j+1} - V_p^{j-1}\right) - e\frac{A}{2\chi t}\left(u_M^{j+1} - u_M^{j-1} - u_1^{j+1} + u_1^{j-1}\right) \\ C^j = \varepsilon^S \frac{A}{t} - e\frac{A}{t}\frac{u_M^j - u_1^j}{V_p^j} \end{cases} \tag{2.10}$$

where the centered difference formula has been employed for the calculation of the current I^j. The expression of the capacitance shows very well the contribution of the piezoelectric effect: while the material is not deformed ($u_M^j = u_1^j = 0$) the capacitance is the customary one; in case the plate undergoes deformation, the capacitance increases (please notice that the piezoelectric stress constant e is negative). The expression of the current shows the link between the mechanical and the electric field, being composed of two separate terms. All these quantities can be calculated only once the voltage across the piezoelectric material is known. To do so, the circuit equation

$$V_s^j = RI^j + V_p^j \tag{2.11}$$

must be considered (the electric circuit analysed is the same shown in Fig. 1.5). Overall the dynamics of a piezoelectric plate is modelled by the following system of equations

$$\begin{cases} u_i^{j+1} = u_{i+1}^j + u_{i-1}^j - u_i^{j-1} \qquad i = 1, \ldots, M; \; j = 1, \ldots, N \\ V_s^j = RI^j + V_p^j \end{cases} \tag{2.12}$$

where boundary conditions must be included for obtaining a solution.

2.2 Boundary and initial conditions formulation

The solution to the system of equations Eq. 2.12 can be found only when boundary and initial conditions are specified. While initial conditions allows calculating the values of u_i^j and V_p^j at the first time steps, boundary conditions helps defining a general scheme for the solution to the system Eq. 2.12. Boundary conditions will be specified for all four the cases reported in chapter one.

2.2.1 Unconstrained plate

The boundary conditions of Eq. 1.13 can be written explicitly by employing the stress equation Eq. 2.9

$$\begin{cases} T_1^j = \frac{\bar{c}^E}{2\delta}\left(u_{M+1}^j - u_{M-1}^j\right) - \frac{e^2}{\varepsilon^S t}\left(u_M^j - u_1^j\right) + \frac{e}{t}V_p^j = 0 \\ T_M^j = \frac{\bar{c}^E}{2\delta}\left(u_2^j - u_0^j\right) - \frac{e^2}{\varepsilon^S t}\left(u_M^j - u_1^j\right) + \frac{e}{t}V_p^j = 0 \end{cases} \tag{2.13}$$

These formulas contains two unknowns, u_{M+1}^j and u_0^j, given that the voltage V_p^j has been previously calculated. Indeed, the circuit equation can be re-written as

$$V_s^j = V_p^j + \varepsilon^S R\frac{A}{2\chi t}\left(V_p^{j+1} - V_p^{j-1}\right) - eR\frac{A}{2\chi t}\left(u_M^{j+1} - u_M^{j-1} - u_1^{j+1} + u_1^{j-1}\right) \tag{2.14}$$

expression that in fact holds true for any boundary conditions and allows calculating the value of V_p^{j+1} once u_1^{j+1} and u_M^{j+1} are known. These last two variables can be calculated starting from the dynamic equation Eq. 2.6. In conclusion, the system of equations finds a solution in

$$\begin{cases} u_0^j = u_2^j + \frac{2\delta e}{\bar{c}^E}\left(\frac{V_p^j}{t} - \frac{e}{\varepsilon^S t}(u_M^j - u_1^j)\right) \\ u_{M+1}^j = u_{M-1}^j - \frac{2\delta e}{\bar{c}^E}\left(\frac{V_p^j}{t} - \frac{e}{\varepsilon^S t}(u_M^j - u_1^j)\right) \\ u_i^{j+1} = u_{i+1}^j + u_{i-1}^j - u_i^{j-1} \qquad i = 1, \ldots, M \\ V_p^{j+1} = V_p^{j-1} + \frac{2\chi t}{\varepsilon^S RA}\left(V_s^j - V_p^j\right) + \frac{e}{\varepsilon^S}\left(u_M^{j+1} - u_M^{j-1} - u_1^{j+1} + u_1^{j-1}\right) \end{cases} \tag{2.15}$$

The solution to the system of equations is based on the assumption that the displacement of all points at the time τ^j is known, as well as the voltage V_p^j. Such assumption might seem questionable, given that a different formulation of the current expression (i.e. the backward difference formula) could lead to different results. In fact the linear theory of piezoelectricity states that the electric field can be considered to be quasi-stationary, that means transient phenomena in the electric circuit occur in a much smaller fraction of time with respect to those related to the piezo-mechanical part. Such hypothesis will be later verified when the electric circuit time constant will be compared to the mechanical resonant period.

2.2.2 Inertially loaded unconstrained plate

The addition of an inertial load of mass m changes the boundary conditions Eq. 2.13 in

$$\begin{cases} T_1^j = \frac{\bar{c}^E}{2\delta}\left(u_2^j - u_0^j\right) - \frac{e^2}{\varepsilon^S t}\left(u_M^j - u_1^j\right) + \frac{e}{t}V_p^j = \frac{m}{A}\frac{u_1^{j+1} - 2u_1^j + u_1^{j-1}}{\chi^2} \\ T_M^j = \frac{\bar{c}^E}{2\delta}\left(u_{M+1}^j - u_{M-1}^j\right) - \frac{e^2}{\varepsilon^S t}\left(u_M^j - u_1^j\right) + \frac{e}{t}V_p^j = -\frac{m}{A}\frac{u_M^{j+1} - 2u_M^j + u_M^{j-1}}{\chi^2} \end{cases} \tag{2.16}$$

The two equations contain four unknowns, thus require two more equations for finding a solution. The dynamic equation Eq. 2.6 for the upper and lower nodes 1 and M can be employed yielding

$$\begin{cases} \frac{\bar{c}^E}{2\delta}\left(u_2^j - u_0^j\right) - \frac{e^2}{\varepsilon^S t}\left(u_M^j - u_1^j\right) + \frac{e}{t}V_p^j = \mu\frac{u_1^{j+1}-2u_1^j+u_1^{j-1}}{\chi^2} \\ \frac{\bar{c}^E}{2\delta}\left(u_{M+1}^j - u_{M-1}^j\right) - \frac{e^2}{\varepsilon^S t}\left(u_M^j - u_1^j\right) + \frac{e}{t}V_p^j = -\mu\frac{u_M^{j+1}-2u_M^j+u_M^{j-1}}{\chi^2} \\ u_1^{j+1} = u_2^j + u_0^j - u_1^{j-1} \\ u_M^{j+1} = u_{M+1}^j + u_{M-1}^j - u_M^{j-1} \end{cases} \tag{2.17}$$

where μ has been defined as $\frac{m}{A}$. The solution to such system can be found as

$$\begin{cases} u_0^j = -u_2^j + 2\left(1 + \frac{2\delta}{\bar{c}^E}\frac{\mu}{\chi^2}\right)^{-1}\left(u_2^j + \frac{2\delta}{\chi^2}\frac{\mu}{\bar{c}^E}u_1^j + \right. \\ \qquad \left. + \frac{\delta}{\bar{c}^E}\frac{e}{t}\left(V_p^j - \frac{e}{\varepsilon^S}\left(u_M^j - u_1^j\right)\right)\right) \\ u_i^{j+1} = u_{i+1}^j + u_{i-1}^j - u_i^{j-1} \qquad i = 1, \dots, M \\ u_{M+1}^j = -u_{M-1}^j + \left(1 + \frac{2\delta}{\chi^2}\frac{\mu}{\bar{c}^E}\right)^{-1}\left(2u_{M-1}^j + 2\frac{2\delta}{\chi^2}\frac{\mu}{\bar{c}^E}u_M^j + \frac{2\delta}{\bar{c}^E} - \right. \\ \qquad \left. - \frac{2\delta}{t}\frac{e}{\bar{c}^E}\left(V_p^j - \frac{e}{\varepsilon^S}\left(u_M^j - u_1^j\right)\right)\right) \\ V_p^{j+1} = V_p^{j-1} + \frac{2\chi t}{\varepsilon^S RA}\left(V_s^j - V_p^j\right) + \frac{e}{\varepsilon^S}\left(u_M^{j+1} - u_M^{j-1} - u_1^{j+1} + u_1^{j-1}\right) \end{cases} \tag{2.18}$$

2.2.3 Constrained plate

In case of a constrained plate the boundary conditions are modified as follows

$$\begin{cases} u_1^j = 0 \\ T_M^j = \frac{\bar{c}^E}{2\delta}\left(u_2^j - u_0^j\right) - \frac{e^2}{\varepsilon^S t}\left(u_M^j - u_1^j\right) + \frac{e}{t}V_p^j = 0 \end{cases} \tag{2.19}$$

The results already found for the unconstrained plate in Eq. 2.15 are partly valid for this case as well. The solution to the system Eq. 2.19 is thus

$$\begin{cases} u_0^j = u_2^j \\ u_1^j = 0 \\ u_{M+1}^j = u_{M-1}^j - \frac{2\delta e}{\bar{c}^E}\left(\frac{V_p^j}{t} - \frac{e}{\varepsilon^S t}(u_M^j - u_1^j)\right) \\ u_i^{j+1} = u_{i+1}^j + u_{i-1}^j - u_i^{j-1} \qquad i = 2, \dots, M \\ V_p^{j+1} = V_p^{j-1} + \frac{2\chi t}{\varepsilon^S RA}\left(V_s^j - V_p^j\right) + \frac{e}{\varepsilon^S}\left(u_M^{j+1} - u_M^{j-1} - u_1^{j+1} + u_1^{j-1}\right) \end{cases} \tag{2.20}$$

2.2.4 Inertially loaded constrained plate

The addition of an inertial load to the system implies a change in the formulation of the boundary conditions. The stress on the unconstrained face of the plate is not always zero but it is variable according to the accelerations of the load. The system of equations Eq. 2.19 has to be modified in

$$\begin{cases} u_1^j = 0 \\ T_M^j = \frac{\bar{c}^E}{2\delta}\left(u_2^j - u_0^j\right) - \frac{e^2}{\varepsilon^S t}\left(u_M^j - u_1^j\right) + \frac{e}{t}V_p^j = -\frac{m}{A}\frac{u_M^{j+1} - 2u_M^j + u_M^{j-1}}{\chi^2} \end{cases} \tag{2.21}$$

This system finds a solution as

$$\begin{cases} u_0^j = u_2^j \\ u_1^j = 0 \\ u_i^{j+1} = u_{i+1}^j + u_{i-1}^j - u_i^{j-1} \qquad i = 2, \ldots, M \\ u_{M+1}^j = -u_{M-1}^j + \left(1 + \frac{2\delta}{\chi^2}\frac{\mu}{\bar{c}^E}\right)^{-1}\left(2u_{M-1}^j + 2\frac{2\delta}{\chi^2}\frac{\mu}{\bar{c}^E}u_M^j - \right. \\ \qquad \left. -\frac{2\delta}{t}\frac{e}{\bar{c}^E}\left(V_p^j - \frac{e}{\varepsilon^S}\left(u_M^j - u_1^j\right)\right)\right) \\ V_p^{j+1} = V_p^{j-1} + \frac{2\chi t}{\varepsilon^S RA}\left(V_s^j - V_p^j\right) + \frac{e}{\varepsilon^S}\left(u_M^{j+1} - u_M^{j-1} - u_1^{j+1} + u_1^{j-1}\right) \end{cases} \tag{2.22}$$

2.3 Simulations and commentary

The finite difference technique is a very simple kind of finite element modelling. As happens for any of this numerical solutions, a particular care must be taken in evaluating the accuracy of the results. As the method models a space and time dependent problem, convergence and accuracy have to be checked with respect to both.

In a finite element model the result of a simulation might depend on the number of elements involved in modelling the object under analysis. In the finite difference model presented there is a double discretization, both in space and time. As demonstrated, best results are achieved when a particular ratio between the two discretization steps is chosen (see Eq. 2.5).

A simple method to evaluate the accuracy and the convergence of the finite difference model of a piezoelectric thin plate is to give an input step voltage and to compare the resulting deformation and period of oscillation. The amplitude of the oscillation will be twice the static deformation, while the oscillating period will be approximately equal to the reciprocal of the first resonance frequency.

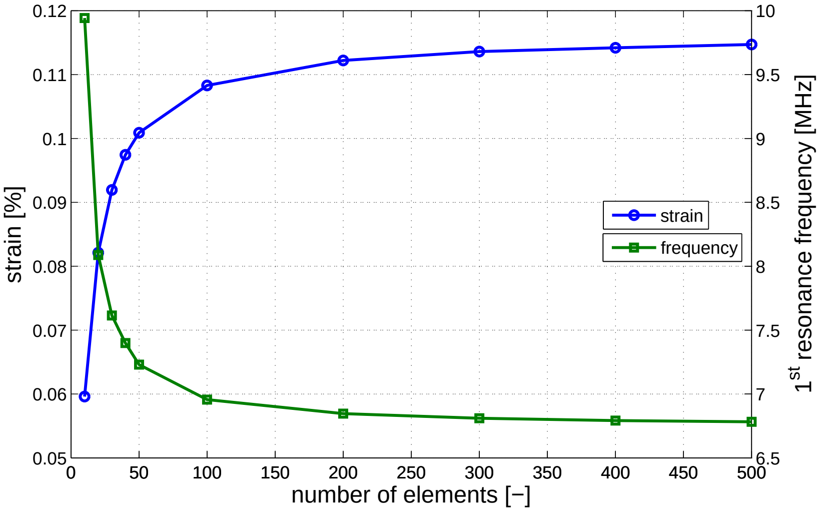

Figure 2.2: Thin plate model convergence

Figure 2.2 shows the values of the maximum strain and of the first resonance frequency as the number of elements increases. The simulations that were carried out consisted in inputting a 100 V step voltage to an undeformed thin plate with the same geometrical and material specifications as that employed in chapter one. Both maximum strain and first resonance frequency reach rapidly a “stable” value. The better accuracy due to employing a large number of elements has a downside: the computational time increases considerably.

Figure 2.3 reports the computational time taken to produce the aforementioned results (simulations run in Matlab, on a Intel Core 2 Duo 2.2 GHz processor equipped with 8 GB RAM). It can be noticed that the computational time shows a quadratic dependence on the number of elements. Therefore a trade-off between accuracy and computational time must be taken. It seems resonable to consider satisfactory the results obtained with 100 elements: further discretization does not bring tremendous improvements both with respect to deformation and dynamic behaviour, while the computational time is still quite limited.

2.3.1 FRF estimation

The frequency response function of a system can be estimated by giving an impulse and measuring the response. Then both the input signal and the response are analysed by means of the fast Fourier transforms and the FFR is calculated. Such method goes under the name of impact testing and is a very common practice in many engineering

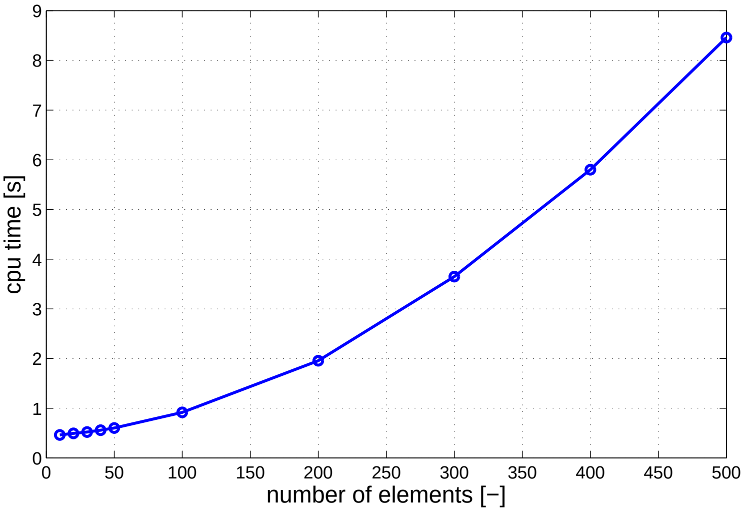

Figure 2.3: CPU time as element number increases

areas.

The procedure can be employed numerically too for estimating the FRF of a system modelled by the finite difference method. The input signal can be obviously reproduced numerically and the simulation gives as output the response. The numerical techniques for the analysis of the data are the same as those employed in the experimental estimation of the FRF.

One way to give an excitation to a system is to input a inpulse of very short duration. The shorter is the duration of the signal, the higher the frequencies to be excited. The longer the acquisition/simulation time is, the broader is the frequency spectrum in the range lower end. The shape of the impulsive signal influences the way the frequencies are excited. Very good results can be achieved by inputting a impulse shaped as a half-sine (see Fig. 2.4).

The fast Fourier transform (FFT) of the half sine impulse is shown in Fig. 2.5. This FFT is calculated for a unitary amplitude impulse signal whose duration is about 10^{-9} seconds. The simulation time is $2 \cdot 10^{-5}$ s. The remarkable result is that the signal give an homogeneous excitation in a very broad frequency range. The lower and upper range boundaries can be calculated approximately as the inverse of the simulation time and the inverse of the impulse duration respectively. In fact at the upper frequency boundary defined in this way overestimates the region in which the FFT of the signal still presents the same gain and phase at lower frequencies. According to particular needs, the upper frequency bound can be considered one or two order of magnitude

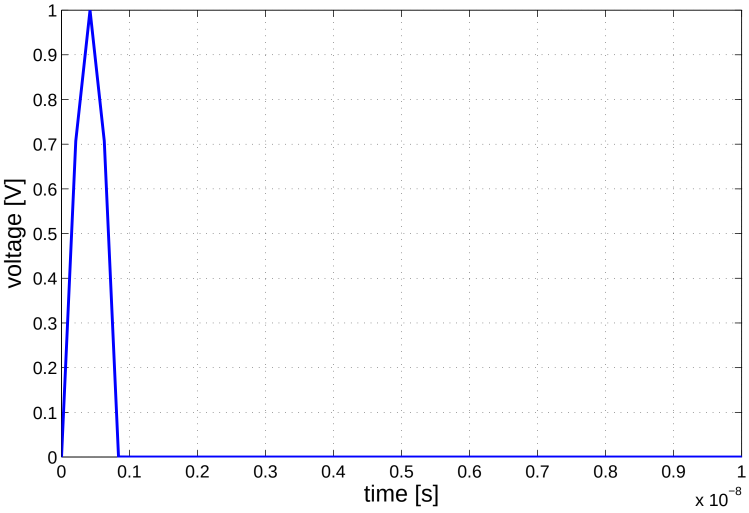

Figure 2.4: 1 V half sine pulse

lower.

Nevertheless, the half sine pulse excitation achieves the remarkable goal of giving a constant excitation in a broad frequency spectrum. Furthermore, numerically this range can be easily controlled, given that the time discretization reproduces well the shape of the signal. The chosen spatial discretization of 100 elements implied an integration time step of $2.1 \cdot 10^{-10}$ s, which is quite satisfactory in this respect.

Figures from 2.6 to 2.9 reports the strain and current FRF's of the thin plate analysed in chapter one, comparing the results with the finite difference simulations. Figures 2.6 and 2.7 show the FRF's of an unloaded constrained thin plate, while Fig. 2.8 and 2.9 represent the behavior of the system when inertially loaded. In this case the load mass equals the piezoelectric plate mass, i.e. $k_m = 1$.

The finite difference model shows an adequate to good dynamic description of the system dynamics with respect to the analytical solution. The strain FRF of the unloaded thin plate matches very well the one calculated analyticaly at low frequencies while there is only an asymptotical correspondence of the dynamic behaviour at high frequencies, that is for frequencies higher than the first resonance. In particular the first resonance frequency resulting from finite difference modelling of the system dynamics differs quite drastically from the analytical model. Indeed a peak can be spotted at about 7.5 MHz, while the resonace frequency calculated analytically is at 5.28 MHz. It is interesting to notice that the resonance frequency estimated with the procedure on which Fig. 2.2 is based yields slightly different results. Reading the plot of Fig. 2.2 the

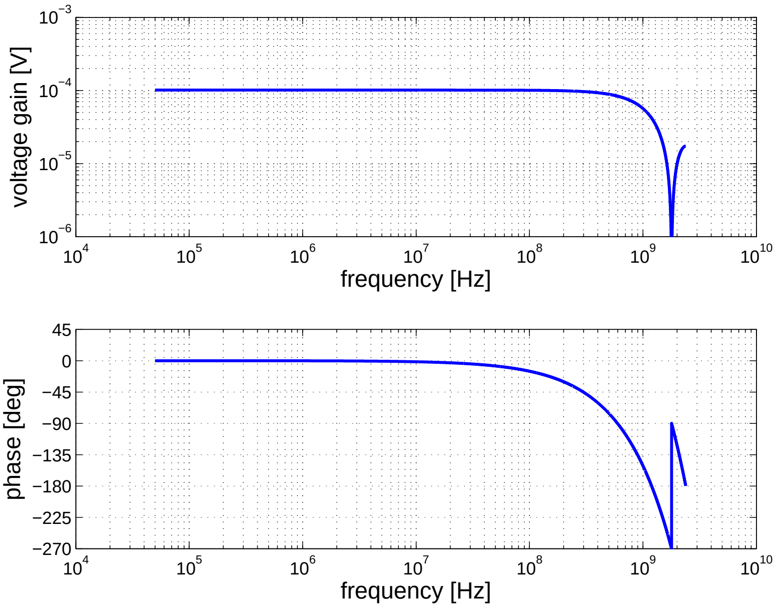

Figure 2.5: 1 V half sine pulse - FFT

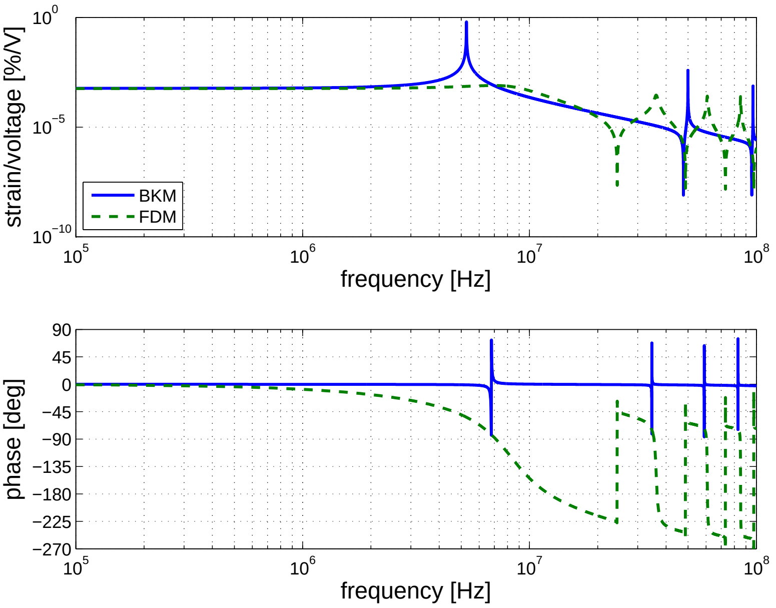

Figure 2.6: Unloaded constrained plate - Strain FRF comparison between BKM and FDM

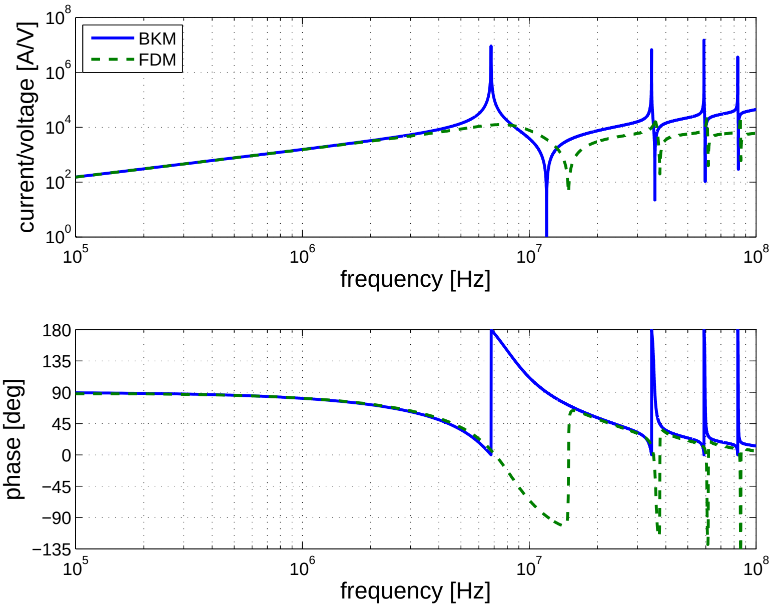

Figure 2.7: Unloaded constrained plate - Current FRF comparison between BKM and FDM

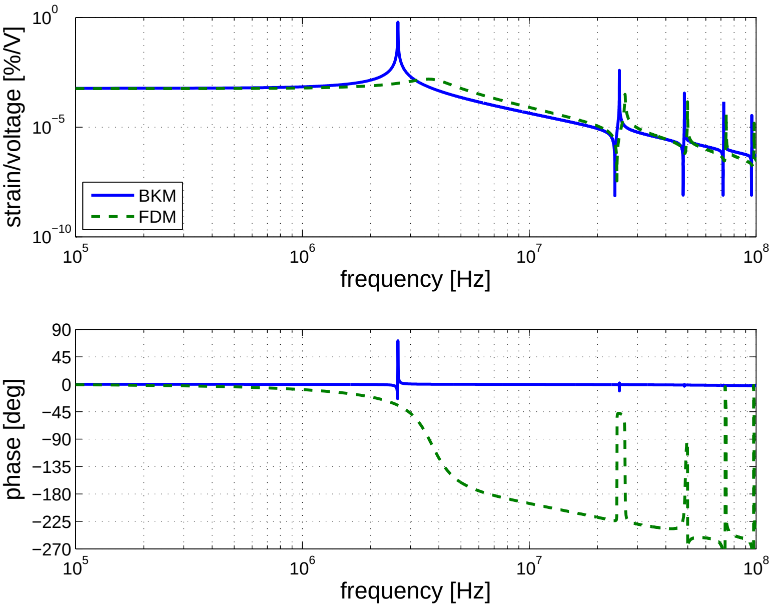

Figure 2.8: Inertially loaded constrained plate - Strain FRF comparison between BKM and FDM

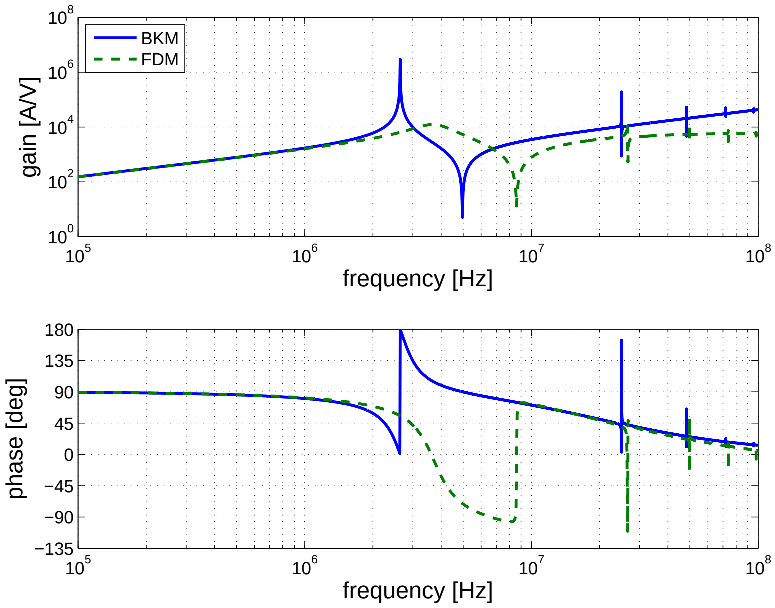

Figure 2.9: Inertially loaded constrained plate - Current FRF comparison between BKM and FDM

first resonance frequency occurs at about 7 Mhz, instead of 7.5 MHz. The conclusion to be drawn is that the shape of the excitation signal influence the calculated FRF.

Chapter 3

Piezoelectric multilayer actuators

Far more interesting for the mechanical engineer is the piezoelectric multilayer actuator (MLA). Indeed, the biggest downside of piezoelectric materials is their limited deformation induced by electric field. Altough large enough in certain applications such as MEMs and NEMs (nano- and micro- electromechanical systems), bulk piezoelectric devices (that is devices made by a single piece of piezoelectric material) do not find applications in larger scale mechanical systems, with the remarkable exception of some piezoelectric motors.

The piezoelectric MLA, made by a stack of single piezoelectric plates or disks, overcomes two large limitations: the small deformations and strokes, and the high driving voltages. At the time this document is written, commercially available piezoelectric MLAs reach 1 mm strokes with driving voltages of 120 V.

3.1 Multilayer actuator modelling

A multilayer stack is basically made by a series of piezoelectric thin plates and electrodes (see Fig. 3). Due to manufacturing considerations, layers and electrodes can be arranged in different configurations (as shown in Fig. 3.1). The easiest solution, from a theoretical point of view, is the alternation of layers of piezoelectric material and electroded surfaces that span the whole actuator's width (Fig. 3.1.a). This *plate-through* solution presents some insulation issues: the electrodes side must be connected in parallel to the driving electric circuit in an alternating way. Every two conducting layers there must be an insulating coating that prevents short circuits.

Insulating might be problematic, thus alternative configurations were introduced. The *interdigital* configuration sees the electrodes occupy only a portion of the actuator's

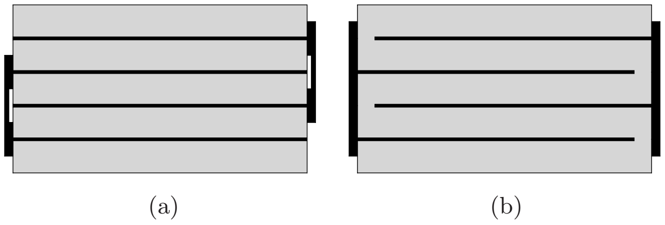
(a) (b)

Figure 3.1: Plate-electrode configurations

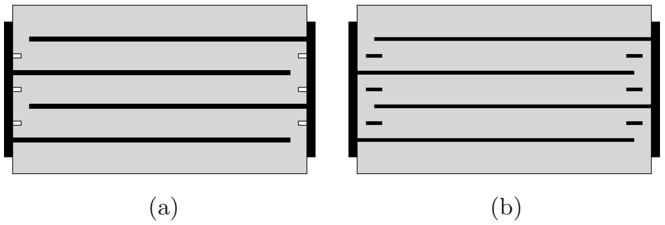
(a) (b)

Figure 3.2: Solutions for relieving stress and electric field concentrations

cross section (Fig. 3.1.b). Employing this solution, there is no concern about short circuiting, although other problems arise. In the areas close to the actuator's outer surface there is no deformation, since the electrodes do not cover the whole area. This causes mechanical stress and electric field concentration (field lines are not parallel to the actuator axis). To overcome these drawbacks, some modification to the interdigital design were proposed. One solution aims at relieving mechanical stress by making some slits where the electrodes end (Fig. 3.2.a). Another solution allows reducing the electric field concentration by putting some disconnected electrodes in the piezoelectric layer (Fig. 3.2.b).

3.1.1 Multilayer statics

The overall displacement can be approximated considering the stack made by a series of L piezoelectric plates and disregarding the influence of the electrodes deformation. When each plate is subject to a displacement ${}^{k}u$, the stack undergoes an elongation equals to

$$u = L\,{}^{k}u$$

It should be noted that larger displacements can be obtained without raising the driving voltage. Low driving voltages result from very thin layers of piezoelectric material and electrodes, which are the remarkable outcome of improved manufacturing

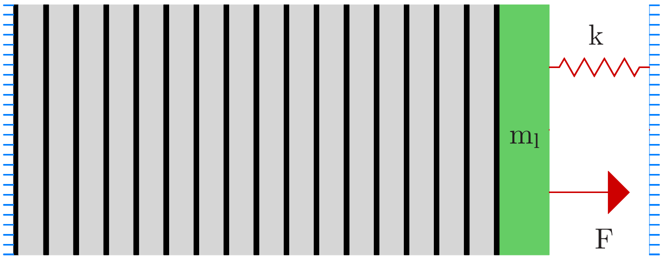

Figure 3.3: Multilayer actuator and loading conditions

processes, known as tape-casting methods. Laminated ceramics with printed electrodes are laminated and co-fired with internal electrodes.

3.2 System's description

The multilayer actuator shall be constituted by L layers of thickness t. Each layer is bound by two electrodes that allow applying a voltage V_p. The actuator is fixed at one end, while the opposite end is free to move and can be loaded by a force F (see Fig. 3.3).

In order to simplify notation, Eq. 1.1 and 1.2 can be greatly simplified if the displacement variable is changed by the linear transformation

$$\bar{u} = \frac{e}{\varepsilon^S} u \tag{3.1}$$

as

$$\begin{cases} T = \frac{c^E \varepsilon^S}{e} \bar{u}_{,x} + e\varphi_{,x} \\ D = \varepsilon^S \left(\bar{u}_{,x} - \varphi_{,x} \right) \\ \frac{c^E \varepsilon^S}{e} \bar{u}_{,xx} + e\varphi_{,xx} = \rho \frac{\varepsilon^S}{e} \bar{u}_{,\tau\tau} \\ \bar{u}_{,xx} - \varphi_{,xx} = 0 \end{cases} \tag{3.2}$$

3.3 Hypotheses

Let $\bar{u}$ be the transformed variable that describes the displacement of the layers. The variable $\bar{u}$ is dependent on the coordinate x and the time τ. Defining the sub-domains R_k upon which $\bar{u}$ is defined as $R_k = [(k-1)t, kt] \times [0, +\infty)$, it is required that $u \in \left(\bigcup_{k=1}^{L} C^2(R_k) \right) \cap C \left(\bigcup_{k=1}^{L} R_k \right)$, i.e. that $\bar{u}$ can be differentiated twice with respect to time and space within a sub-domain R_k and that is continuous across neighboring sub-domains.

3.4 Formulation of the equations

3.4.1 Dynamic equations

For each layer, the set of equations Eq. 3.2 can be written as

$$\begin{cases} T^k = \frac{c^E \varepsilon^S}{e} \bar{u}^k_{,x} + e\varphi^k_{,x} \\ D^k = \varepsilon^S \left(\bar{u}^k_{,x} - \varphi^k_{,x} \right) \\ \frac{c^E \varepsilon^S}{e} \bar{u}^k_{,xx} + e\varphi^k_{,xx} = \rho \frac{\varepsilon^S}{e} \bar{u}^k_{,\tau\tau} \\ \bar{u}^k_{,xx} - \varphi^k_{,xx} = 0 \end{cases} \qquad k = 1, \dots, L \tag{3.3}$$

Expressing the electric potential derivative $\varphi^k_{,x}$ as a function of displacement derivative as $\varphi^k_{,x} = \bar{u}^k_{,x} + B^k(\tau)$, one gets

$$\begin{cases} T^k = \left(\frac{c^E \varepsilon^S}{e} + e \right) \bar{u}^k_{,x} + eB^k \\ D^k = -\varepsilon^S B^k \\ \left(\frac{c^E \varepsilon^S}{e} + e \right) \bar{u}^k_{,xx} = \rho \frac{\varepsilon^S}{e} \bar{u}^k_{,\tau\tau} \\ \varphi^k_{,x} = \bar{u}^k_{,x} + B^k \end{cases} \qquad k = 1, \dots, L \tag{3.4}$$

Recalling the definition of the coefficients $\bar{c}^E = 1 + \frac{c^E \varepsilon^S}{e^2}$ and $v^2 = \frac{\bar{c}^E e^2}{\rho \varepsilon^S}$ yields

$$\begin{cases} T^k = e \left(\bar{c}^E \bar{u}^k_{,x} + B^k \right) \\ D^k = -\varepsilon^S B^k \\ \bar{u}^k_{,\tau\tau} - v^2 \bar{u}^k_{,xx} = 0 \\ \varphi^k = \bar{u}^k + B^k x \end{cases} \qquad k = 1, \dots, L \tag{3.5}$$

3.4.2 Boundary and initial conditions

Boundary and initial conditions are such as

1. The piezoelectric actuator is fixed at one end:

$$\bar{u}^1(0, \tau) = 0$$

2. Every layer except the free end one is fixed to a neighboring one:

$$\bar{u}^k(kt, \tau) = \bar{u}^{k+1}(kt, \tau) \qquad k = 1, \dots, L-1$$

$$T^{k+1}(kt, \tau) = T^k(kt, \tau) + \mu_e \frac{\varepsilon^S}{e} \bar{u}^k_{,\tau\tau}(kt, \tau) \qquad k = 1, \dots, L-1$$

where μ_e is the electrode mass per unit area. The latter can be re-written as

$$T^k(kt, \tau) = e \left(\bar{c}^E \bar{u}^{k+1}_{,x}(kt, \tau) + B^{k+1} \right) - \mu_e \frac{\varepsilon^S}{e} \bar{u}^k_{,\tau\tau}(kt, \tau)$$

3. A voltage is applied to each layer:

$$V_p^k(\tau) = \varphi^k(kt,\tau) - \varphi^k((k-1)t,\tau) \qquad k = 1,\dots,L$$

   This condition can be re-written as

$$V_p^k(\tau) = \bar{u}^k(kt,\tau) - \bar{u}^k((k-1)t,\tau) + tB^k \qquad k = 1,\dots,L$$

4. The mechanical stress acting upon the free end shall be given by an applied force, an inertial load, and an elastic load:

$$T^L(Lt,\tau) = f(\tau) - (\mu_l + \mu_e)\frac{\varepsilon^S}{e}\bar{u}^L_{,\tau\tau}(Lt,\tau) - \kappa\frac{\varepsilon^S}{e}\bar{u}^L(Lt,\tau)$$

   where $f = \frac{F}{A}$, $\kappa = \frac{k}{A}$ and $\mu_l = \frac{m_l}{A}$

5. The actuator is initially undeformed:

$$\bar{u}^k(x,0) = 0$$

3.4.3 Boundary equations formulation

Boundary conditions equations can be simplified following a particular scheme. As the stress on the free end can be expressed as a function of F and $\bar{u}^L$ only, B^L can be calculated as well. The voltage condition on layer L can be now expressed only as a function of F and $\bar{u}^L$.

The equality $T^k(kt,\tau) = T^{k+1}(kt,\tau) - \mu_e\frac{\varepsilon^S}{e}\bar{u}^k_{,\tau\tau}(kt,\tau)$ allows progressing to inner layers as Tab. 3.1 shows. The explicit expression of B^k can be substituted into that of V_p^k yielding

$$V_p^k = \bar{u}^k(kt,\tau) - \bar{u}^k((k-1)t,\tau) + \frac{t}{e}T^k(kt,\tau) - t\bar{c}^E\bar{u}^k_{,x}(kt,\tau) \tag{3.6}$$

and once more $T^k(kt,\tau)$ can be re-written as

$$T^k(kt,\tau) = e\bar{c}^E\bar{u}^{k+1}_{,x}(kt,\tau) - e\bar{c}^E\bar{u}^{k+1}_{,x}((k+1)t,\tau) + T^{k+1}((k+1)t,\tau) - \mu_e\frac{\varepsilon^S}{e}\bar{u}^k_{,\tau\tau}(kt,\tau) \tag{3.7}$$

giving a more compact notation for the k^{th} voltage equation

$$\begin{aligned} V_p^k &= \bar{u}^k(kt,\tau) - \bar{u}^k((k-1)t,\tau) - t\bar{c}^E\bar{u}^k_{,x}(kt,\tau) + \\ &+ t\bar{c}^E\sum_{h=j}^{L-1} u^{h+1}_{,x}(ht,\tau) - u^{h+1}_{,x}((h+1)t,\tau) - \mu_e\frac{\varepsilon^S}{\bar{c}^E e^2}u^h_{,\tau\tau}(ht,\tau) + \frac{t}{e}T^L(Lt,\tau) \qquad k = 1,\dots,L-1 \end{aligned} \tag{3.8}$$

layer	$T^k(kt,\tau)$	eB^k	V_p^k
L	$f(\tau)-(\mu_l+\mu_e)\frac{\varepsilon^S}{e}\bar{u}^L_{,\tau\tau}(Lt,\tau)-\kappa\frac{\varepsilon^S}{e}\bar{u}^L(Lt,\tau)$	$\frac{1}{e}T^L(Lt,\tau)-\bar{c}^E\bar{u}^L_{,x}(Lt,\tau)$	$\bar{u}^L((L)t,\tau)-\bar{u}^L((L-1)t,\tau)+teB^L$
L-1	$e\bar{c}^E\bar{u}^L_{,x}((L-1)t,\tau)+eB^L-\mu_e\frac{\varepsilon^S}{e}\bar{u}^{L-1}_{,\tau\tau}((L-1)t,\tau)$	$T^{L-1}((L-1)t,\tau)-e\bar{c}^E\bar{u}^{L-1}_{,x}((L-1)t,\tau)$	$\bar{u}^{L-1}((L-1)t,\tau)-\bar{u}^{L-1}((L-2)t,\tau)+teB^{L-1}$
…	…	…	…
k	$e\bar{c}^E\bar{u}^{k+1}_{,x}(kt,\tau)+eB^{k+1}-\mu_e\frac{\varepsilon^S}{e}\bar{u}^k_{,\tau\tau}(kt,\tau)$	$T^k(kt,\tau)-e\bar{c}^E\bar{u}^k_{,x}(kt,\tau)$	$\bar{u}^k(kt,\tau)-\bar{u}^k((k-1)t,\tau)+teB^k$
…	…	…	…
2	$e\bar{c}^E u^3_{,x}(2t,\tau)+eB^3-\mu_e\frac{\varepsilon^S}{e}\bar{u}^2_{,\tau\tau}(2t,\tau)$	$T^2(2t,\tau)-e\bar{c}^E\bar{u}^2_{,x}(2t,\tau)$	$\bar{u}^2(2t,\tau)-\bar{u}^2(t,\tau)+teB^2$
1	$e\bar{c}^E\bar{u}^2_{,x}(t,\tau)+eB^2-\mu_e\frac{\varepsilon^S}{e}\bar{u}^1_{,\tau\tau}(t,\tau)$	$T^1(t,\tau)-e\bar{c}^E\bar{u}^1_{,x}(t,\tau)$	$\bar{u}^1(t,\tau)+teB^1$

Table 3.1: Boundary conditions

The explicit formulation of the voltage equation for the layer L can be read in Tab. 3.1. Subtracting V_p^{k-1} from V_p^k yields:

$$\begin{aligned}&V_p^k - V_p^{k-1} = \bar{u}^k(kt,\tau) - 2\bar{u}^k((k-1)t,\tau) + \bar{u}^{k-1}((k-2)t,\tau)+\\ &+t\bar{c}^E\bar{u}^{k-1}_{,x}((k-1)t,\tau)-t\bar{c}^E\bar{u}^{k+}_{,x}((k-1)t,\tau)+\mu_e t\frac{\varepsilon^S}{e^2}\bar{u}^{k-1}_{,\tau\tau}((k-1)t,\tau) \qquad k=2,\dots,L-1\end{aligned} \tag{3.9}$$

This result can be extended to $k = 2, \dots, L$. For V_p^L

$$\begin{aligned}V_p^L - \frac{t}{e}f(\tau) = \bar{u}^L(Lt,\tau) - \bar{u}^L((L-1)t,\tau)-&\\ -\frac{t\varepsilon^S}{e^2}(\mu_e+\mu_l)\bar{u}^L_{,\tau\tau}(Lt,\tau) - \kappa t\frac{\varepsilon^S}{e^2}\bar{u}^L(Lt,\tau) - t\bar{c}^E\bar{u}^L_{,x}(Lt,\tau)&\end{aligned} \tag{3.10}$$

Boundary conditions constitute a set of $2L$ equations. They can be summed up as

$$\begin{cases}\bar{u}^L(Lt,\tau) - \bar{u}^L((L-1)t,\tau) - \frac{t\varepsilon^S}{e^2}(\mu_e+\mu_l)\bar{u}^L_{,\tau\tau}(Lt,\tau) - \kappa t\frac{\varepsilon^S}{e^2}\bar{u}^L(Lt,\tau)-\\ -t\bar{c}^E\bar{u}^L_{,x}(Lt,\tau) = V_p^L - \frac{t}{e}f(\tau)\\ \\ \bar{u}^k(kt,\tau) - 2\bar{u}^k((k-1)t,\tau) + \bar{u}^{k-1}((k-2)t,\tau) + t\bar{c}^E\bar{u}^{k-1}_{,x}((k-1)t,\tau)-\\ -t\bar{c}^E\bar{u}^{k+}_{,x}((k-1)t,\tau) + \mu_e t\frac{\varepsilon^S}{e^2}\bar{u}^{k-1}_{,\tau\tau}((k-1)t,\tau) = V_p^k - V_p^{k-1} \qquad k=2,\dots,L\\ \\ \bar{u}^k(kt,\tau) = \bar{u}^{k+1}(kt,\tau) \qquad k=1,\dots,L-1\\ \\ \bar{u}^1(0,\tau) = 0\end{cases} \tag{3.11}$$

3.5 Solution

The dynamic equation Eq. 3.5 is linear, as well as boundary conditions expressed in Eq. 3.11. Considering the external actions V_p^k and F, a function G_k that groups them is defined as

$$\begin{aligned}&G_L = V_p^L - \tfrac{t}{e}f\\ &G_{k-1} = V_p^k - V_p^{k-1} \qquad k=2,\dots,L\end{aligned} \tag{3.12}$$

Because of the linearity of the equations, if $\bar{u}$ is a solution associated with G_k and $\tilde{\bar{u}}$ associated with $\tilde{G}_k$, $\bar{u}+\tilde{\bar{u}}$ is a solution associated with $G_k+\tilde{G}_k$. The generic solution $\bar{u}$ to the problem is such as

$$\bar{u}^k(x,\tau) = X_k(x)\Theta(\tau) \tag{3.13}$$

where $X \in \left(\bigcup_{k=1}^{L} C^2([(k-1)t, kt])\right) \cap C([0, Lt])$, and $X_k = X_{\chi_{[(k-1)t,kt]}}$. The dynamic equation can be re-written as

$$\frac{\Theta''(\tau)}{\Theta(\tau)} = v^2 \frac{X_k''(x)}{X_k(x)} = -\lambda \tag{3.14}$$

where λ is a constant dependent on G_k. Boundary conditions Eq. 3.11 can be re-written as

$$\begin{cases} \left(\left(1 - \kappa\frac{t\varepsilon^S}{e^2}\right) X_L(Lt) - X_L((L-1)t) + \lambda\frac{t\varepsilon^S}{e^2}(\mu_e + \mu_l)X_L(Lt) - t\bar{c}^E X_L'(Lt)\right)\Theta(\tau) = G_L \\ \\ \big(X_k(kt) - 2X_k((k-1)t) + X_{k-1}((k-2)t) + t\bar{c}^E X_{k-1}'((k-1)t) - \\ \qquad -t\bar{c}^E X_k'((k-1)t) - \lambda\mu_e\frac{t\varepsilon^S}{e^2}X_{k-1}((k-1)t)\big)\Theta(\tau) = G_{k-1} \qquad k = 2,\dots,L \\ \\ X_k(kt) = X_{k+1}(kt) \qquad k = 1,\dots,L-1 \\ \\ X_1(0) = 0 \end{cases} \tag{3.15}$$

3.5.1 Positive parameter

Let $\lambda = \omega^2$, the solution $\bar{u}^k$ can be written as

$$\bar{u}^k(x,\tau) = \left(r_k \cos\left(\frac{\omega}{v}x\right) + q_k \sin\left(\frac{\omega}{v}x\right)\right)\sin(\omega\tau) \tag{3.16}$$

The first derivative with respect to x of Eq. 3.16 is

$$\bar{u}^k_{,x}(x,\tau) = \frac{\omega}{v}\left(-r_k \sin\left(\frac{\omega}{v}x\right) + q_k \cos\left(\frac{\omega}{v}x\right)\right)\sin(\omega\tau) \tag{3.17}$$

This solution implies that G_k is either null or equal to $g_k \sin(\omega\tau)$. In the most generic case, the boundary conditions can be written as

$$\left\{\begin{array}{l}
r_L \left(\left(1-\kappa\frac{t\varepsilon^S}{e^2}\right)\cos\left(Lt\frac{\omega}{v}\right)-\cos\left((L-1)t\frac{\omega}{v}\right)+\omega^2\frac{t\varepsilon^S}{e^2}(\mu_e+\mu_l)\cos\left(Lt\frac{\omega}{v}\right)+\right.\\
\qquad\left.+t\bar{c}^E\frac{\omega}{v}\sin\left(Lt\frac{\omega}{v}\right)\right)+q_L\left(\left(1-\kappa\frac{t\varepsilon^S}{e^2}\right)\sin\left(Lt\frac{\omega}{v}\right)-\sin\left((L-1)t\frac{\omega}{v}\right)+\right.\\
\qquad\left.+\omega^2\frac{t\varepsilon^S}{e^2}(\mu_e+\mu_l)\sin\left(Lt\frac{\omega}{v}\right)-t\bar{c}^E\frac{\omega}{v}\cos\left(Lt\frac{\omega}{v}\right)\right)=g_L\\
\\
r_k\left(\cos\left(kt\frac{\omega}{v}\right)-2\cos\left((k-1)t\frac{\omega}{v}\right)+t\bar{c}^E\frac{\omega}{v}\sin\left((k-1)t\frac{\omega}{v}\right)\right)+\\
\qquad+q_k\left(\sin\left(kt\frac{\omega}{v}\right)-2\sin\left((k-1)t\frac{\omega}{v}\right)-t\bar{c}^E\frac{\omega}{v}\cos\left((k-1)t\frac{\omega}{v}\right)\right)+\\
\qquad+r_{k-1}\left(\cos\left((k-2)t\frac{\omega}{v}\right)-t\bar{c}^E\frac{\omega}{v}\sin\left((k-1)t\frac{\omega}{v}\right)-\omega^2\mu_e\frac{t\varepsilon^S}{e^2}\cos\left((k-1)t\frac{\omega}{v}\right)\right)+\\
\qquad+q_{k-1}\left(\sin\left((k-2)t\frac{\omega}{v}\right)+\cos\left((k-1)t\frac{\omega}{v}\right)-\omega^2\mu_e\frac{t\varepsilon^S}{e^2}\sin\left((k-1)t\frac{\omega}{v}\right)\right)=g_{k-1}\\
\qquad\qquad\qquad k=2,\ldots,L\\
\\
r_{k+1}\cos\left(kt\frac{\omega}{v}\right)+q_{k+1}\sin\left(kt\frac{\omega}{v}\right)-r_k\cos\left(kt\frac{\omega}{v}\right)-q_k\sin\left(kt\frac{\omega}{v}\right)=0 \qquad k=1,\ldots,L-1\\
\\
r_1=0
\end{array}\right. \tag{3.18}$$

It is convenient, for a computer code implementation, to express the system of equations in matrix form. Defining

$$\begin{aligned}
\boldsymbol{p} &= \{r_1,\ldots,r_L,q_1,\ldots,q_L\}^{\mathrm{T}}\\
\boldsymbol{g} &= \{0,\ldots,g_L,0,\ldots,0\}^{\mathrm{T}}
\end{aligned} \tag{3.19}$$

and

$$P = \begin{bmatrix}
p_{1,1} & p_{1,2} & 0 & \cdots & \cdots & \cdots & p_{1,L+1} & p_{1,L+2} & 0 & \cdots & \cdots & \cdots \\
\cdots & 0 & p_{i,i} & p_{i,i+1} & 0 & \cdots & \cdots & 0 & p_{i,L+i} & p_{i,L+i+1} & 0 & \cdots \\
\cdots & \cdots & \cdots & 0 & 0 & p_{L,L} & 0 & \cdots & \cdots & 0 & 0 & p_{L,2L} \\
p_{L+1,1} & p_{L+1,2} & 0 & \cdots & \cdots & \cdots & p_{L+1,L+1} & p_{L+1,L+2} & 0 & \cdots & \cdots & \cdots \\
\cdots & 0 & p_{L+i,i} & p_{L+i,i+1} & 0 & \cdots & \cdots & 0 & p_{L+i,L+i} & p_{L+i,L+i+1} & 0 & \cdots \\
\cdots & \cdots & \cdots & 0 & p_{2L-1,L-1} & p_{2L-1,L} & 0 & \cdots & \cdots & 0 & p_{2L-1,2L-1} & p_{2L-1,2L} \\
1 & 0 & \cdots & \cdots & \cdots & \cdots & \cdots & \cdots & \cdots & \cdots & \cdots & 0
\end{bmatrix}$$

being

$$
\begin{aligned}
p_{1,1} &= 1 - t\bar{c}^E \tfrac{\omega}{v} \sin\left(t\tfrac{\omega}{v}\right) - \omega^2 \mu_e \tfrac{t\varepsilon^S}{e^2} \cos\left(t\tfrac{\omega}{v}\right) \\
p_{1,2} &= \cos\left(2t\tfrac{\omega}{v}\right) - 2\cos\left(t\tfrac{\omega}{v}\right) + t\bar{c}^E \tfrac{\omega}{v} \sin\left(t\tfrac{\omega}{v}\right) \\
p_{h,h} &= \cos\left((h-1)t\tfrac{\omega}{v}\right) - t\bar{c}^E \tfrac{\omega}{v} \sin\left(ht\tfrac{\omega}{v}\right) - \omega^2 \mu_e \tfrac{t\varepsilon^S}{e^2} \cos\left(ht\tfrac{\omega}{v}\right) \\
p_{h,h+1} &= \cos\left((h+1)t\tfrac{\omega}{v}\right) - 2\cos\left(ht\tfrac{\omega}{v}\right) + t\bar{c}^E \tfrac{\omega}{v} \sin\left(ht\tfrac{\omega}{v}\right) \\
p_{L,L} &= \left(1 - \kappa\tfrac{t\varepsilon^S}{e^2}\right) \cos\left(Lt\tfrac{\omega}{v}\right) - \cos\left((L-1)t\tfrac{\omega}{v}\right) + \omega^2 \tfrac{t\varepsilon^S}{e^2}(\mu_e + \mu_l) \cos\left(Lt\tfrac{\omega}{v}\right) + t\bar{c}^E \tfrac{\omega}{v} \sin\left(Lt\tfrac{\omega}{v}\right) \\
p_{1,L+1} &= \cos\left(t\tfrac{\omega}{v}\right) + \omega^2 \mu_e \tfrac{t\varepsilon^S}{e^2} \sin\left(t\tfrac{\omega}{v}\right) \\
p_{1,L+2} &= \sin\left(2t\tfrac{\omega}{v}\right) - 2\sin\left(t\tfrac{\omega}{v}\right) - t\bar{c}^E \tfrac{\omega}{v} \cos\left(t\tfrac{\omega}{v}\right) \\
p_{h,L+h} &= \sin\left((h-1)t\tfrac{\omega}{v}\right) + \bar{c}^E t\tfrac{\omega}{v} \cos\left(ht\tfrac{\omega}{v}\right) - \omega^2 \mu_e \tfrac{t\varepsilon^S}{e^2} \sin\left(ht\tfrac{\omega}{v}\right) \\
p_{h,L+h+1} &= \sin\left((h+1)t\tfrac{\omega}{v}\right) - 2\sin\left(ht\tfrac{\omega}{v}\right) - t\bar{c}^E \tfrac{\omega}{v} \cos\left(ht\tfrac{\omega}{v}\right) \\
p_{L,2L} &= \left(1 - \kappa\tfrac{t\varepsilon^S}{e^2}\right) \sin\left(Lt\tfrac{\omega}{v}\right) - \sin\left((L-1)t\tfrac{\omega}{v}\right) + \omega^2 \tfrac{t\varepsilon^S}{e^2}(\mu_e + \mu_l) \sin\left(Lt\tfrac{\omega}{v}\right) - t\bar{c}^E \tfrac{\omega}{v} \cos\left(Lt\tfrac{\omega}{v}\right) \\
p_{L+1,1} &= -\cos\left(t\tfrac{\omega}{v}\right) \\
p_{L+1,2} &= \cos\left(t\tfrac{\omega}{v}\right) \\
p_{L+h,h} &= -\cos\left(ht\tfrac{\omega}{v}\right) \\
p_{L+h,h+1} &= \cos\left(ht\tfrac{\omega}{v}\right) \\
p_{2L-1,L-1} &= -\cos\left((L-1)t\tfrac{\omega}{v}\right) \\
p_{2L-1,L} &= \cos\left((L-1)t\tfrac{\omega}{v}\right) \\
p_{L+1,L+1} &= -\sin\left(t\tfrac{\omega}{v}\right) \\
p_{L+1,L+2} &= \sin\left(t\tfrac{\omega}{v}\right) \\
p_{L+h,L+h} &= -\sin\left(ht\tfrac{\omega}{v}\right) \\
p_{L+h,L+h+1} &= \sin\left(ht\tfrac{\omega}{v}\right) \\
p_{2L-1,2L-1} &= -\sin\left((L-1)t\tfrac{\omega}{v}\right) \\
p_{2L-1,2L} &= \sin\left((L-1)t\tfrac{\omega}{v}\right) \\
p_{2L,1} &= 0
\end{aligned}
\tag{3.20}
$$

The system of equations can be solved as

$$\boldsymbol{p} = P^{-1}\boldsymbol{g} \tag{3.21}$$

3.6 Physical quantities

The key to obtain an explicit expression of all the physical quantities is to calculate the values of B^k. That is easily achieved by

$$B^k(\tau) = \frac{1}{t}\left(V_p^k(\tau) - \bar{u}^k(kt,\tau) + \bar{u}^k((k-1)t,\tau)\right) \qquad k = 1,\dots,L \tag{3.22}$$

The time-independent part can be obtained from Eq. 3.16 as

$$\begin{aligned} B^k = \frac{1}{t}\Bigg(V_p - r_k\left(\cos\left(\frac{\omega}{v}kt\right) - \cos\left(\frac{\omega}{v}(k-1)t\right)\right) - \\ -q_k\left(\sin\left(\frac{\omega}{v}kt\right) - \sin\left(\frac{\omega}{v}(k-1)t\right)\right)\Bigg) \qquad k = 1,\dots,L \end{aligned} \tag{3.23}$$

3.6.1 Stress

The maximum stress occurs at the lower surface, where the actuator is fixed to the base. The stress can be calculated as

$$T_{\max} = \frac{e}{t}V_p + r_1\frac{e}{t}\left(1 - \cos\left(\frac{\omega}{v}t\right)\right) + q_1\frac{e}{t}\left(\bar{c}^E t\frac{\omega}{v} - \sin\left(\frac{\omega}{v}t\right)\right) \tag{3.24}$$

recalling Eq. 3.4.

3.6.2 Electric displacement, charge, and current

The same can be done for the electrical quantities; from Eq. 3.4 and 3.23

$$\begin{aligned} D^k = -\frac{\varepsilon^S}{t}\Bigg(V_p - r_k\left(\cos\left(\frac{\omega}{v}kt\right) - \cos\left(\frac{\omega}{v}(k-1)t\right)\right) - \\ -q_k\left(\sin\left(\frac{\omega}{v}kt\right) - \sin\left(\frac{\omega}{v}(k-1)t\right)\right)\Bigg) \qquad k = 1,\dots,L \end{aligned} \tag{3.25}$$

The amplitude of the charge and current can be easily calculated as

$$\begin{cases} Q^k = -D^k A \\ I^k = -\omega D^k A \end{cases} \tag{3.26}$$

3.7 Electric circuit

The electric driving circuit specifications can be included in the model as done in chapter one. Should an internal resistor be taken into account, the relative equations are as follows. The equations previously developed consider an ideal voltage source. As a consequence the voltage drop V_p^k is exactly the voltage drop across the two electrodes. When an internal resistor is considered such voltage drop is not the one produced by the voltage source. A procedure for calculating it can be nevertheless devised.

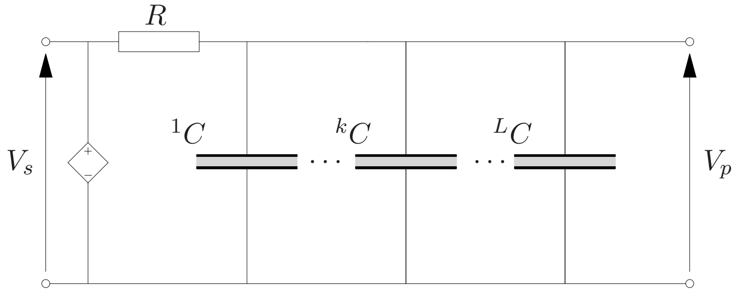

Figure 3.4: Driving circuit for a piezoelectric actuator

When a voltage V_s is applied, a current flows through each layer according to the charge accumulated on the piezoelectric layer and the layer deformation. Pertinent equations are those in Eq. 3.26. The electric circuit equation is

$$V_s = R\sum_{k=1}^{L} I^k + V_p \tag{3.27}$$

which can be expressed explicitly as

$$V_s = V_p\sin(\omega\tau) + RA\sum_{k=1}^{L}\frac{\varepsilon^S}{t}\left(V_p - r_k\left(\cos\left(\frac{\omega}{v}kt\right) - \cos\left(\frac{\omega}{v}(k-1)t\right)\right) - \right.$$
$$\left. -q_k\left(\sin\left(\frac{\omega}{v}kt\right) - \sin\left(\frac{\omega}{v}(k-1)t\right)\right)\right)\cos(\omega\tau) \tag{3.28}$$

As the equation Eq. 3.28 shows, the amplitude of the voltage V_s required to apply a voltage V_p to the actuator varies according to r_k, q_k. Supposing a unitary voltage across the piezoelectric actuator, the circuit equation Eq. 3.27 becomes

$$V_s = R\sum_{k=1}^{L} I^k_{V_p=1} + 1 \tag{3.29}$$

In such conditions, the charge accumulated on the electrodes in Eq. 3.26 is numerically equal to the actuator's capacitance, that is

$$C = L\frac{\varepsilon^S A}{t} - \frac{\varepsilon^S A}{t}\sum_{k=1}^{L} r_k^{V_p=1}\left(\cos\left(\frac{\omega}{v}kt\right) - \cos\left(\frac{\omega}{v}(k-1)t\right)\right) +$$
$$+ q_k^{V_p=1}\left(\sin\left(\frac{\omega}{v}kt\right) - \sin\left(\frac{\omega}{v}(k-1)t\right)\right) \tag{3.30}$$

where the superscript "$V_p = 1$" has been added to the coefficients r_k, q_k to underline that they must be calculated for a unitary voltage V_p. All this said and done, the system could be described as an RC electric circuit where the multilayer actuator is a capacitor whose capacitance is frequency-dependent, as already analysed in chapter one. For an RC electric circuit, the voltage across the capacitive element, in this case the piezoelectric actuator, is reduced according to Eq. 1.35.

The actual values of displacement, current, mechanical stress, etc. can be found simply multiplying the values found at $V_p = 1$ for the coefficient $V_s \cos\theta$, since the system of equations Eq. 3.21 is linear.

3.8 Parametric analysis

The multilayer analytical modelling (MLM) allows evaluating the influence of all the parameters employed on the system's dynamics, as the equations set Eq. 3.21 shows. The parameters whose influence is to be investigated are those related to the actuator's geometry. Material characteristics were not taken into account, as to underline the focus of the present work on the system design. The cross-sectional area does not have any influence on the dynamic behaviour of the actuator, granted that the load mass m is proportional to the actuator's active mass m_{MLA}, i.e. the mass of the piezoelectric material alone. The preload force is considered to be constant given the very small displacement of the actuator's free end, thus can be modelled as a constant force. For a constant force does not interfere with the dynamic behaviour, it is not taken into account in the present analysis. On the contrary the load mass and stiffness, the stack height, the electrode thickness will be varied in wide ranges.

As introduced in the previous sections, often piezoelectric multilayer actuators have been modelled as bulk piezoelectric continua (bulk modelling, BKM). It will be shown that MLM does provide a higher number of resonance frequencies in the same frequency range, besides the capabilities of a more detailed analysis.

3.8.1 Parameters estimation

The mathematical models presented require a number of parameters that are not readily available from the manufacturer's datasheet. Nevertheless, some simpe procedures were devised in order to find all the necessary data without carrying out dedicated measurements. The procedure to evaluate the material constants were already presented in chapter one.

The next step is to estimate the actuator's geometrical dimensions, namely the layer thickness and area, and the number of layers. The layer thickness t can be calculated once the height of the active part of the actuator is known. A simple comparison between the different overall heights and relative maximum displacements of actuators belonging to the same family allows deducing the displacement corresponding to a certain height of the active part. Supposing an height H and a displacement $u_{\max}$, from Eq. B.24

$$\frac{u_{\max}}{H} = -\frac{e_{33}}{c_{33}^E}\frac{LV_p}{Lt} \qquad \rightarrow \qquad t = -\frac{e_{33}}{c_{33}^E}\frac{H}{u_{\max}}V_p \tag{3.31}$$

where L is the number of layers. It is straightforward then to calculate L, given the active part height

$$L = \frac{H}{t} \tag{3.32}$$

The active part area A can be easily obtained from the capacitance value found in the datasheets. Often the capacitance is measured at a certain voltage and frequency, usually far enough from resonance condition. Therefore it is appropriate to consider this value comparable to the static capacitance (see Eq. 1.36). Furthermore, the voltage amplitude is small, so that deformation is limited; consequently

$$A = \frac{t}{L\varepsilon^S} \tag{3.33}$$

In case the electrode thickness is taken into account, Eq. 3.31 and 3.32 are modified as follows

$$\left\{ \begin{array}{l} \frac{u_{\max}}{Lt} = -\frac{e_{33}}{c_{33}^E}\frac{LV_p}{Lt} \\ H = (1+k_t)Lt \end{array} \right. \rightarrow \left\{ \begin{array}{l} L = -\frac{c_{33}^E}{e_{33}}\frac{u_{\max}}{V_p} \\ t = \frac{H}{(1+k_t)L} \end{array} \right. \tag{3.34}$$

where k_t is the ratio between electrode thickness and piezoelectric layer thickness. It goes without saying that this ratio in the present investigation is discretionary.

In order to evaluate properly the mass of the load that the active part is moving, some estimation on the mass of the actuator's mechanical interface must be made. Most multilayer actuators present the active part enclosed in a metallic case that serves both as a protective shell against humidity and pollution and as a practical mean to exert a constant compressive force on the active part. Indeed, to avoid dangerous tensile stresses on the piezoelectric material, an elastic element is interposed between the active part of the actuator and the case (see Fig. 3.5). The active part is rigidly

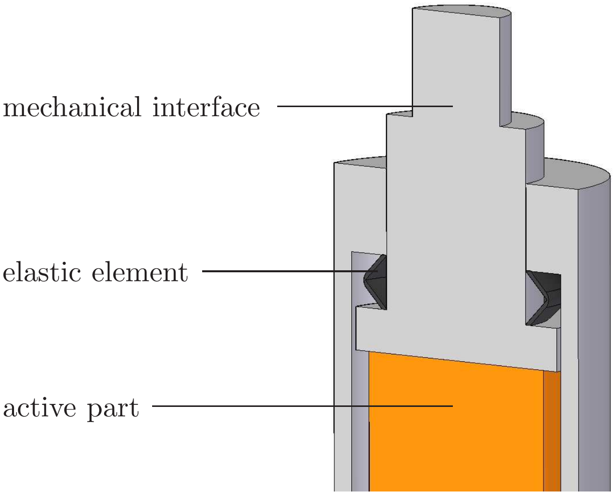

Figure 3.5: Multilayer actuator cross-sectional view. Please notice that this image is only qualitative.

connected to a sort of threaded rod that allows fixing a load to the actuator. The mass of this device must be known and it will be referred to as m_{tip}.

3.8.2 Influence of system's parameters

To evaluate the influence of the system's parameters to the dynamic behaviour, the characteristics of some commercially available actuators were considered (PI - P840/841 family [22]). The actuators from this family withstand loads up to 1000 N, are driven at a voltage between -20 V and 120 V, produce displacements from 15 μm to 90 μm, and have resonance frequencies ranging from 6 kHz to 18 kHz. The mass of the actuator's mechanical interface is estimated as

$$m_{\mathrm{tip}} = \frac{\pi(5\ \mathrm{mm})^2}{4} \cdot 15\ \mathrm{mm} \cdot 7.8 \cdot 10^{-6}\ \mathrm{kg/mm}^3 = 0.0023\ \mathrm{kg} \tag{3.35}$$

value that will be rounded up to 0.003 kg, comprehensive of part of the preload element. The mass of the active part of the actuator is 0.012 kg, that means the coefficient of normalized load mass coefficient k_m cannot be lower than 0.25.

The electrodes constitute, from the mechanical point of view, a set of passive elements that slow down the actuator's response. They cannot be treated as an external bulk load since their dynamics differs according to their position along the actuator. The presented multilayer model allows taking their exact dynamics into account. Figure 3.6 shows the influence of the electrode mass on the overall dynamics of a system driven by a piezoelectric actuator under the excitation of a sinusoidal voltage. The

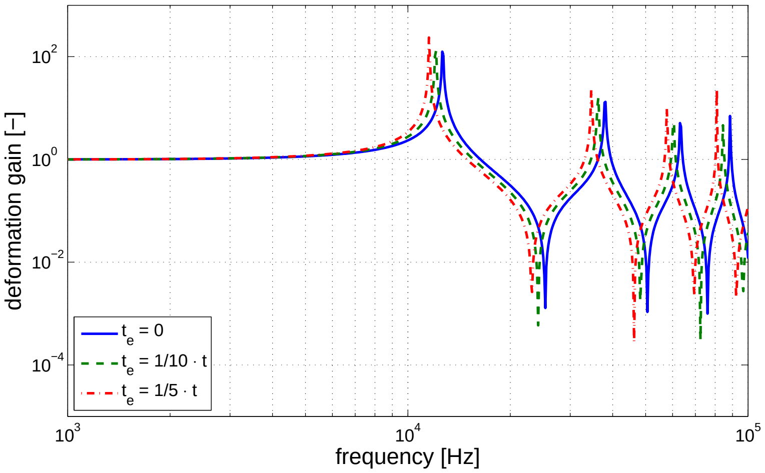

Figure 3.6: Frequency response as electrodes mass varies: the solid line shows the frequency response when the influence of electrode mass is disregarded. The dashed and dash-dotted ones are the result of the actuator's dynamics when the electrodes thickness is respectively one tenth and one fifth of the layer thickness. In these simulations the load stiffness k and the load mass m were set to zero.

length of the actuator's active part is 54 mm (the load mass is fixed at 3 g while the elastic stiffness of the external load are set to zero. Such mass is that of the mechanical interface to the outside and it does not vary for any actuator of the family). The electrode mass is chosen so that its thickness t_e can be compared to that of the active piezoelectric layer. The electrode mass does slow, although not very sensibly, the natural frequencies of the system, even for electrode thickness equal to one fifth of the piezoelectric layer.

The same system has been tested under various values of the load stiffness. In these simulations the electrode mass is discarded, and the load mass is still 3 g. Results are shown in Fig. 3.7. The three curves show the frequency response of the actuator as the spring stiffness k increases from zero to one tenth and to the same value of the actuator stiffness k_{MLA}. The actuator stiffness is calculated in static conditions at constant electric field. As the load stiffness increases, so does the first resonance frequency; but at the same time the static deformation decreases. As the figure shows, the influence of the external elastic load is nearly negligible when the spring stiffness is much lower than the actuator's.

The specification that differentiates one another the MLAs is the stack length H. This parameter is directly connected to the actuator's stroke and therefore is definitely

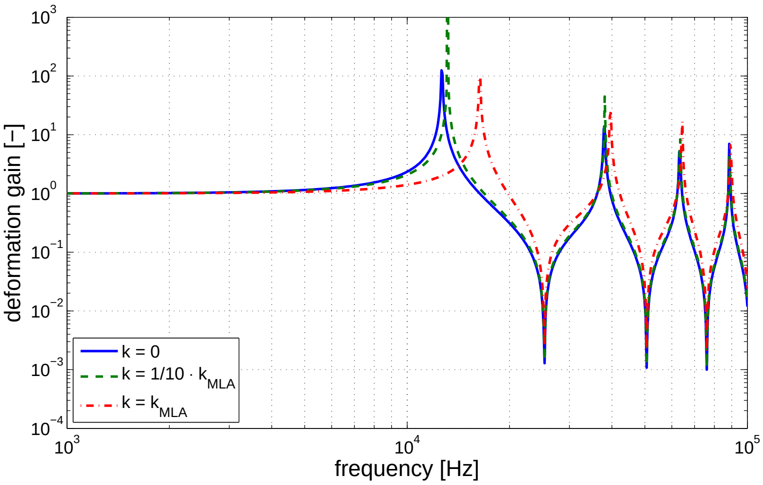

Figure 3.7: Frequency response as load stiffness varies: the solid line shows the frequency response of the unloaded actuator's dynamics when the stiffness constant k was set to zero. The dashed and dash-dotted ones are the result of the actuator when k is set to respectively 0.1 k_{MLA} and k_{MLA}, being k_{MLA} the axial stiffness of the piezoelectric actuator at constant electric field.

a key design variable.

The dynamic response of the actuator alone to a sinusoidal voltage excitation has been investigated for several values of the actuator length. The value of the load mass has been set to 3 g to take the mechanical interface mass into account, the electrode thickness to one tenth of the piezoelectric layer's one, and the load stiffness to zero. Figure 3.8 shows the frequency responses of the actuator for several values of its length. Since the length is tightly connected to the actuator's stroke, the y axis reports corresponding stroke values for a deformation of 0.08 %. Resonance and antiresonance frequencies can be identified in the figure by the colors: the red areas indicate the resonance peaks, while the deep blue ones the antiresonance peaks. As the actuator length increases all natural frequencies decrease following a hyperbolic-like trend. The influence of the inertial load (the mass of the mechanical interface) weakens as the actuator grows larger: such behaviour is easily predictable since the inertial load mass becomes a smaller fraction of the actuator's active part mass. For the smallest actuator of the family, the inertial load mass is of the same order of magnitude of that of the active part. Higher natural frequencies (found in the top-right part of Fig. 3.8) seem to be linearly dependent on the actuator length.

Focusing on the the first resonance frequency, the family of actuators was tested

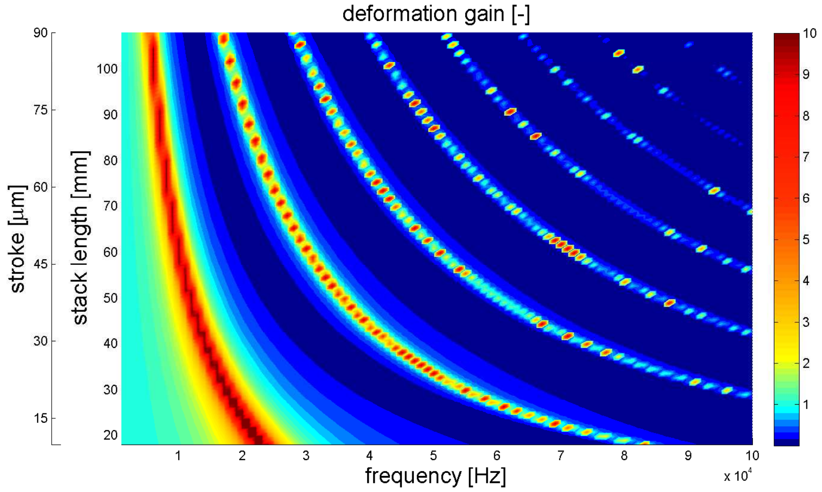

Figure 3.8: Frequency response to a sinusoidal voltage as the actuator length varies: the red areas are found in correspondence of the resonance peaks.

when a purely inertial load is considered[1]. The load mass is normalized to the mass of the actuator's active part, allowing a less biased comparison of the actuators' performances. The parameter k_m is the ratio of the load mass m to the mass of the active part m_{MLA}. Figures 3.9 and 3.10 show the results of these simulations. In Fig. 3.9 the value of the first resonance frequency is plotted versus the actuator length while the normalized load mass is varied. In Fig. 3.10 the values of the first resonance frequency are plotted versus the normalized load mass while the actuator length is a parameter.

The first resonance frequency is inversely proportional to the actuator length regardlessly of the load mass m (in the double logarithmic plot of Fig. 3.9 the resonance frequency is a linear function of the stack length). The resonance frequency is inversely proportional to the load mass ratio k_m too. In the double logarithmic plot of Fig. 3.10 a non-linear dependency is clearly visible. There is a transition between $k_m = 0.1$ and $k_m = 1$ where the slope of the curve changes. Outside this range the curves can be regarded as straight lines, although with different slopes. For k_m greater than 1, the first resonance frequency is conversely proportional to k_m, while for k_m smaller than 0.1 the influence of the mass load is negligible.

---

[1] The values of the stack length H are linearly spaced between 18 and 108 mm. The values of k_m are 0.01, 0.05, 0.1, 0.2, 0.5, 1, 2, 3, 4, 5, 10, 20, 30, 40, 50, 60, 70, 80, 90, 100. Neither linear nor logarithmic spacings were considered suitable since both do not provide enough values at either ends of the range. Figures 3.9, 3.10, and 3.16 are all obtained for these ranges.

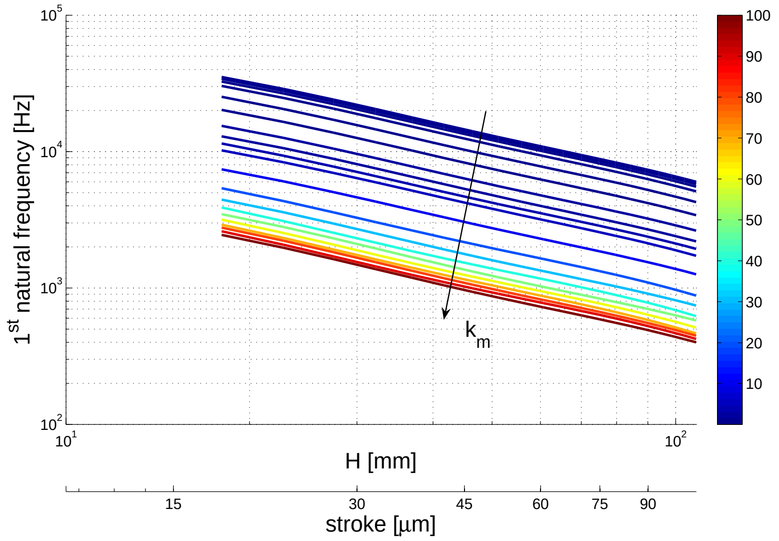

Figure 3.9: First natural frequency of the piezoelectric actuator versus the actuator length H; several curves are plotted for various values of the normalized inertial load mass k_m.

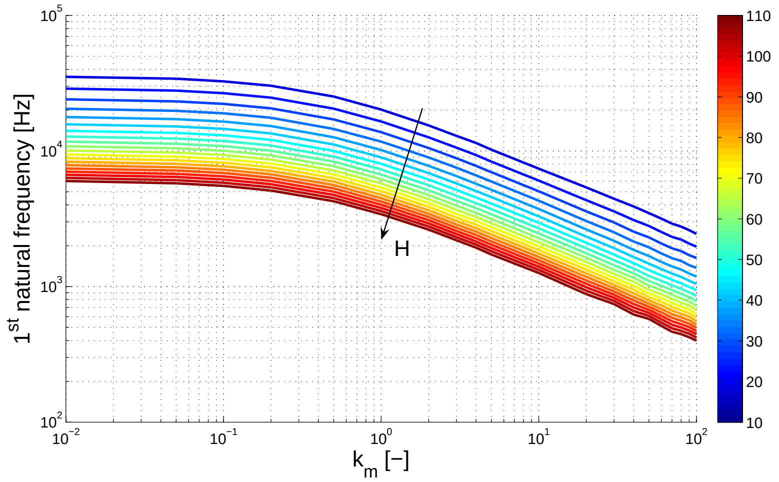

Figure 3.10: First natural frequency of the piezoelectric actuator versus the normalized inertial load mass k_m; several curves are plotted for various values of the actuator length H.

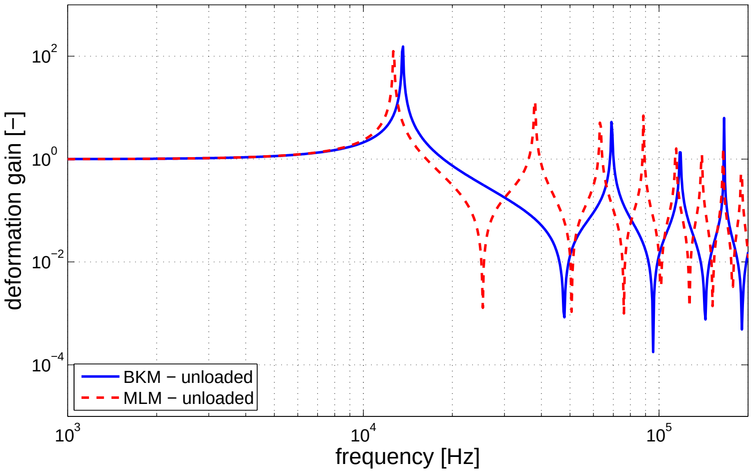

Figure 3.11: Frequency response of an unloaded multilayer actuator: the solid line shows the frequency response of the MLA modelled by BKM. The dashed line is the result of the MLM.

3.8.3 Comparison with bulk modelling

The behaviour of a sample piezoelectric MLA was analysed. Its characteristics are close to those of commercially available actuators. The sample MLA is constituted by 500 layers whose area and thickness are respectively 100 mm^2 and 0.1 mm. The piezoelectric material's constants were taken from a commercially available ceramics (PIC 151 from *PI ceramics* [22]) as shown in Tab. 1.1. A sinusoidal voltage of 100 V is applied; the applied voltage induces an electric field of 1 MV/m.

Figure 3.11 shows the frequency response for a MLA modelled both by BKM and by MLM. The equations employed for the analytical modelling of the piezoelectric continuum are those shown in [26]. The first natural frequency is calculated with the significant difference of 8 % (12.6 kHz versus 13.6 kHz). A remarkable difference is given though by the first antiresonance frequency (89 % difference, 25.4 kHz versus 47.9 kHz) and by higher order resonance frequencies. When an inertial load is considered, the two models provide more similar results for the first resonance frequency (0.7 % difference, 6918 Hz versus 6966 Hz). Nevertheless, higher order frequencies differ more consistently (see Fig. 3.12). At higher frequencies the MLM modelling allows funding a larger number of resonance frequencies in the investigated range than BKM modelling , as both Fig. 3.11 and Fig. 3.12 shows.

A more complete investigation of the behaviour of the two mathematical models

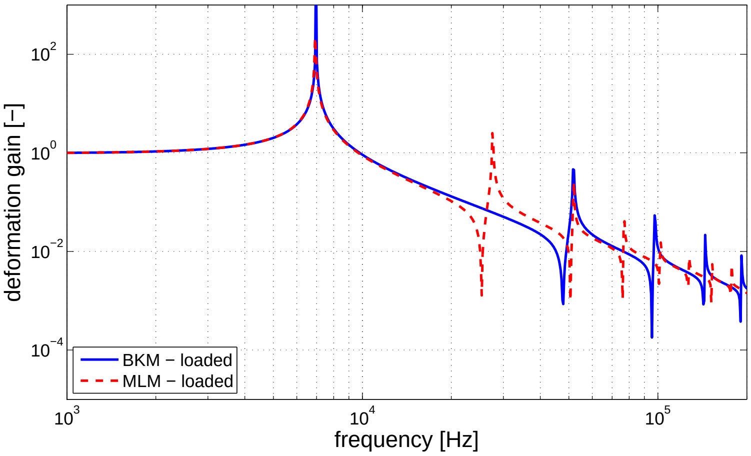

Figure 3.12: Frequency response of a loaded multilayer actuator: the solid line shows the frequency response of the MLA modelled by BKM. The dashed line is the result of the MLM. The actuator is loaded by an inertial load whose mass equals that of the actuator.

can be done by evaluating the resonance frequencies as the number of layers L used for modelling the piezoelectric MLA and k_m vary. For $L = 500$ the behaviour is that of the multilayer modelling and for $L = 1$ the behaviour coincides with that of the monolithic modelling. It must be noted that the electric field is kept constant at 1 MV/m, therefore the driving voltage is increased accordingly. The purpose of this workaround is to obtain equal static deformations. Nonetheless, driving voltage amplitudes do not influence resonance frequencies.

Figure 3.13 helps highlighting the influence of the piezoelectric layer thickness and of the inertial load mass on the actuator's dynamics. The figure shows the value of the first natural frequency: it is slightly depended on the layer thickness at low inertial loads, while it is nearly independent on L at higher inertial loads (as Fig. 3.12 already showed). However, the value of the first resonance frequency decreases significantly as the inertial load mass increases.

Figures 3.14 and 3.15 show respectively the second and third resonance frequencies. In these cases the frequencies are very much dependent on both L and k_m. While the latter was easily predictable, the former indicates a significant difference between the mathematical models.

It is worth noticing that similar values of the resonance frequencies are found for a number of layers that is considerably smaller than the actual one. It can be affirmed

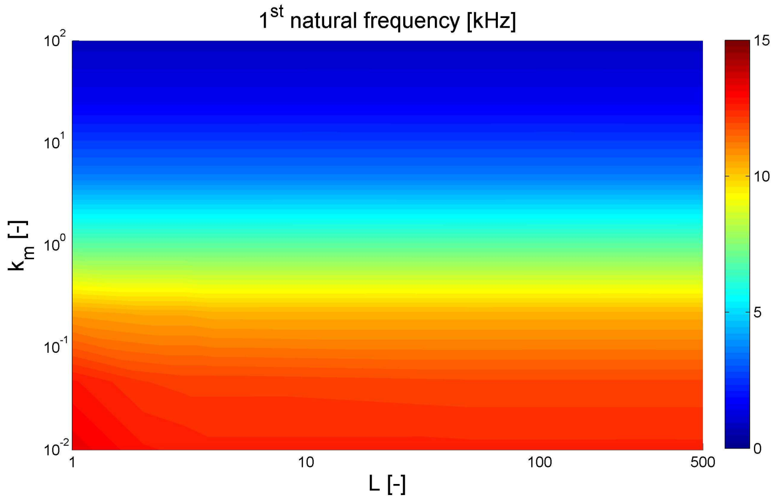

Figure 3.13: First natural frequency of the piezoelectric actuator as the number of layers L and the normalized inertial load mass k_m vary.

that for 100 layers (that is 1/5 of the actual value) there is no difference in the values of the first, second, and third resonance frequencies, regardless of the normalized load mass k_m. For $L = 10$ (1/50 of the actual value) some differences in the values of the first three resonance frequencies are found at low k_m (below $k_m = 0.1$). Therefore the MLM modelling is claimed to provide accurate results of the investigated resonance frequencies even if a reduced number of layers is considered. This methodology allows reducing the size of the equations set Eq. 3.21 and therefore reduces the computational effort.

The simulations presented does not consider any dissipative phenomena, therefore, in correspondence of resonance frequencies, the displacements amplitude goes to infinity. Such behaviour is obviously not encountered in the real-life situations where friction and other dissipative phenomena reduce the amplitude of the displacements. Nevertheless, even in this theoretical speculation, some limitations can be taken into account. As an example, a limit to the stress level has to be introduced, otherwise the actuator breaks down because of mechanical failure. Indeed as the frequency increases there is significant increase in magnitude of the inertial forces (due to both larger displacement and accelerations) and thus of the stress level. The stress, calculated analytically, was monitored at the fixed end of the actuator, where it is largest. Figure 3.16 shows the frequency reduction with respect to the first natural frequency (Fig. 3.9 can be taken as reference). The largest frequency reductions occur for those configurations that reach the highest resonance frequencies: these are made by small actuators with low inertial

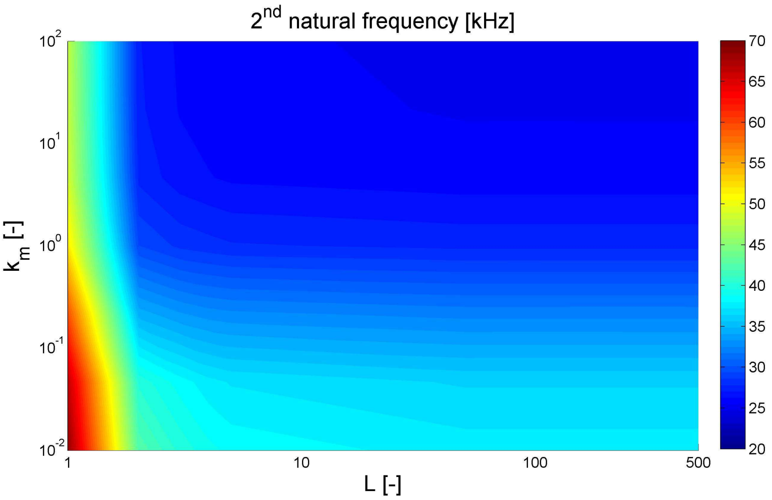

Figure 3.14: Second natural frequency of the piezoelectric actuator as the number of layers L and the normalized inertial load mass k_m vary.

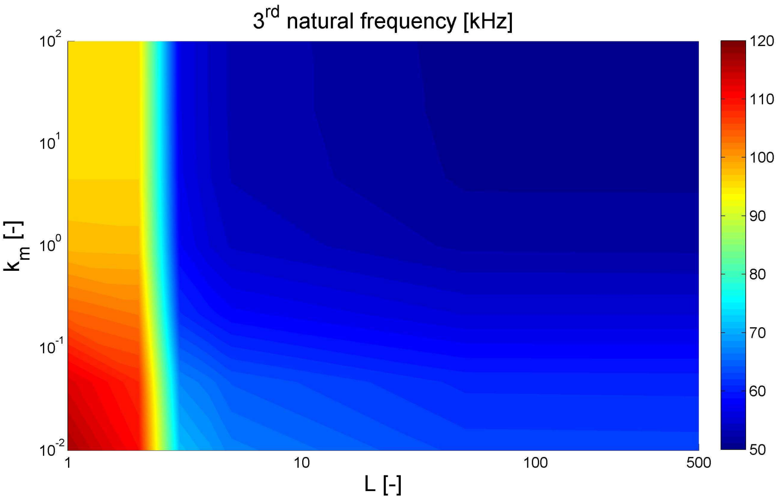

Figure 3.15: Third natural frequency of the piezoelectric actuator as the number of layers L and the normalized inertial load mass k_m vary.

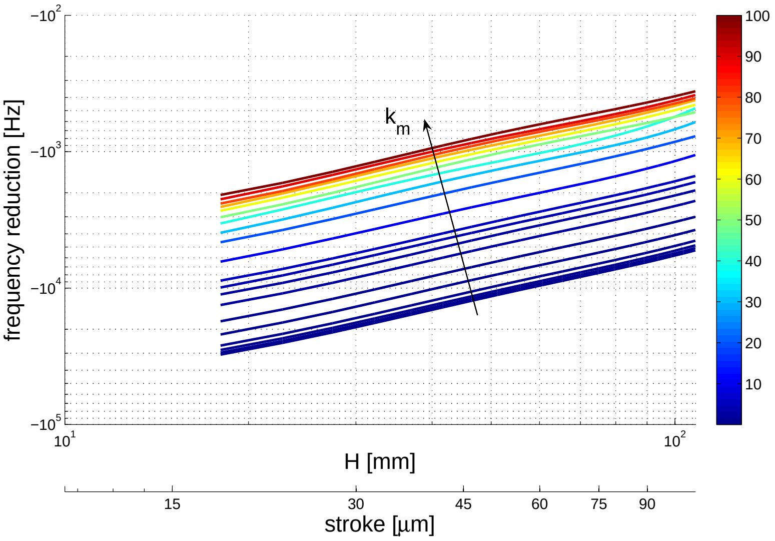

Figure 3.16: Reduction of frequency range of use of the piezoelectric actuator due to stress limitations. The curves shows the frequency reduction with respect to the 1st natural frequency versus the actuator length H; several curves are plotted for various values of the normalized inertial load mass k_m.

load. It must be noted that this results are purely indicative (maximum stress was set to 30 MPa) and are obtained from a non-dissipative system.

Chapter 4

Finite difference modelling of piezoelectric MLAs

The motivation for the formulation of a finite difference model of a piezoelectric multilayer actuator lies in the same limitations found for the analytical model of a piezoelectric plate. The hypothesis on which the two analytical models presented are based are exactly the same; therefore the limitations to the use of the models are identical. The same can be said for the advantages that a finite difference model can bring in. Furthermore, while the dynamics of a piezoelectric plate can be interesting for a relatively limited number of applications, the dynamics of systems driven by piezoelectric actuators, especially in transient conditions, can be very useful for the choice of actuator and the design of the power supply.

Figure 4.1 shows how a piezoelectric MLA can be modelled by finite elements. Each layer is split in M elements, whose displacement is ${}^{k}u_i^j$. Although an electrode is

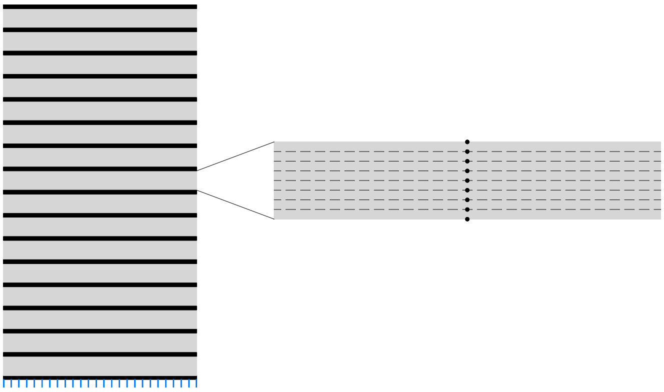

Figure 4.1: Discretization in finite elements of a piezoelectric multilayer actuator

interposed between piezoelectric layers, from the kinematical point of view the faces of neighbouring layers are considered to have the same displacement. This assumption is equivalent to neglecting the electrodes' elasticity.

4.1 Multilayer dynamics

The dynamics of a stack of piezoelectric plates can be studied by finite difference modelling considering varying boundary conditions on each plate. Equations obtained in the previous sections are valid for any boundary conditions, including rigid body motion of the plate.

Considering a piezoelectric actuator made by L layers, having the same thickness t and the same surface area A, the dynamics of each "internal" layer can be described by the following set of equations and boundary conditions

$$\begin{cases} {}^{k}u_{,xx} = \frac{1}{v^2}\,{}^{k}u_{,\tau\tau} \\ {}^{k}T\left(-\frac{t}{2}\right) = \mu_e\ {}^{k}u_{,\tau\tau}\left(-\frac{t}{2}\right) + {}^{k-1}T\left(\frac{t}{2}\right) \\ {}^{k}u\left(-\frac{t}{2}\right) = {}^{k-1}u\left(\frac{t}{2}\right) \\ {}^{k}\varphi\left(\frac{t}{2}\right) - {}^{k}\varphi\left(-\frac{t}{2}\right) = {}^{k}V_p \end{cases} \qquad k = 2, \ldots, L-1 \tag{4.1}$$

where the first superscript refers to the corresponding layer. The system of equations can be written in terms of finite difference equations as

$$\begin{cases} {}^{k}u_i^{j+1} = {}^{k}u_{i+1}^{j} + {}^{k}u_{i-1}^{j} - {}^{k}u_i^{j-1} \qquad i = 2, \ldots, M-1 \\ {}^{k-1}u_M^{j+1} = {}^{k}u_1^{j+1} \\ {}^{k}B_1^{j} = \frac{{}^{k}V_p^{j}}{t} - \frac{e}{\varepsilon^S t}\left({}^{k}u_M^{j} - {}^{k}u_1^{j}\right) \\ {}^{k}u_1^{j+1} = -{}^{k}u_1^{j-1} + \left(1 + \frac{\delta}{\chi^2}\frac{\mu_e}{\bar{c}^E}\right)^{-1}\left({}^{k}u_2^{j} + {}^{k-1}u_{M-1}^{j} - {}^{k-1}u_M^{j-1} + \right. \qquad k = 2, \ldots, L-1 \\ \qquad \left. + \frac{\delta}{t}\frac{e^2}{\bar{c}^E\varepsilon^S}\left(2\ {}^{k}u_1^{j} - {}^{k-1}u_1^{j} - {}^{k}u_M^{j}\right) + 2\frac{\delta}{\chi^2}\frac{\mu_e}{\bar{c}^E}\ {}^{k}u_1^{j}\right) \\ {}^{k-1}u_{M+1}^{j} = {}^{k}u_1^{j+1} - {}^{k-1}u_{M-1}^{j} + {}^{k-1}u_M^{j-1} \\ {}^{k}u_0^{j} = {}^{k}u_1^{j+1} - {}^{k}u_2^{j} + {}^{k}u_1^{j-1} \end{cases} \tag{4.2}$$

An internal layer is one upon which no external forces can be applied and only kinematic constraints to neighbouring layers are present. The equations set Eq. 4.1 is to be completed by the equations governing the dynamics of the "external" layers, which vary according to peculiar boundary conditions.

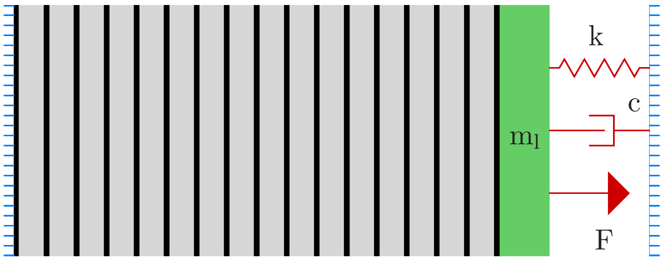

Figure 4.2: Model of a constrained multilayer actuator; the figure shows the loading conditions, featuring stiffness, damping, and inertia. Furthermore a time-dependent force can be applied.

4.2 Constrained actuator

Since the unconstrained actuator can be studied as composed by two constrained actuators oh half height, the equations will be derived only for a constrained one.

Should the layer 1 be constrained to a fixed position and the layer L loaded by a load with inertia m_l, stiffness k and a known force $F(\tau)$ (as shown in Fig. 4.2), the additional equations are

$$\begin{cases} {}^{1}u_{,xx} = \frac{1}{v^2}\,{}^{1}u_{,\tau\tau} \\ {}^{1}\varphi\left(\frac{t}{2}\right) - {}^{1}\varphi\left(-\frac{t}{2}\right) = {}^{1}V_p \\ {}^{1}u\left(-\frac{t}{2}\right) = 0 \\ {}^{L}u_{,xx} = \frac{1}{v^2}\,{}^{L}u_{,\tau\tau} \\ {}^{L}\varphi\left(\frac{t}{2}\right) - {}^{L}\varphi\left(-\frac{t}{2}\right) = {}^{L}V_p \\ {}^{L}u\left(-\frac{t}{2}\right) = {}^{L-1}u\left(\frac{t}{2}\right) \\ -(m_l + m_e)\,{}^{L}u_{,\tau\tau}\left(\frac{t}{2}\right) - c\,{}^{L}u_{,\tau}\left(\frac{t}{2}\right) - k\,{}^{L}u\left(\frac{t}{2}\right) + \\ \qquad +F - {}^{L}T\left(\frac{t}{2}\right)A = 0 \\ {}^{L}T\left(-\frac{t}{2}\right) = \mu_e\,{}^{L}u_{,\tau\tau}\left(-\frac{t}{2}\right) + {}^{L-1}T\left(\frac{t}{2}\right) \end{cases} \tag{4.3}$$

Finite difference method can be employed for finding the solution to this set of equations, yielding

$$\begin{cases} {}^1u_i^{j+1} = {}^1u_{i+1}^j + {}^1u_{i-1}^j - {}^1u_i^{j-1} \qquad i = 1, \dots, M \\ {}^1B_1^j = \frac{{}^1V_p^j}{t} - \frac{e}{\varepsilon^S t}({}^1u_M^j - {}^1u_1^j) \\ {}^1u_1^j = 0 \\ {}^Lu_i^{j+1} = {}^Lu_{i+1}^j + {}^Lu_{i-1}^j - {}^Lu_i^{j-1} \qquad i = 1, \dots, M \\ {}^LB_1^j = \frac{{}^LV_p^j}{t} - \frac{e}{\varepsilon^S t}({}^Lu_M^j - {}^Lu_1^j) \\ {}^Lu_1^j = {}^{L-1}u_M^j \\ -\mu\frac{{}^Lu_M^{j+1} - 2\ {}^Lu_M^j + {}^Lu_M^{j-1}}{\chi^2} - \gamma\frac{{}^Lu_M^{j+1} - {}^Lu_M^{j-1}}{2\chi} - \kappa\ {}^Lu_M^j + f^j - \\ \qquad -\bar{c}^E\frac{{}^Lu_{M+1}^j - {}^Lu_{M-1}^j}{2\delta} - \frac{e}{t}\ V_p^j + \frac{e^2}{\varepsilon^S t}\left({}^Lu_M^j - {}^Lu_1^j\right) = 0 \\ \frac{\bar{c}^E}{2\delta}\left({}^Lu_2^j - {}^Lu_0^j\right) - \frac{e^2}{\varepsilon^S t}({}^Lu_M^j - {}^Lu_1^j) + \frac{e}{t}\ {}^LV_p^j = \frac{\mu_e}{\chi^2}\left({}^Lu_1^{j+1} - 2\ {}^Lu_1^j + {}^Lu_1^{j-1}\right) + \\ \qquad + \frac{\bar{c}^E}{2\delta}\left({}^{L-1}u_{M+1}^j - {}^{L-1}u_{M-1}^j\right) - \frac{e^2}{\varepsilon^S t}({}^{L-1}u_M^j - {}^{L-1}u_1^j) + \frac{e}{t}\ {}^{L-1}V_p^j \end{cases} \tag{4.4}$$

where $\mu_e = \frac{m_e}{A}$, $\mu = \frac{m_l + m_e}{A}$, $\gamma = \frac{c}{A}$, $\kappa = \frac{k}{A}$ and $f = \frac{F}{A}$ are defined per unit area. Unknowns include ghost points at the time τ^j and the position at time τ^{j+1}. Unknowns can be isolated

$$\begin{cases} {}^1u_i^{j+1} = {}^1u_{i+1}^j + {}^1u_{i-1}^j - {}^1u_i^{j-1} \qquad i = 2, \dots, M-1 \\ {}^1u_0^j = {}^1u_2^j \\ {}^1B_1^j = \frac{{}^1V_p^j}{t} - \frac{e}{\varepsilon^S t}({}^1u_M^j - {}^1u_1^j) \\ {}^1u_1^j = 0 \\ {}^Lu_i^{j+1} = {}^Lu_{i+1}^j + {}^Lu_{i-1}^j - {}^Lu_i^{j-1} \qquad i = 2, \dots, M-1 \\ {}^Lu_1^{j+1} = {}^Lu_2^j + {}^Lu_0^j - {}^Lu_1^{j-1} \\ {}^Lu_M^{j+1} = {}^Lu_{M+1}^j + {}^Lu_{M-1}^j - {}^Lu_M^{j-1} \\ {}^LB_1^j = \frac{{}^LV_p^j}{t} - \frac{e}{\varepsilon^S t}({}^Lu_M^j - {}^Lu_1^j) \\ {}^Lu_1^j = {}^{L-1}u_M^j \\ {}^Lu_M^{j+1} = \left(\frac{\mu}{\chi^2} + \frac{\gamma}{2\chi} + \frac{\bar{c}^E}{2\delta}\right)^{-1}\left(\left(2\frac{\mu}{\chi^2} - \kappa + \frac{e^2}{\varepsilon^S t}\right)\ {}^Lu_M^j - \left(\frac{\mu}{\chi^2} - \frac{\gamma}{2\chi} + \frac{\bar{c}^E}{2\delta}\right){}^Lu_M^{j-1} - \right. \\ \qquad \left. + 2\frac{\bar{c}^E}{2\delta}\ {}^Lu_{M-1}^j - \frac{e^2}{\varepsilon^S t}{}^Lu_1^j + f^j - \frac{e}{t}\ V_p^j\right) \\ {}^Lu_1^{j+1} = -{}^Lu_1^{j-1} + \left(1 + \frac{\delta}{\chi^2}\frac{\mu_e}{\bar{c}^E}\right)^{-1}\left({}^Lu_2^j + {}^{L-1}u_{M-1}^j - {}^{L-1}u_M^{j-1} + \right. \\ \qquad \left. + \frac{\delta}{t}\frac{e^2}{\bar{c}^E\varepsilon^S}\left(2\ {}^Lu_1^j - {}^{L-1}u_1^j - {}^Lu_M^j\right) + 2\frac{\delta}{\chi^2}\frac{\mu_e}{\bar{c}^E}\ {}^Lu_1^j\right) \end{cases} \tag{4.5}$$

4.2.1 Electric circuit for multilayer actuator

The electric circuit for the multilayer actuator is the one shown in Fig. 3.4. The electrodes are connected in parallel to the same voltage source; this wiring method justifies the simplification introduced in the dynamics equation of the piezoelectric stack, the one that consider the voltage across every piezoelectric layers equal at all times. Circuit equations remain roughly the same with respect to the finite difference formulation already presented in chapter three, albeit the resultant current must be calculated summing up all the contributions. The circuit equation is

$$V_s^j = R\sum_{k=1}^{L} {}^kI^j + V_p^j \tag{4.6}$$

where ${}^kI$ is the current flowing to each piezoelectric layer k. In Eq 4.6 no distinction in voltage has been made between layers since they are all connected in parallel. The explicit expression of the overall current I is

$$I = \sum_{k=1}^{L} \varepsilon^S \frac{A}{2\chi t}\left(V_p^{j+1} - V_p^{j-1}\right) - e\frac{A}{2\chi t}\left({}^ku_M^{j+1} - {}^ku_M^{j-1} - {}^ku_1^{j+1} + {}^ku_1^{j-1}\right) \tag{4.7}$$

$$I = \frac{A}{2\chi t}\left(\varepsilon^S L\left(V_p^{j+1} - V_p^{j-1}\right) - e\left({}^Lu_M^{j+1} - {}^Lu_M^{j-1}\right)\right) \tag{4.8}$$

This expression can be substituted into Eq 4.6 allowing the calculation of the voltage across the piezoelectric actuator at the time step τ^{j+1}:

$$V_p^{j+1} = V_p^{j-1} + \frac{2\chi t}{L\varepsilon^S RA}\left(V_s^j - V_p^j\right) + \frac{e}{\varepsilon^S L}\left({}^Lu_M^{j+1} - {}^Lu_M^{j-1}\right) \tag{4.9}$$

4.3 Transient dynamics of a piezoelectric MLA

The transient dynamic response of a system driven by piezoelectric MLA is investigated for an actuator driving an inertial load. Although very simple, such system allows drawing some general conclusions regarding the influence of loads on the system dynamics. Analysing more complex situations would yield results hardly applicable to other contexts.

The transient behaviour of the system will be tested when subject to an input step voltage. The load mass and the circuit impedance will be varied for estimating their influence on the response speed. The parameters for the MLA are chosen to match a commercially available one (Physik Instrumente P842.10). This actuator is capable of strokes up to 15 μm when driven at 100 V and forces ranging from 300 N (traction) and 800 N (compression). Its capacitance is 1.5 μF and its unloaded resonance frequency is 18 kHz. All these values are subject to a ±20 % variability [22]. The

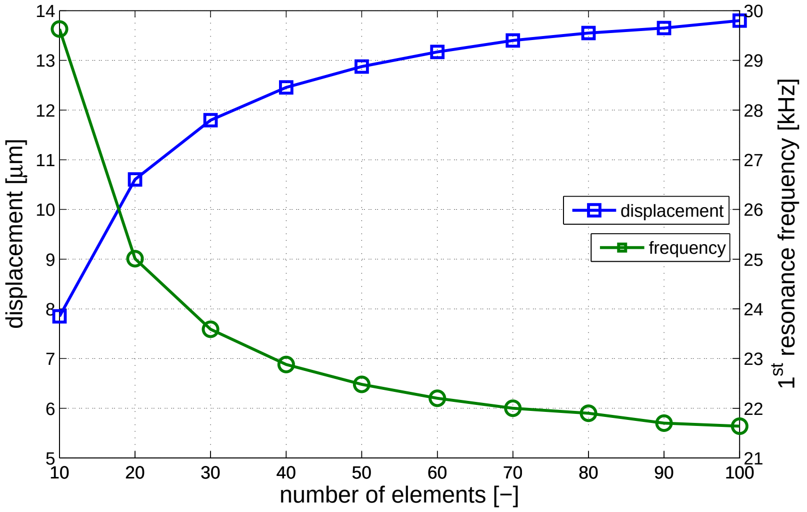

Figure 4.3: Convergence of MLA dynamics: first resonance frequency and amplitude of displacement

piezoelectric material the actuator is made of is a commercially available ceramic (PIC 151) whose characteristics are shown in Tab. 1.1. By making use of the equations of linear piezoelectricity all of the parameters of the MLA model presented could be calculated from the manufacturer's specifications, with the sole exception of the electrode thickness, which was estimated to be one tenth of the piezoelectric layer thickness. The resulting actuator's parameters are 254 layers, each 64.4 μm thick, whose surface area is 15.71 mm^2.

As for the piezoelectric plate, the MLA finite difference model is subject to numerical approximations, due to the discretization process. Figure 4.3 shows the dependency of maximum displacement and first resonance frequency on the number of elements employed for modelling a single layer. The procedure followed to obtain the lines of Fig. 4.3 is the same explained in chapter two. Instead of the strain, the displacement is represented, being more directly comparable with the actuator's datasheet values. It must be noticed that the displacement reported in figure is calculated as half the maximum displacement resulting from a step voltage input. As previously pointed out, this computed displacement should be equal to the static displacement, thus comparable to the values given by the manufacturer.

According to the convergence conditions previoulsy stated, each layer is subdivided into 50 elements, each 1.29 μm thick. As introduced in chapter two, the spatial and time discretization are linearly dependent, thus the time step must be set to 2.7 $\cdot 10^{-10}$ s.

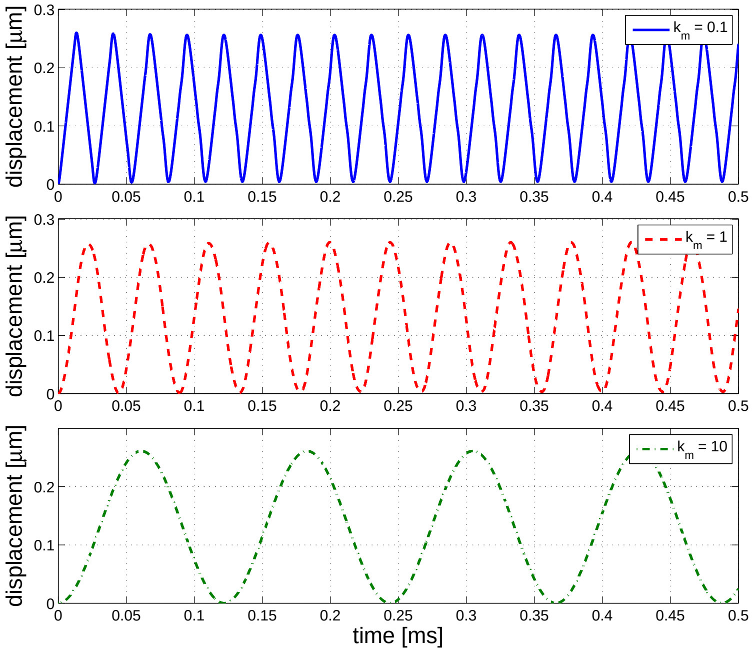

Figure 4.4: Response to a step voltage as load mass varies. The normalized load mass coefficient k_m in the three cases is 0.1, 1, and 10. The circuit resistance R is set to zero.

The values of the load mass are chosen so that they can be easily compared to the mass of the active part of the multilayer actuator. For this purpose the coefficient of normalized load mass k_m was introduced in chapter one. It is calculated as the ratio betweeen the load mass and the mass of the MLA active part. The load mass will be set to three values representative of three different conditions: small ($k_m = 0.1$), intermediate ($k_m = 1$), and large inertial loading ($k_m = 10$). Figure 4.4 shows the position of the free end of the actuator in response to a step voltage of amplitude 1 V. In this simulation the electric circuit impedance is set to zero, as to underline the effect of the load inertia on the system response. Being undamped, the system oscillates about the position of static equilibrium when driven at constant voltage. The amplitude of the oscillation is therefore equal to twice the static deformation. Since this value does not depend on the load mass (gravity is disregarded), the amplitude of the oscillations for the different loading conditions is the same. It must be noted that the period of oscillation is inversely proportional to the first resonance frequency of the system. As the load mass increases the shape of the displacement curve becomes smoother and the zones where the motion inversion occurs present a larger radius. Indeed, when the load mass is ten times the actuator active part's mass, the displacement curve looks

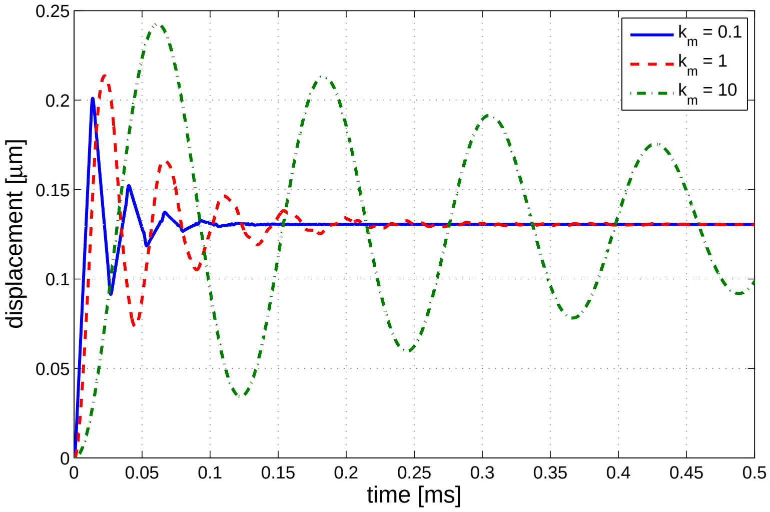

Figure 4.5: Displacement response to a step voltage as load mass varies. The circuit resistance R is set to 1 Ω.

very much like a sine. This behaviour may indicate similarities with a one degree of freedom spring-mass system. For smaller load masses the resulting motion is not so easily described and may suggest the superposition of several modes of vibration of the system.

A dissipative effect is introduced when the electric circuit impedance is considered, for example setting the value of R to 1 Ω. Figure 4.5 shows the displacement induced by a 1 V step voltage. The response is calculated for three different values of k_m: 0.1, 1, and 10; the smaller the load mass is, the quicker is the settling time. Furthermore it can be seen from Fig. 4.5 that the amplitude of the oscillations are proportional to the load mass. From the mechanical point of view this result can be easily forseen: the load mass lowers the resonance frequencies of the system and thus settling is expected to take more time. From the electrical point of view, one may anticipate a quite different behavior, independent of the load mass, on the ground that the electric circuit time constant is given by the product of the impedance and the MLA's capacitance. This reasoning fails because it considers the MLA's capacitance as a constant: in fact it depends on the actual deformation of the actuator. The rise time of the actuator, that is the time it takes to the actuator to settle in a static equilibrium position at a given driving voltage, could be estimated, in a purely electrical perspective, as five times the electric circuit time constant, yielding roughly 0.01 ms. From Fig. 4.5 it is clear that this calculation does not produce matching results.

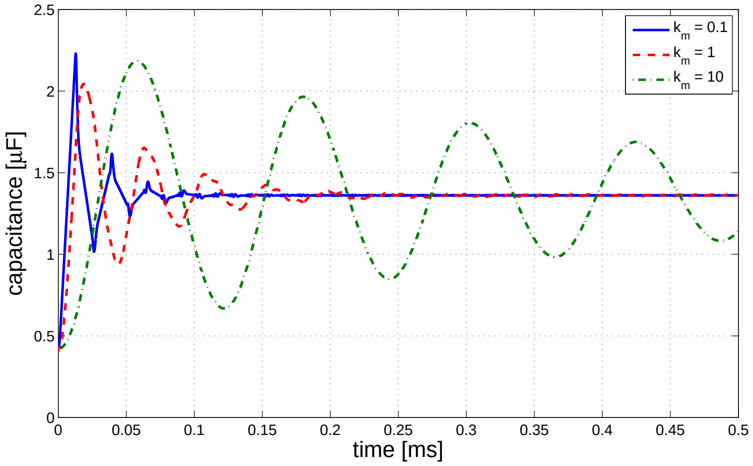

Figure 4.6: Capacitance response to an input step voltage as load mass varies. $V_s = 1$ V, $R = 1\ \Omega$

The implemented model allows calculating the actuator capacitance at each time step. The same simulations that brought the results shown in Fig. 4.5, gave also the values of the actuator's capacitance reported in Fig. 4.6. The variations of capacitance are very much connected to the displacement of the free end of the actuator, as the curves of Fig. 4.5 and Fig. 4.6 look very similar. At the beginning of the simulation the actuator undergoes large displacements and deformations that result in large fluctuations of the capacitance about its nominal value. When the transient phenomena have passed, the capacitance value is settled at 1.37 μF, that is close to the value measured by the manufacturer at 1 kHz, which is 1.5 μF [22]. Even in the "worst" case (that corresponds to the largest value of capacitance read in Fig. 4.6), the electric circuit time constant is not larger than 0.002 ms. The rise time of the actuator could be estimated as five time this time constant, yielding 0.01 ms. From Fig. 4.6 it is clear that this calculation does not produce matching results.

In Fig. 4.5 the static displacement is reached when the system has settled. Since linear relationships between electric field and deformation hold (see Eq. 1.1), the static displacement for 50 elements of Fig. 4.4 can be compared to 100 times the values read in the aforementioned figures: the values match.

Figure 4.7 shows the current requirement obtained in the same simulations of Fig. 4.5. The figure is split in two: in the upper part the whole time history is shown while in the lower part only the first 0.05 ms are shown in order to highlight the very first values of the current. The first value of the current is very large (0.5 A) for all the

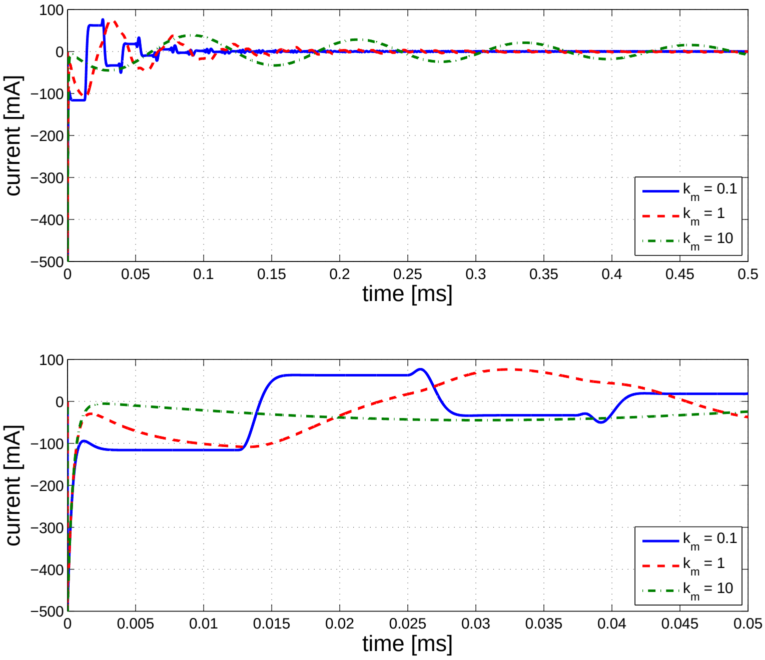

Figure 4.7: Current response to a step voltage as load mass varies. The circuit resistance R is set to 1 Ω.

three load masses and it may be due to the singularity encountered when the voltage goes from 0 V to 1 V. Nevertheless, the current rapidly decreases its absolute value following the same curve in the three cases until it takes different paths according to the inertial loading. For intermediate and large values of k_m the current curve is as smooth as the displacement and the capacitance curves. For small values of k_m the current changes abruptly, varying from constant values to upwards and downwards peaks. This behaviour is considered to reflect that of the displacement, where linear variations are alternated by sharp inversions. In the linear sections the capacitance varies too in a linear fashion, therefore the current is expected to be constant as in this case it can be regarded as proportional to the derivative of the capacitance.

Chapter 5

Test bench design

The results presented until now are very promising since they provide many pieces of information regarding the dynamic behaviour of a mechanical system driven by a piezoelectric actuator, either bulk or multilayer. To be of any practical use, the model presented must adhere to a certain degree to real dynamic behaviour. Here lies the motivation for the design of a test bench which allows to verify the models presented.

The test bench consists of a piezoelectric multilayer actuator rigidly connected to an inertial load whose mass can be varied in order to analyse its influence on the system's dynamics. The load displacement is monitored by a laser displacement sensor and a miniature accelerometer. The piezoelectric actuator is driven by a voltage signal that is amplified by dedicated circuitry. This electronic part allows also the measurement of the supplied current.

5.1 Test bench model

The test bench dynamics can be easily analysed with the mathematical models implemented in the previous chapters. This analysis will provide valuable indications for the choice of suitable sensors and the electronic components of the amplifying circuit. The amplifier's electric scheme can be reduced to an ideal controllable voltage source and a resistor (the one across which current is measured). The overall scheme of the test bench can be found in Fig. 5.1.

For convenience, the analytical model of a thin plate can be employed for investigating the dynamics of the test bench. The plate thickness will be equal to the height of the active part of the actuator, and the voltage will be multiplied by the number of layers.

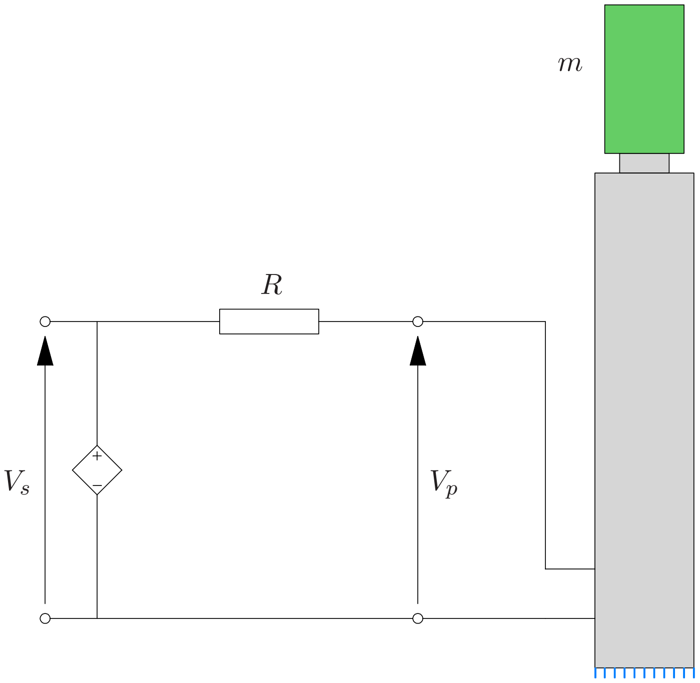

Figure 5.1: Test bench model

The actuator under test is a Physik Instrumente P842.60 whose characteristics are reported in Tab. 5.1; the material which it is made of is a modified lead-zirconate titanate (PIC151), as declared by the manufacturer. Its characteristics are reported in Tab. 1.1.

This data can be introduced into the Eq. 3.31, 3.32, and 3.33 yielding

$$\begin{cases} t = 64.4\ \mu\text{m} \\ L = 1525 \\ A = 15.69\ \text{mm}^2 \end{cases}$$

Characteristic	**Value**	**Unit**
Open loop travel 0-100 V	$90 \pm 20\%$	[μm]
Resolution	0.9	[nm]
Static large signal stiffness	$10 \pm 20\%$	[N/μm]
Push/Pull force capacity	800/300	[N]
Electrical capacitance (@1 V, 1000 Hz)	$9 \pm 20\%$	[μF]
Dynamic operating current coeff.	12.5	[μA / Hz / μm]
Unloaded resonance frequency	$6 \pm 20\%$	[kHz]
Mass (no cable)	$86 \pm 20\%$	[g]
Length	127	[mm]

Table 5.1: PI P-842.60 specifications [22]

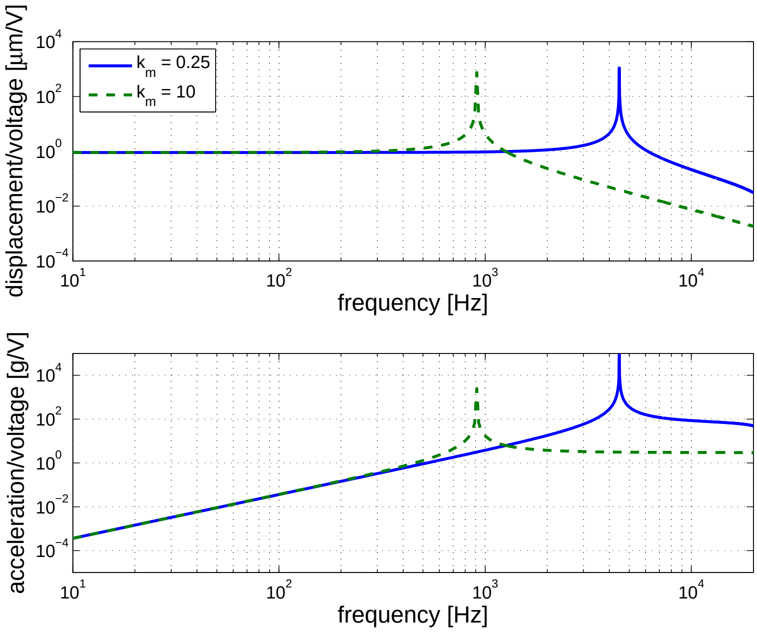

Figure 5.2: Displacement/Acceleration FRF, $k_m = 0.25, 10$

5.1.1 Test bench simulations

Of particular interest is the frequency response function of the various quantities (displacement, acceleration, current, and stress) in order to choose the proper electronic components and sensors, and to avoid breakage (due to exceeding current and/or stress).

Figures from 5.2 to 5.3 shows the aforementioned frequency response functions. To limit the displacement the voltage amplitude must be kept below 0.1 V. In such case the current requirements are 10 mA. It can be seen that the maximum stress with such voltage level is always below 100 MPa and the acceleration peak is 10^4 g. It must be noted though that the mathematical models presented do not include losses in the piezoelectric material. These losses will very likely affect the actuator's behavior, reducing the amplitude of the peaks found in Fig. 5.2 and 5.3.

Overall the simulations suggest to keep voltage amplitude near resonance in the range 0.01 V - 0.1 V. Should this be the case, the current requirements, the maximum acceleration, and the stress never exceed the aforementioned limits.

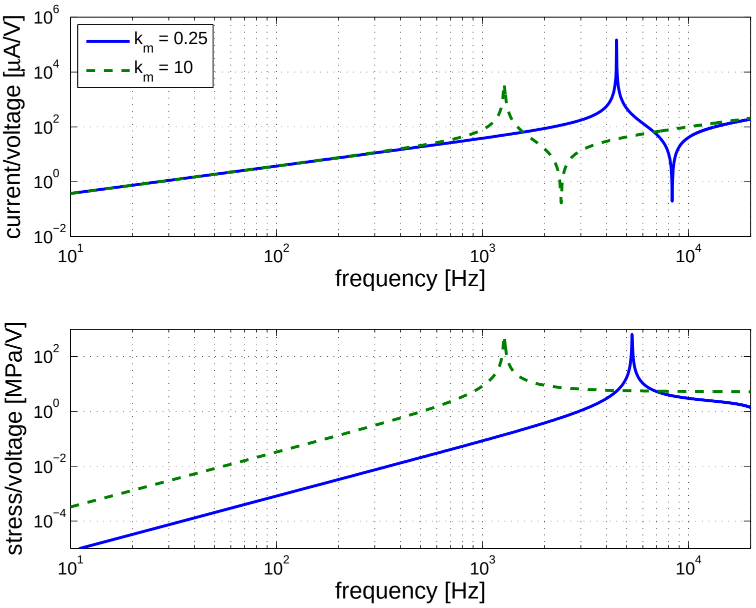

Figure 5.3: Current/stress on piezo FRF, $k_m = 0.25, 10$

5.2 Amplifier design

The amplifier is a conceptually simple device that takes an input voltage signal and produces as output an amplified voltage signal. An ideal amplifier shows a constant ratio between input and output voltage, no time delay between the two signals, no distortion, and no additional noise. Such characteristics can be met to certain extent, given that no ideal amplifier can be manufactured. In a practical case, a suitable amplifier will have a flat frequency response function and no or very limited delay in a desired frequency range; distortion and noise should be al low as possible.

The starting point for the design of an amplifier for driving a piezoeletric actuator is the gain, that is the ratio between output and input voltage. Typically piezoelectric devices require a voltage ranging from tens to hundreds of volt; in the case of multilayer actuators the typical voltage is about -20 V / +120 V. Another important specification is the current requirements, cannot be specified a-priori without a knowledge of the system the piezoelectric actuator is going to drive.

Based on the results from previous simulations, the specifications for the voltage amplifiers are stated as shown in Tab. 5.2, beside general characteristics as being linear, not introducing noise or delays. The voltage gain was chosen in order to to exploit the DC power supplies available (± 30 V) and on the fact that driving signal can be

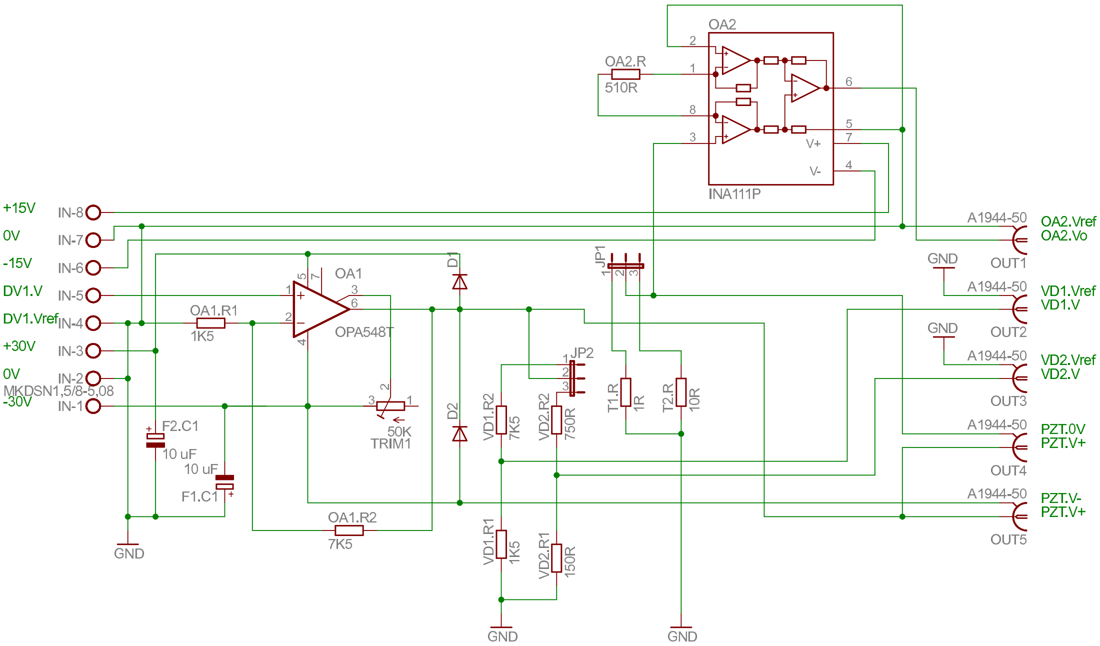
OA2
OA2.R
510R
INA111P
V+
V-
+15V
0V
-15V
DV1.V
DV1.Vref
+30V
0V
-30V
MKDSN1,5/8-5,08
IN-8
IN-7
IN-6
IN-5
IN-4
IN-3
IN-2
IN-1
OA1
OPA548T
OA1.R1
1K5
F2.C1
10 uF
10 uF
F1.C1
GND
50K
TRIM1
OA1.R2
7K5
D1
D2
VD1.R2
7K5
VD2.R2
750R
VD1.R1
1K5
VD2.R1
150R
JP1
JP2
T1.R
1R
T2.R
10R
GND
GND
A1944-50
OA2.Vref
OA2.Vo
OUT1
GND
A1944-50
VD1.Vref
VD1.V
OUT2
GND
A1944-50
VD2.Vref
VD2.V
OUT3
A1944-50
PZT.0V
PZT.V+
OUT4
A1944-50
PZT.V-
PZT.V+
OUT5

Figure 5.4: Amplifier electric scheme

generated at 10 V.

Piezoelectric actuators in general can be approximated as a capacitive load from the electrical point of view when driven off resonance and as a resistive load when driven near resonance (see [1] for further details on equivalent electric circuit representation in resonance conditions). The amplifier scheme proposed in [33] has been adopted. It is based on the use of an operational amplifier with feedback control, such as the Texas Instruments OPA548 [27]. This operational amplifiers can be driven either to +60 V or to ± 30 V, in respectively single or double supply mode, and can supply continuously 3 A current with peaks of 5 A. The gain bandwith over a resistive load of 8 Ω is 1 MHz and the total harmonic distortion plus noise at 1 kHz is 0.02 %. In other words, the OPA548 completely meets all the requirements of Tab. 5.2 and is even more performing in some respects (bandwidth and current).

Figure 5.4 shows the electric scheme of the amplifier. The "heart" is the OPA548, placed in the left part of the scheme, wired in the inverting configuration so that the

voltage gain	6
maximum current	100 mA
frequency range	1 Hz - 20 kHz

Table 5.2: Amplifier requirements

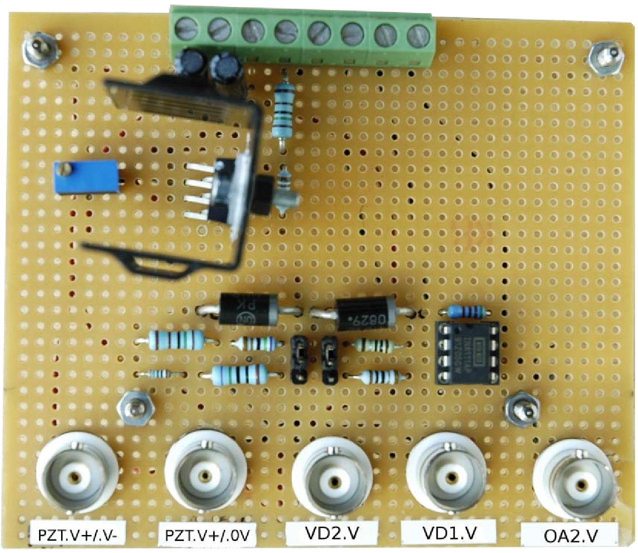

Figure 5.5: Amplifier

gain is 6; a trimmer (TRIM1) allows adjusting the current limit. Directly wired to the voltage output terminal of the operational amplifier are two diods that permit an extremely quick discharge of current returning towards the voltage source. Their presence is of paramount importance given the capacitive behaviour of the piezoelectric actuator. Two voltage dividers are then placed in order to measure the actual output voltage. Each presents a different total resistance; at most one can be connected. The basic idea behind the introduction of these "multiple resistance" voltage divider was to stabilise the output voltage in case of need. Looking at the right part of the electric scheme, one can see the resistive load (T1 and T2) which can be alternatively selected. They both serve as a measuring resistor (the voltage drop across them is read by the instrumentation operational amplifier Texas Instruments INA111 [27]) and as circuit element whose influence on the system's dynamics is to be evaluated. The gain of the INA111 is set to 100 by connecting a 510R resistor (1 % accuracy). Furthemore two electrolitic capacitors were placed between the power input voltage connection to filter out noise.

The input terminals are the power supply voltage for the OPA548 -30V/0V/+30V, the voltage supply for the INA111 -15V/0V/+15V, and the voltage signal that is to be amplified. The output terminals include the amplified voltage across the measuring resistor, the two voltage dividers reading, a zero to amplified voltage output, and a -30V to amplified voltage output. These outputs are to be connected to the load. They can thus provide a -30 V to +30 V or a 0 V to +60 V range. The assembled amplifier

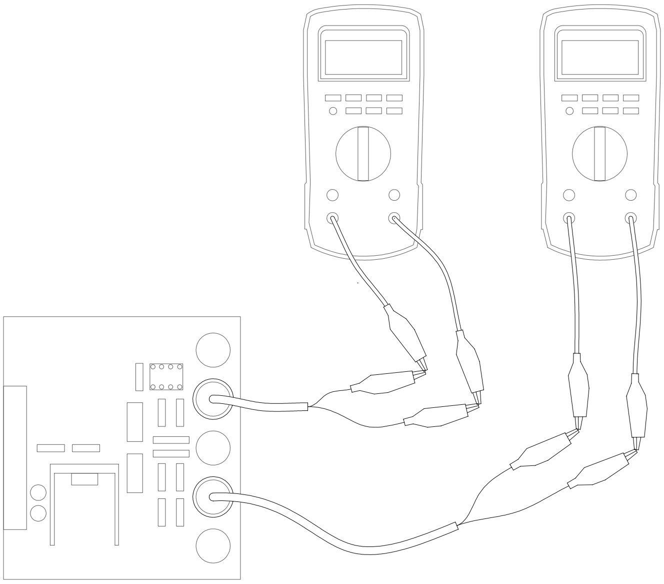

Figure 5.6: Voltage measuring set-up

is shown in Fig. 5.5.

5.2.1 Calibration

Comprehenive testing was made in order to verify that the amplifier met all the requirements. Two DC power supplies were employed: a TTi EL 302 D (dual power supply ± 30 V, 2 A per channel) and an Agilent E3631 A (0 - +6V 5A/± 25 V 1 A) that served both as power supply for the instrumentation operational amplifier and as a DC signal source.

First the output voltage was read on the output terminals employing two digital multimeters (Fluke 79 III and Fluke 111 [9]). The measuring set-up is shown in Fig. 5.6. The input signal was swept from -5 V to +5 V by steps of 0.5 V and the corresponding output voltage was read. Figure 5.7 shows the measurements: The output signal is very linear except towards the ends of the graph where the voltage limit of the amplifier is reached.

The same measurement has been made for the voltage dividers readings. Figure 5.8 reports the results and they are very much satisfactory. In particular the gain of the two amplifiers has been computed (except for the values of voltage signal close to zero) and the results (see Fig. 5.8) shows a variation that is definitely negligible (standard deviations of 0.0048 and 0.005 for the voltage dividers VD1 and VD2 respectively).

Output current was monitored by connecting a resistive load (a 100R resistor, 1 %

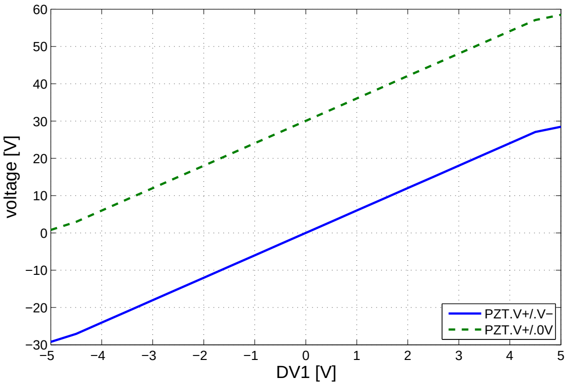

Figure 5.7: Open loop output voltage

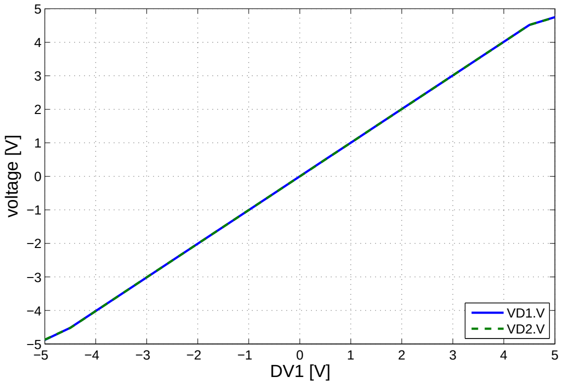

Figure 5.8: Open loop voltage readings

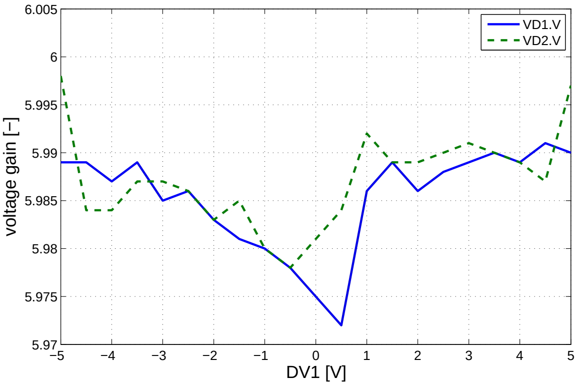

Figure 5.9: Voltage dividers gain

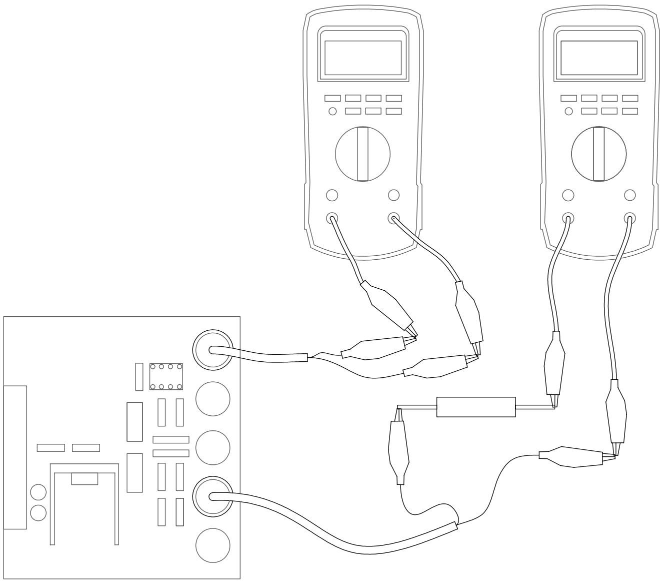

Figure 5.10: Current measuring set-up

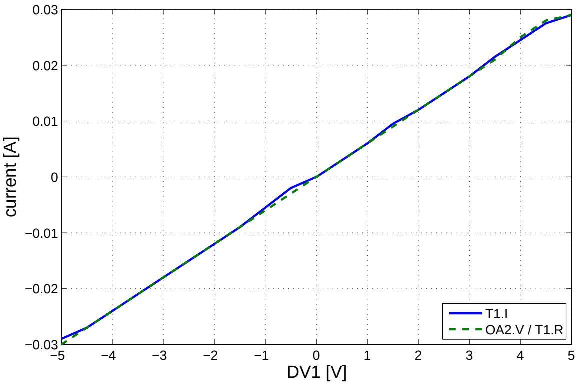

Figure 5.11: Current flowing into circuit

accuracy) and measuring both the current flowing and the instrumentation amplifier voltage output. The measurement set-up is shown in Fig. 5.10.

The current flowing into the circuit is measured directly by the digital multimeter Fluke III and indirectly via the instrumentation amplifier. Figure 5.11 shows the measured current and the current calculated from the amplified voltage readings. The current is calculated dividing the voltage reading by the appropriate operational amplifier gain and the resistance of the resistor T1. The calculated current fits extremely well the measured data with the sole exception of the negative values close to zero. This mismatch is considered to be due to the very small values of the current, which is very close to the digital multimeter resolution.

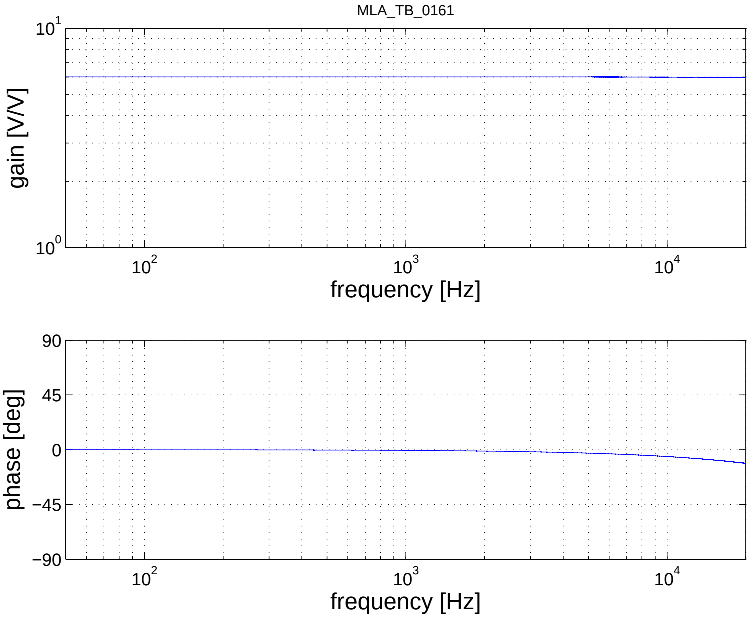

Figure 5.12: Frequency response function of supplied voltage

The frequency response fuction of the amplifier when a purely resistive load is connected is of paramount importance, since it shows whether the amplifier introduces or not distortions or noise. To this end the amplifier input and output signals have been connected to a data acquisition system (LMS Scadas Mobile, 16 channels of analog input, 24 bit per channel, 46 kHz ADC bandwidth). The front end generated a swept sinusoidal voltage of 1 V over a frequency range of 50-20000 Hz. The sampling frequency was set to 51200 Hz; a highpass filter of 0.5 Hz was activated. The amplifier was connected to a 1K resistor (1 % accuracy). The FRF of the supplied voltage is nearly flat and equal to 6 in all the desired frequency range. The phase shows some feeble deviation from zero, approximately visible from 1 kHz and reaching -11° at 20 kHz (see Fig. 5.12). The FRF of the supplied current is shown in Fig. 5.13. As read from the instrumentation operational amplifier, the current follows identically the trend of the voltage FRF.

5.3 Sensors

The test bench is equipped with a displacement laser sensor and an uniaxial accelerometer placed on the mechanical load. The displacement laser sensor is a MicroEpsilon optoNCDT 1402 [17]. This sensor presents a 5 mm measuring range with maximum

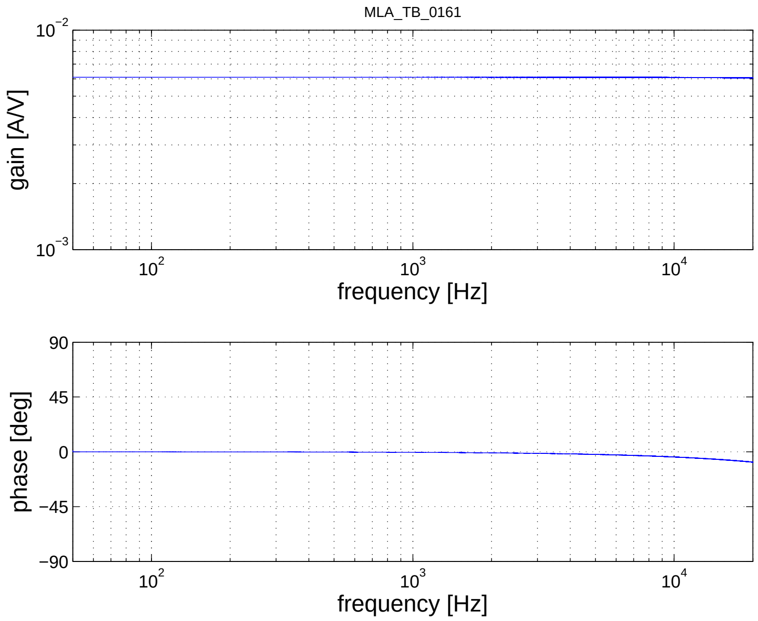

Figure 5.13: Frequency response function of supplied current

resolution of 0.6 μm. Resolution and linearity are respectively equal to 0.01 % and ± 0.18 % of full scale, that is 0.5 μm and ± 0.9 μm. The measuring rate can be set up to 1.5 kHz.

The accelerometer is a Dytran 3035 BG miniature piezoelectric accelerometer, featuring 50 g of full scale with sensitivity of 100 mV/g [7]. This sensor has a resonant frequency of 45 kHz, a linearity of ± 1 % of full scale, that is ± 0.5 g. Its weight is 2.5 grams, that is roughly the 21 % of the mass of the actuator's active part. The accelerometer requires a flat surface for adhesive mount.

5.4 Mechanical load

The actuator will be loaded with some different inertial loads. These loads need to present a M5 threaded hole and a flat top surface so that the accelerometer can be mounted and displacement can be read. Few loads were manufactured out of aluminium and steel weighing 2, 5, and 70 grams. Their masses relative to that of actuator's active part is respectively 16.67 %, 41.67 %, and 58.33 %. When equipped with the accelerometer, and considering the mass of the mechanical interface, the ratio between the load mass and the active part mass (previously defined as normalized load mass coefficient k_m) is respectively 0.625, 0.875, and 6.29. Should the actuator be tested

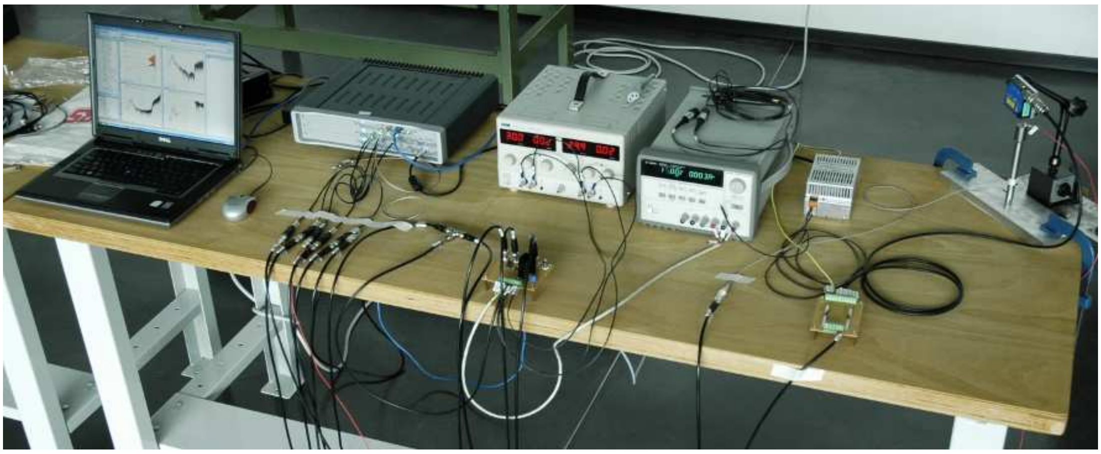

Figure 5.14: Test bench set-up

with no load and thus no accelerometer k_m reaches 0.25. The test bench as designed is shown in Fig. 5.14.

Chapter 6

Experimental analysis and models validation

The experimental campaign constitutes the final step in the process of analysing the system. Different models were presented, simulations were run in order to investigate the dynamic behavior of a piezoelectric multilayer actuator. The test bench designed allows to verify all the models implemented, from all points of view. The results that are going to be presented cover the dynamic behaviour of the system excited by a periodic signal. Transient phenomena have not been investigated yet.

6.1 Experimental set-up

The test bench configuration has been largely described in the previous section: it is constituted by a commercial piezoelectric multilayer actuator (PI P842.60), a dedicated amplifier (in-house developed and assembled), a LMS Scadas Mobile data acquisition system, and a personal computer. The test bench is equipped with some sensors in order to measure displacements, accelerations, voltages, and currents.

6.1.1 Description of the instrumentation

The LMS Scadas Mobile SCM05 is a data acquisition system and signal analyzer featuring up to 40 input analog channels, two analog output channels, two tachometric input channels, and a GPS receiver. Each channel has a 24-bit resolution and can be sampled at up to 102.4 kHz. Data is sent real time (2.2 megasample per second) through an ethernet connection to any personal computer running LMS software such as TestExpress or TestLab. All sensors and voltage signals are connected to this system, while an output channel is wired to the corresponding input terminals of the amplifier. Channel properties are set so that input voltages are scaled and expressed in the appropriate units, that is ampere on channel 1 (T1.I), volt on channel 2, 3, and 4 (DV1, VD1, VD2), meter on channel 5 (PZT.u), and g (9.81 m/s^2) on channel 6 (PZT.upp). These last two channels are connected respectively to the displacement laser sensor and to the miniature accelerometer. Channel 1 takes as input the amplified voltage OA2.V from the instrumentation amplifier and scales it in order to show the corresponding current.

6.1.2 Measuring methodology

No particular methodology was followed in carrying out measurements. Each measurement type was repeated three times in order to have a small statistical basis. Measurements were basically of two kinds: a constant frequency sine signal or a frequency sweep sinusoidal signal across a frequency range. The former was used to check the low-frequency behaviour of the multilayer actuator and to investigate the voltage-displacement relation, while the latter was employed to analyse the dynamic behaviour of the system. Care was nevertheless taken in starting the measurements only after the accelerometer settling time had passed (few seconds, being 0.5 s the discharge time constant of the sensor).

6.2 Static behavior

The relation between input voltage and displacement was analysed by slowly varying the input voltage amplitude from 0 V to 60 V (that correspond to generating a signal from -5 V to +5 V at 1 Hz), as Fig. 6.1 shows.

Magnifying Fig. 6.1, a closer look on the displacement-voltage relation can be taken. There is a sort of delay in the displacement response; Fig. 6.2 shows the superposition of the driving voltage curve and the displacement curve. Should Eq. 1.1 hold, the two curves would be coincident or slightly offset due to different axis scaling.

A better understanding of the relation between the two quantities can be achived by eliminating time from the graphical representation. Figure 6.3 reports the displacement-voltage curve. It can be easily observed that two parts can be distinguished: one below 35 V and one above; each can be approximated as a straight line. The one up to 35 V is quite flat: the displacement is less than 10 μm for 35 V of driving voltage. In the second part the actuator proves to be much more responsive travelling 40 μm more

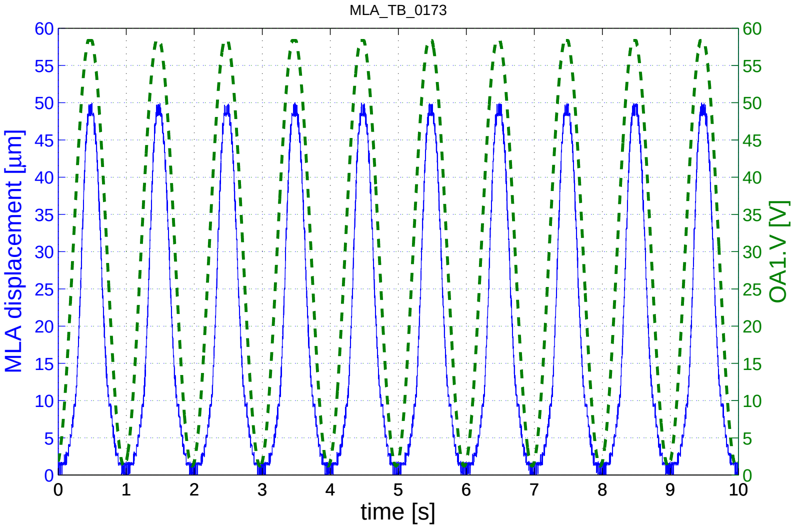

Figure 6.1: MLA displacement under large voltage excitation. Sampling frequency 2048 Hz

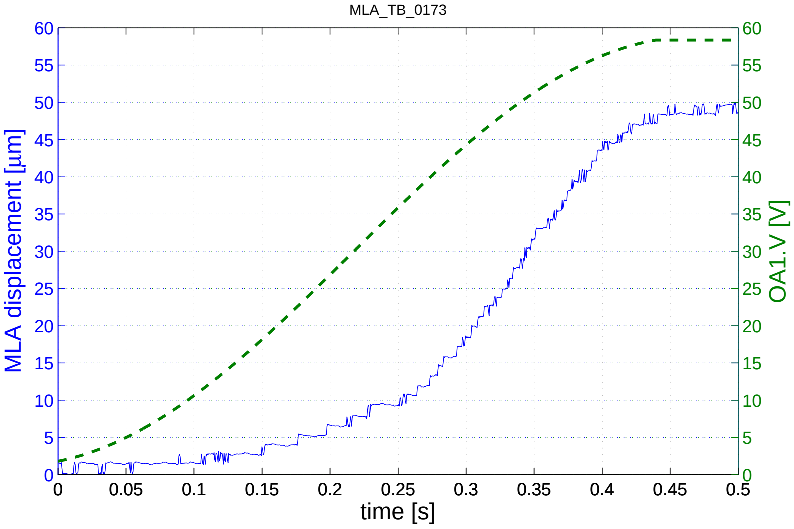

Figure 6.2: Half period of MLA displacement under large voltage excitation. Sampling frequency 2048 Hz

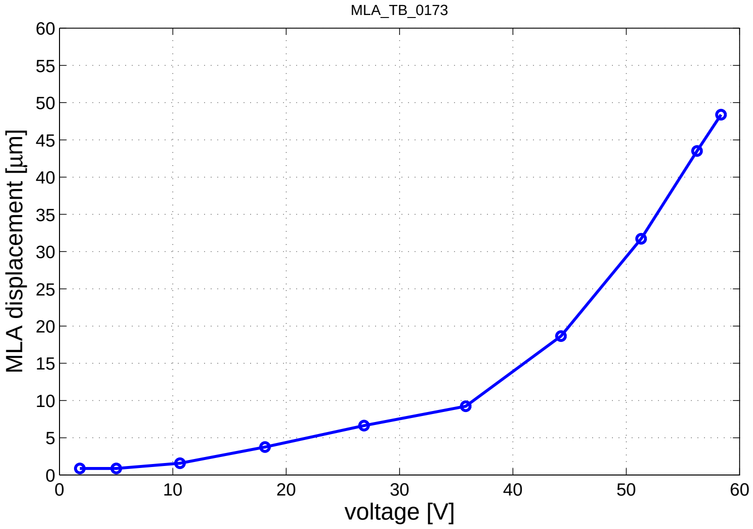

Figure 6.3: Relation between voltage and displacement for large signal excitation

under approximately 25 V of extra driving voltage. The slope of the two curves can be calculated elementary as 0.286 μm/V and 1.6 μm/V respectively. The value expected from Eq. 1.1 is

$$\frac{u}{V_s} = L\frac{e}{c^E} = 0.9\ \mu\text{m/V} \tag{6.1}$$

where the values obtained in chapter five had been employed. This value corresponds to the data declated by the manufacturer (90 μm at 100 V). Anyhow, the behaviour shown by the actuator proves that the relation between voltage and displacement is not linear, thus giving a confirmation that the simplifications introduced in the constitutive equations are valid only for low intensity electric fields (see appendix B).

6.3 Quasi-static behaviour

Quasi static behavior was investigated by driving the system at a low frequency sinusoidal signal. This signal would result in an almost in-phase load displacement and from the electrical point of view the actuator would be equivalent to a capacitor with constant capacitance (when the signal amplitude is small).

Raising the voltage amplitude would result in larger deformation thus displacements and consequently in larger capacitance. The actuator's capacitance can be calculated starting from the measured electrical quantities as

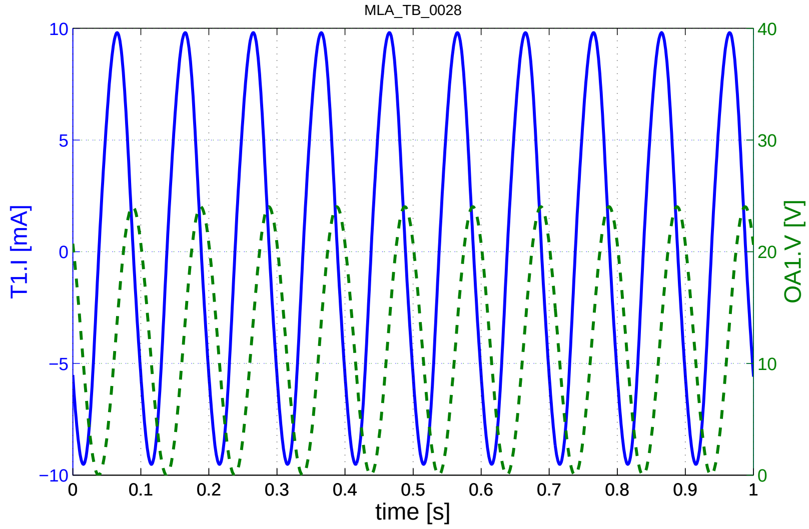

Figure 6.4: Electrical quantities in a 24 V p-p 10 Hz sine excitation

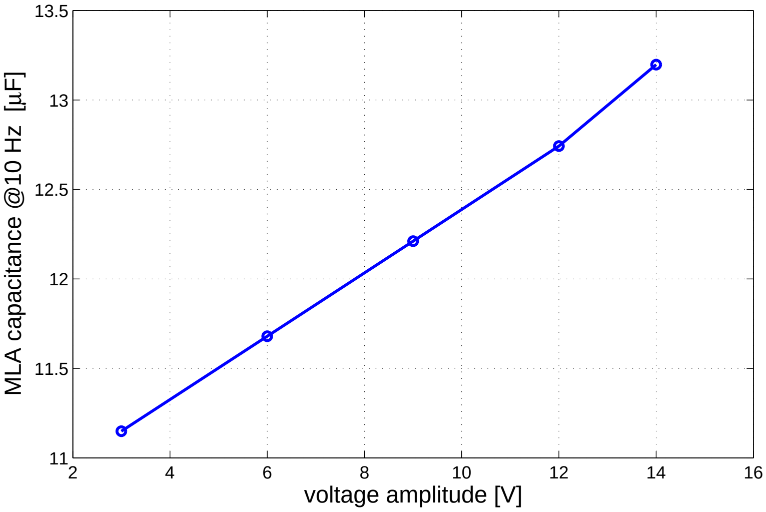

Figure 6.5: Relation between capacitance and voltage at low frequencies

$$C = \frac{I}{\omega \left(V_s - RI \right)} \tag{6.2}$$

making use of well-known relations for RC circuits. In this way the relation between capacitance and voltage amplitude (at a certain frequency, 10 Hz in this case) can be found, as shown in Fig. 6.5.

The capacitance is remarkably dependent on driving voltage level (the slope of the curve is 0.182 μF/V) at least in the voltage range considered. The variation could be due to the different thickness of the piezoelectric layer: the higher the driving voltage, the higher the deformation and thus the thickness of the piezoelectric layer. An increased thickness results in a larger electric capacitance of the actuator.

Nevertheless it must be noticed that the actuator's capacitance calculated in this manner is sensibly larger than the value read on the actuator's datasheet. As seen in Tab. 5.1, the declared capacitance is 9 μF measured at 1 kHz, while the values reported in Fig. 6.5 range from 11 μF to 13 μF at 10 Hz. The different frequency at which the capacitance has been measured should not invalidate the considerations made since the capacitance of a piezoelectric actuator is proportional to the driving frequency.

6.4 Dynamic behaviour

The dynamic behavior of the system over a large range of frequencies can be analysed by driving it with a sinusoidal signal of varying frequency. In particular the frequency of the signal can be swept either linearly or logarythmically over a time interval; in the former case equal time is given to all frequencies, while in the latter more time is allocated for lower frequencies. Logarythmic sweeping is thus more suitable for analysing also lower frequencies: in fact at lower frequencies it takes more time for complete periods to pass. Sinusoidal sweep gives a rather uniform excitation in a wide frequency range, therefore the FRF calculated from the measured data can be considered accurate.

The system will be tested in different configurations, emphasis will be put on the influence of the load inertia on the overall dynamics. The FRF will be calculated for the measurable quantities, that are current and acceleration. All the voltage amplitudes reported from now on are referred to the values generated before amplification.

Figure 6.6 shows the frequency response function of the current when the actuator is unloaded. As previously pointed out, that does not mean the load mass is zero, since the inertia of the actuator's mechanical interface has to be taken into account;

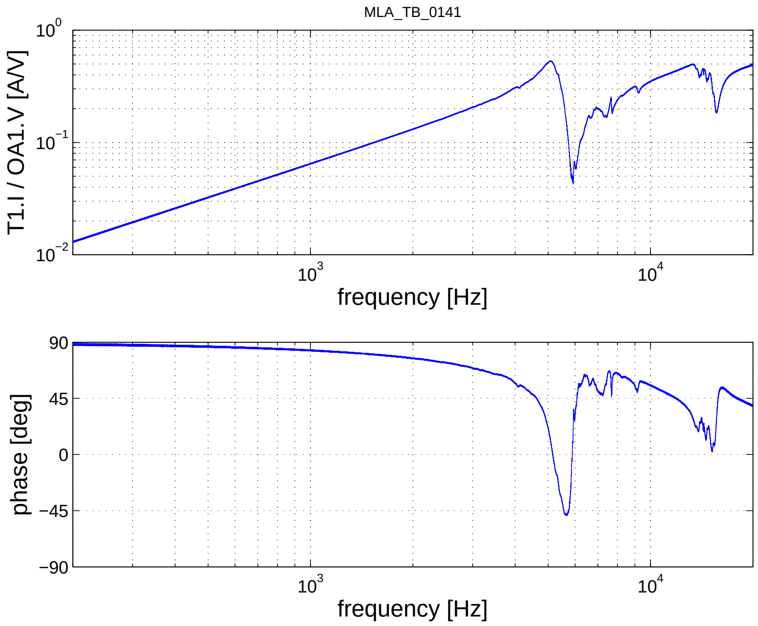

Figure 6.6: Current FRF in the range 200 Hz - 20 kHz, $k_m = 0.25$. Voltage amplitude 0.12 V, sampling frequency 102.4 kHz, sweep time 10 s.

therefore $k_m = 0.25$. The plot shows a linear behavior roughly up to 2 kHz and then there is a resonance peak at 5056 Hz. At higher frequencies three more phenomena can be seen: the first anti-resonance peak at 5936 Hz, a second resonance peak at 13.33 kHz, and a second anti-resonance peak at 15.63 kHz. In the linear part of the curve the current gains one order of magnitude per decade, in complete accordance with RC circuit analogy. The phase is 90° shifted with respect to driving voltage in the linear part and that too is in accordance with RC circuit analogy. In this configuration the acceleration cannot be measured.

Figure 6.7 shows the current frequency response function of the current when the actuator is loaded an the accelerometer is mounted. In this configuration $k_m = 0.63$ and the acceleration can be measured. With respect to the previous figure, the current FRF shows the same frequency dependence. The resonance and anti-resonance peaks are shifted to lower frequencies (first and second resonance at 4294 Hz and 12.27 kHz, first and second anti-resonance at 5209 kHz and 12.87 kHz). The same can be said for the phase plot.

Figure 6.8 shows the current frequency response function of the system when $k_m = 6.3$. With respect to the previous measurements, the curve shows much lower oscillations at frequencies higher than the first of resonance. Only the first resonance and

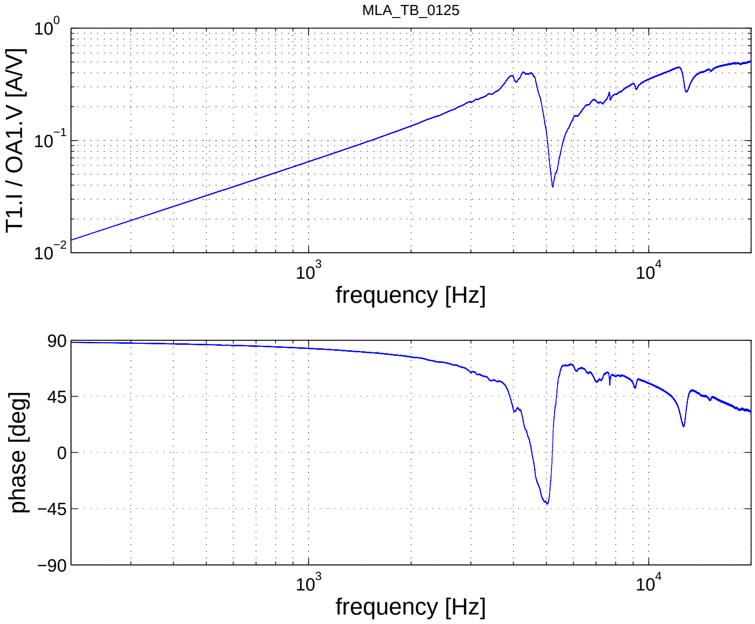

Figure 6.7: Current FRF in the range 200 Hz - 20 kHz, $k_m = 0.63$. Voltage amplitude 0.12 V, sampling frequency 102.4 kHz, sweep time 10 s.

anti-resonance peaks can be found at 1876 Hz and 2172 Hz. The same can be said for the phase plot.

Looking at the acceleration FRF plots the same considerations can be made. Figures from 6.9 to 6.12 shows the FRF plots. The measurements have been carried out splitting the frequency range in two parts in order to set different voltage amplitudes. In fact at low frequency the acceleration would be too low to be measured.

All the acceleration FRF curves show a linear part in the low frequency range (Fig. 6.9 and 6.10) that ends invariabily before the first resonance frequency. In this part the acceleration gains two orders of magnitude per decade; once again this result is in accordance with the linear theory of piezoelectricity (see Eq. 1.5). It can be noticed that at low frequencies there are some sudden jumps of the phase from 180° to -180°; this behavior must be regarded to merely as a numerical artifact, not representative of real dynamic behavior. A minor resonance peak can be noticed at 300 Hz in both Fig. 6.9 and 6.10; it is believed that this resonance peak has nothing to do with the system dynamics itself but it is more likely due to the experimental apparatus. This hypothesis wuold be confirmed by the current FRF plot (see Fig. 6.7 and 6.8), where no resonance peak can be spotted at 300 Hz. Should the system present any kind of resonance, an increase in current absorption would occur.

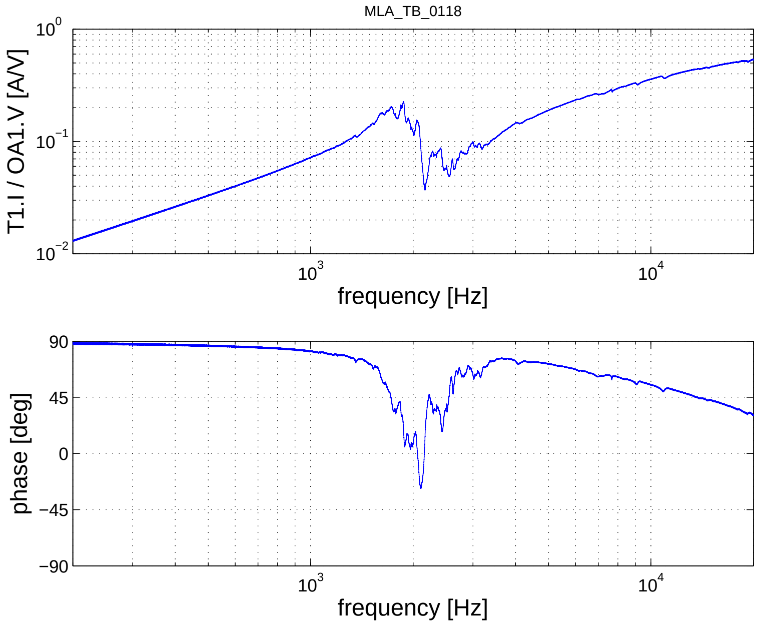

Figure 6.8: Current FRF in the range 200 Hz - 20 kHz, $k_m = 6.3$. Voltage amplitude 0.15 V, sampling frequency 102.4 kHz, sweep time 10 s.

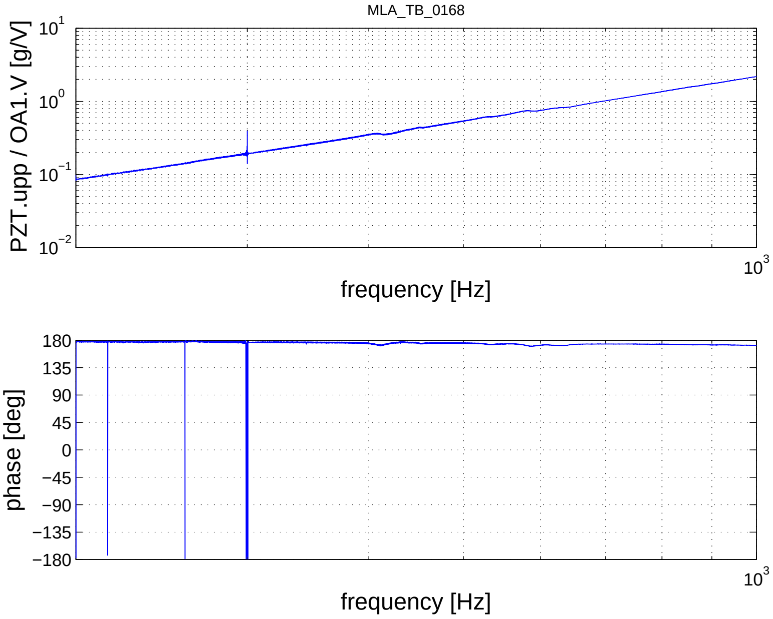

Figure 6.9: Acceleration FRF in the range 200 Hz - 1 kHz, $k_m = 0.63$. Voltage amplitude 1 V, sampling frequency 20.48 kHz, sweep time 15 s.

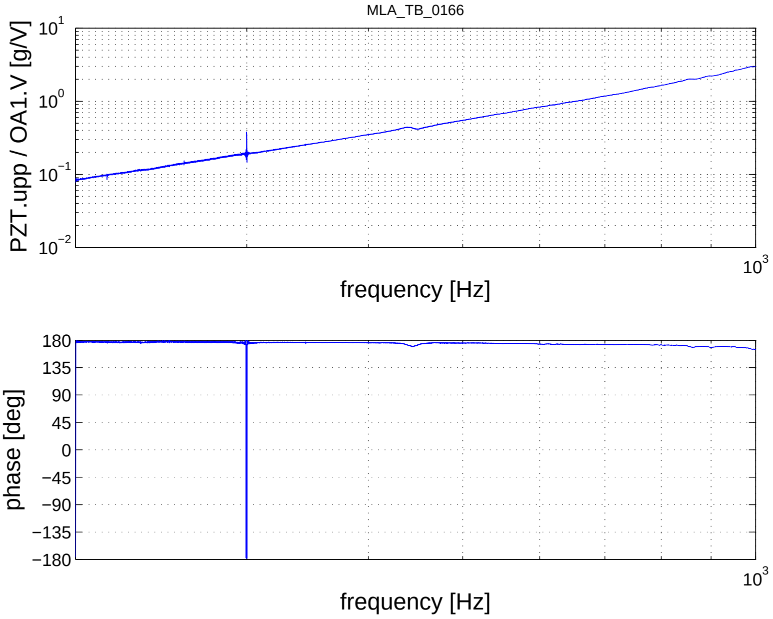

Figure 6.10: Acceleration FRF in the range 200 Hz - 1 kHz, $k_m = 6.3$. Voltage amplitude 1 V, sampling frequency 20.48 kHz, sweep time 15 s.

At high frequencies (Fig. 6.11 and 6.12) the resonance peaks can be easily identified. There are two resonances and one anti-resonance, as the current FRFs showed. With respect to the current plots, these are more disturbed, especially in between the two resonances for Fig. 6.11 and in correspondence of the first resonance for Fig. 6.12.

It can be observed that the current plots do not allow a clear identification of the second resonance and the anti-resonance frequencies when high inertial loads are present, especially with respect to the acceleration plots. This behavior favors acceleration measurements in the analysis of system driven at high frequencies.

6.5 Comparison with numerical data

After carrying out the experimental campaign is time to verify the numerical model implemented. A numerical model of the test bench for each mathematical model will be implemented and the FRF will be calculated. The method for calculating the frequency response function differs according to the mathematical model employed. In the case of analytical models, the FRF is calculated point-wise. Given a frequency range of interest, a vector of frequencies is considered (of course a larger vector results in smother line plots) and the analytical solution of the displacement, current, and

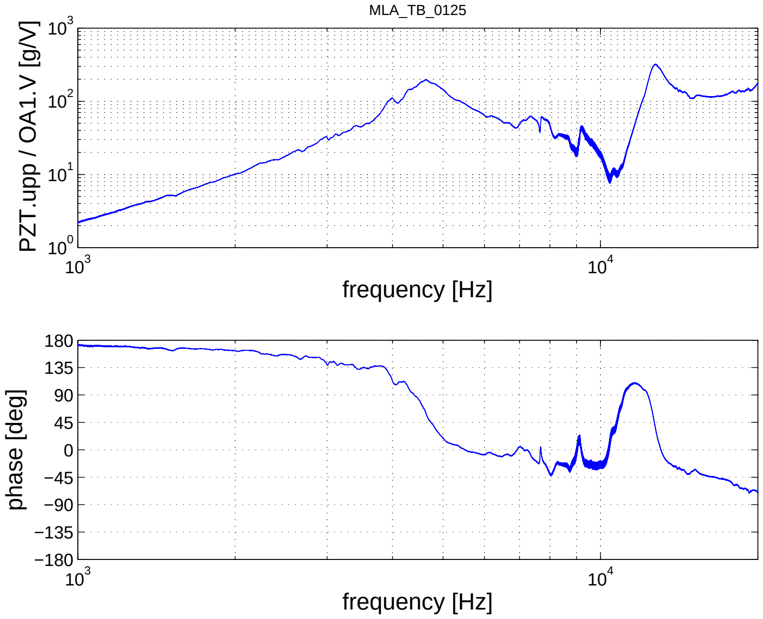

Figure 6.11: Acceleration FRF in the range 1 kHz - 20 kHz, $k_m = 0.63$. Voltage amplitude 0.12 V, sampling frequency 102.4 kHz, sweep time 10 s.

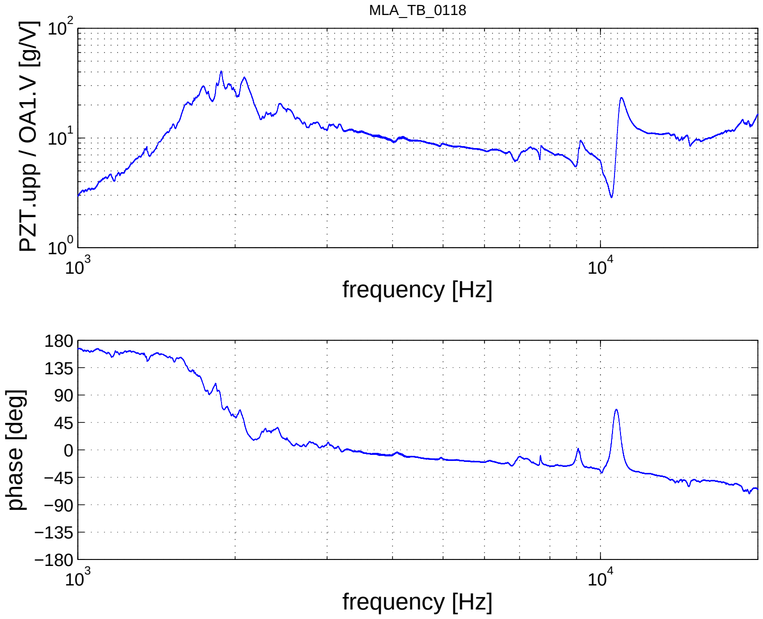

Figure 6.12: Acceleration FRF in the range 1 kHz - 20 kHz, $k_m = 6.3$. Voltage amplitude 0.15 V, sampling frequency 102.4 kHz, sweep time 10 s.

acceleration is found at each frequency. In the finite difference modelling the simulated impact testing is employed (as illustrated in chapter two). In this case best results are obtained for longer simulation times and a high number of elements. Either cases better results imply longer simulation times. In all the simulations, the frequency vector for the analytical models was composed by 1000 elements. The simulation time for such models (on a Intel Core 2 Duo 2.2 GHz processor equipped with 8 GB RAM) was of about 40 minutes for the MLM model and few tens of seconds for the BKM model. The FDM model was made by dividing each layer in 50 elements and considering a simulation time of 2 ms. The simulation time in these cases was much longer: the average simulation took 36 hours to complete. A simulation time this large is the result of carring out the calculation of approximately

$$50 \times 1525 \times \frac{2 \cdot 10^{-3}}{4.2 \cdot 10^{-10}} \approx 0.38 \cdot 10^{12} \tag{6.3}$$

unknowns.

The experimental data will be compared to the analytical bulk model (BKM, as extended in chapter five to simulate the dynamic behavior of multilayer actuators), to multilayer analtytical model (MLM), and to the finite difference model (FDM). Figures 6.13 from to 6.15 shows the various FRFs with different inertial loads. Each figure reports superposed the four curves resulting from either simulations or measurements.

Figure 6.13 shows the current FRF when the actuator is not loaded with any external load. As already stated, that condition is not equivalent to not having any inertial load; indeed the normalized load mass coefficient k_m is equal to 0.25 (see chapter 5 for further explanations). In the low frequency range (100 Hz to 3 kHz) the four curves are coincident, clear sign that the three models describe extremely well the dynamic behaviour of the system. From 4 kHz and on the mathematical models show a larger gain with respect to the actual system. This might be due to damping effects that where not taken into account in modelling. The resonance frequency, identified by the local maximum, occurs at a slightly lower frequency than predicted by the models. Once again this could be ascribed to the undamped modelling. Anyhow the MLM model is the most accurate one in predicting the first resonance frequency. At higher frequencies all the models fail; first of all the anti-resonance frequency, represented by the downward peak, is present in all curves but occurs at wrong frequencies. Once again best results are obtained by the MLM model although there is a large error (predicted 8.5 kHz against approximately 5.94 kHz measured). The other models predicts

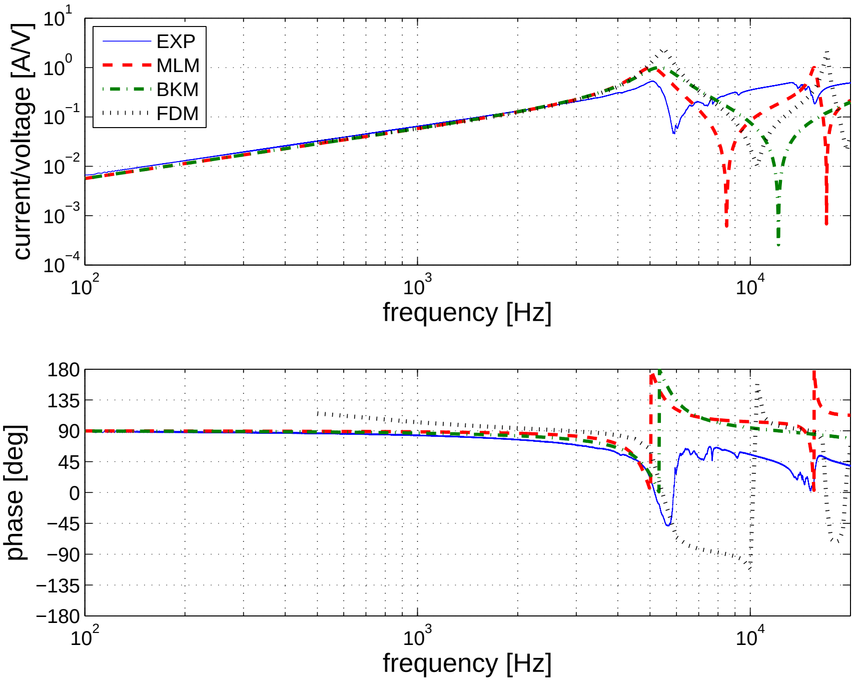

Figure 6.13: Current FRF - no external inertial load ($k_m = 0.25$)

the first anti-resonance frequency at approximately 10.5 kHz and 12.14 kHz for respectively the FDM and the BKM models. As previously pointed out in chapter three it is remarkable the difference between the two mathematical models. The MLM and the FDM curves show a second resonance right before the end of the analysed range, while the BKM model none. This is confirmed by the experimental evidence, although the resonance peak is hardly noticeable; on the contrary the anti-resonance downward peak can be easily seen. Simulated data places second resonance frequencies at 15.56 kHz and 17 kHz for the MLM and FDM models respectively, while the measured data shows it at 13.33 kHz (value read from the phase diagram). The second anti-resonance can be seen at 16.96 kHz and at 19.5 kHz for respectively the MLM and the FDM models; the measurements indicates that it occurs at 15.63 kHz. The MLM model is very accurate in identifying these second resonance and anti-resonance frequencies.

The phase plot can be commented similarly: repentinous changes in this phase indicates that a singularity (i.e. resonance or anti-resonance) occurred. With respect to the magnitude plots, the phase diagram allows a more precise evaluation of the resonances, either on numerical or simulated data.

Figures 6.14 and 6.15 reports the comparison between current FRFs when higher

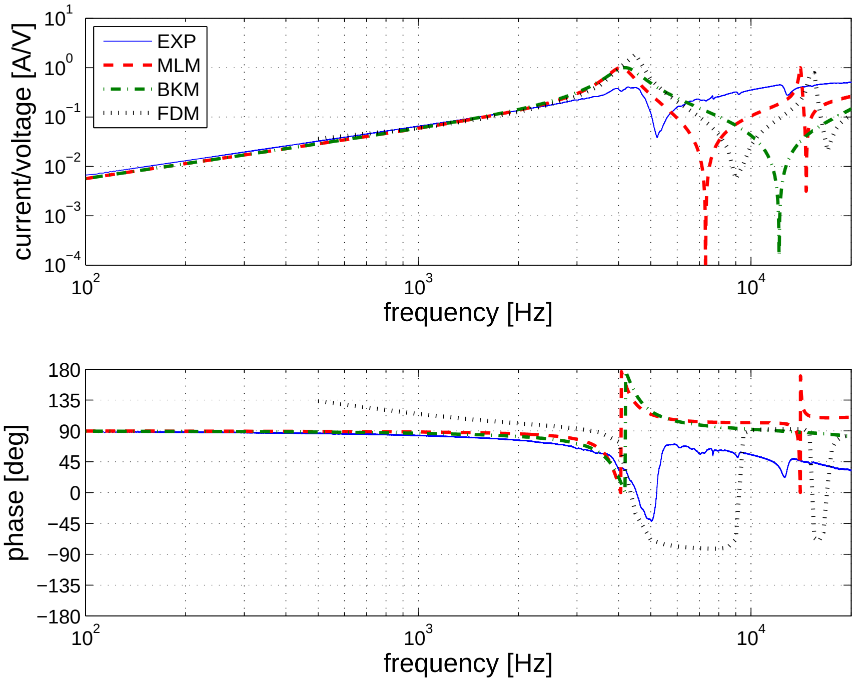

Figure 6.14: Current FRF - external inertial load $m = 2$ g, ($k_m = 0.63$)

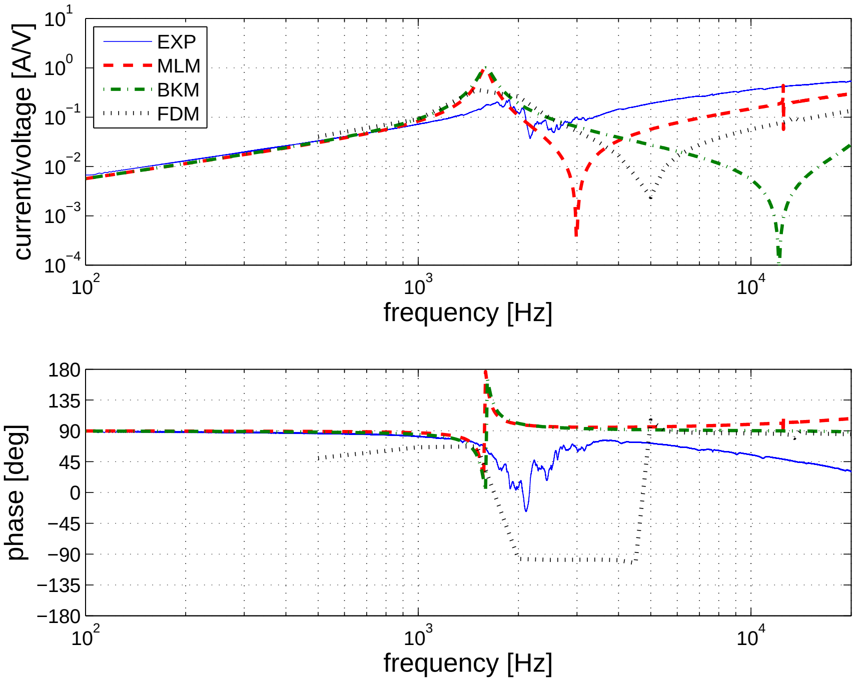

Figure 6.15: Current FRF - external inertial load $m = 70$ g, ($k_m = 6.3$)

inertial load are applied. As already seen the values of the resonance and anti-resonance frequencies are shifted to lower values. The simulated data is shifted as well; the same comments can be made for these curves. Table 6.1 sums-up all the results for the resonance and anti-resonance frequencies obtained either experimentally or numerically.

The current FRF at low frequencies can be compated to another values which is given in the actuator's datasheet. This parameter, called dynamic operating current coefficient, gives and indication of the current requirement for the functioning of the actuator ar a certain operating frequency and a fixed amplitude of displacement. For the actuator employed in the test bench the dynamic operating current coefficient is 12.5 μA/Hz/μm (see Tab. 5.1 for complete specifications of the actuator). It is thus possible to reconstruct the low frequency part of the current FRF plots shown in Fig. 6.13, 6.14, and 6.15 by calculating the slope of the current gain. The resulting value at 100 Hz is $2.25 \cdot 10^{-3}$ A/V, a value definitely smaller than that read in the aforementioned figures. In other words the current absorption of the system is larger than predicted; this fact could be due to two distinct aspect: the larger than declared capacitance (see previous section § 6.3) and the measuring resistor which raises the current requirements.

		Resonance [kHz]		Anti-resonance [kHz]	
k_m	Type	$f_R^{(1)}$	$f_R^{(2)}$	$f_A^{(1)}$	$f_A^{(2)}$
0.25	EXP	5.06	13.33	5.94	15.63
	MLM	5.03	15.56	8.50	16.96
	BKM	5.39	-	12.14	-
	FDM	5.50	17.00	10.50	19.50
0.63	EXP	4.29	12.27	5.20	12.87
	MLM	4.06	14.03	7.31	14.65
	BKM	4.18	-	12.16	-
	FDM	4.50	15.50	9.00	17.00
6.3	EXP	1.88	-	2.17	-
	MLM	1.59	12.50	2.99	12.52
	BKM	1.59	-	12.10	-
	FDM	1.50	13.50	5.00	-

Table 6.1: This table sums up all the values of the resonance and anti-resonance frequencies resulting from either experiments or simulations

Conclusions

The aim of the present work was to investigate the dynamic behaviour of a mechanical system driven by a piezoelectric multilayer actuator (MLA). Fairly simple in construction, MLAs are far more complicated objects to analyse from the dynamic standpoint. Indeed, the dynamics of any mono-dimensional piezoelectric media is ruled by the sound wave equation with time-dependent boundary conditions.

The models presented have different complexities, reflecting the different purposes which they have been conceived for. The analytical bulk modelling (BKM) is directly derived from the theory of linear piezoelectricity as presented in [1] and in [34]. This model is extended to MLA by simply considering a very thick layer of piezoelectric material and including a driving circuit. Such modelling has a very limited number of parameters, it is very easy to implement and requires a modest processing power. Obviously this model is based on a great simplification of the actuator's real structure; nevertheless very interesting results are obtained in certain conditions. Furthermore this model gives results only for a periodic excitation, failing to describe transient behaviour. Herein lied the motivation to implement a finite difference model (FDM). This model is much more flexible, allows analysing the system in transient conditions, can be employed to study the response to harmonic excitation, and can include a much larger variety of loading conditions. On the contrary results depends on the level of discretization and may require high-end processing capabilities. The multilayer analytical model is somehow a trade-off between the "exactness" of the analytical model and the modelling accuracy of the finite difference model. Being an original contribution, this model was implemented to give a better description of the actuator's structure, being composed of alternating layers of piezoelectric material and electrodes. The contribution of the electrodes' inertia to the overall dynamics was taken into account, as well as the external load and the driving circuit.

An experimental campaign was carried out for the validation of the mathematical models, a necessary step to be taken. The choice of the test bench, quite essential in its design, was due mostly to the need of not introducing complex parameter identification that would interfere with the validation of the model. Indeed, the aim was to minimize the risk of attributing discrepancies between models and experiments to the parameters evaluation.

The three models provides substantially equivalent results in the low frequency region, that spans from static behaviour to first resonance frequency. Especially with high load inertia the results of the three models are equivalent, as reported in Fig.6.13, 6.14, and 6.15. The most substantial differences can be found in the identification of the anti-resonance frequencies; in this respect the three models yields different results. The most accurate is the multilayer analytical model; the finite difference model succedes in identifying two anti-resonance frequencies but the corresponding frequency values are far less accurate than the MLM model. The bulk analytical model is very inaccurate in this respect since it shows only one anti-resonance frequency in the given range.

The overall predicting behaviour of the mathenatical model is very satisfactory. In all the loading cases the three models describe very well the low frequency dynamic behaviour and identify very precisely the first resonance frequency. In this respect the “simple” BKM model provides very good results at a very limited cost in terms of processing capabilities. When the frequency range under consideration spans above the first resonance frequency the MLM model is more suitable. Emerging applications like the development of piezoelectric ultrasonic motors constituted by an MLA as active part may benefit from the accurate prediction of the high frequency dynamic behavior. The FDM model places itself somewhere in between the other two models in terms of accuracy. Nevertheless it must be noticed that, while the two analytical models are “exact”, the FDM model is discretization dependent. Therefore the model accuracy may improve if more elements are employed in modelling the actuator. In any case the FDM model is a extremely valuable design tool since it allows analysing the transient dynamics of a mechanical system driven by a piezoelectric MLA.

The present investigation was limited to the analysis of the system under a periodic excitation. Although the analytical models cannot describe the system’s dynamics in transient conditions, the FDM model definitely can. Thus the natural next step to be taken is that of measuring the dynamic response of the test bench under the excitation of transient signals such as step, ramps, impulses, etc. in order to validate the results provided by the FDM model.

Much can be done too in the field of parameters identification. In the present work a very straightforward technique has been employed, which in fact does not take into account any experimental evidence. It goes without saying that results could be largely improved by considering, for the parameters identification, some feedback from the experimental data. Black-box, grey-box techniques could be proficiently employed to this end.

From the modelling point of view, a simple model that could be used for control purposes would be highly desiderable. In fact the models presented are not suitable for implementing control strategies. Some authors consider piezoelectric MLAs as ideal constraints to the driven system for the constitutive equation relates directly strain and voltage [29]. It was proved that such approach does not yield accurate results, especially when the load mass is not much larger than the actuator's active part mass. Therefore a reasonably simple model could help design more accurate controllers.

Appendix A

Non-linear theory of electroelasticity for strong fields

The theory of electroelasticity studies the behaviour of a solid body subject to mechanical forces and electical fields acting upon it. The non-linear theory is valid for large deformations and strong electric fields [34].

Conventions

Scalars are generally represented with lower case letters (such as a), vectors with bold letters (such as $\boldsymbol{a}$). Unit vectors are represented by the letter “i” (either lower case or upper case). Unit vectors are orthogonal, thus

$$\boldsymbol{i}_i \cdot \boldsymbol{i}_j = 0 \quad \forall i, j : i \neq j$$

Tensors will be represented using the two-point Cartesian tensor notation. Repeated indexes imply summation

$$a_i b_i = a_1 b_1 + \ldots + a_{\mathrm{N}} b_{\mathrm{N}} \quad i = 1, \ldots, \mathrm{N}$$

$$a_{ij} b_i = a_{j1} b_1 + \ldots + a_{j\mathrm{N}} b_{\mathrm{N}} \quad j = 1, \ldots, \mathrm{M}$$

When a set of coordinates is represented by a vector $\boldsymbol{x}$ such as

$$\boldsymbol{x} = \{x_1, \ldots, x_{\mathrm{N}}\}^{\mathrm{T}}$$

the differentiation of a scalar function f with respect to a coordinate x_i is indicated by its index i using the comma notation,

$$f_{,i} = \frac{\partial f}{\partial x_i}$$

This expression alone can be interpreted as the gradient of the scalar function f. Higher order derivatives can be represented as follows

$$f_{,ii} = \left\{ \frac{d^2 f}{dx_1^2}, \ldots, \frac{d^2 f}{dx_{\mathrm{N}}^2} \right\}^{\mathrm{T}}$$

The differentiation of a vector-valued function $\boldsymbol{f}(\boldsymbol{x})$ with respect to $\boldsymbol{x}$ is written

$$\frac{d\boldsymbol{f}}{d\boldsymbol{x}} = f_{j,i} = \begin{bmatrix} \frac{df_1}{dx_1} & \cdots & \frac{df_{\mathrm{M}}}{dx_1} \\ \cdots & \cdots & \cdots \\ \frac{df_1}{dx_{\mathrm{N}}} & \cdots & \frac{df_{\mathrm{M}}}{dx_{\mathrm{N}}} \end{bmatrix}$$

The divergence of a vector-valued function $\boldsymbol{f}$ is

$$\nabla \cdot \boldsymbol{f} = f_{i,i}$$

while the vector product can be represented in a compact manner introducing the permutation tensor ε_{ijk}

$$\varepsilon_{ijk} = \boldsymbol{i}_i \cdot (\boldsymbol{i}_j \times \boldsymbol{i}_k) = \begin{cases} 1 & i,j,k = 1,2,3;\ 2,3,1;\ 3,1,2; \\ -1 & i,j,k = 1,3,2;\ 2,1,3;\ 3,2,1; \\ 0 & \text{otherwise} \end{cases}$$

where $\boldsymbol{i}_i$, $\boldsymbol{i}_j$ and $\boldsymbol{i}_k$ are three orthogonal unit vectors. Therefore

$$\boldsymbol{a} \times \boldsymbol{b} = \boldsymbol{c} \qquad c_i = \varepsilon_{ijk} a_j b_k$$

The curl of a vector-valued function $\boldsymbol{f}$ is

$$\nabla \times \boldsymbol{f} = \{\varepsilon_{ijk} f_{k,j} \boldsymbol{i}_i\}$$

The Kronecker delta is a unit matrix, whose generic element is δ_{ij}. An interesting property is

$$\boldsymbol{i}_j \cdot \boldsymbol{i}_K = \delta_{jk} \qquad \boldsymbol{I}_J \cdot \boldsymbol{I}_K = \delta_{JK}$$

From the properties of unit matrices, $\delta_{jk} = \delta_{JK}$

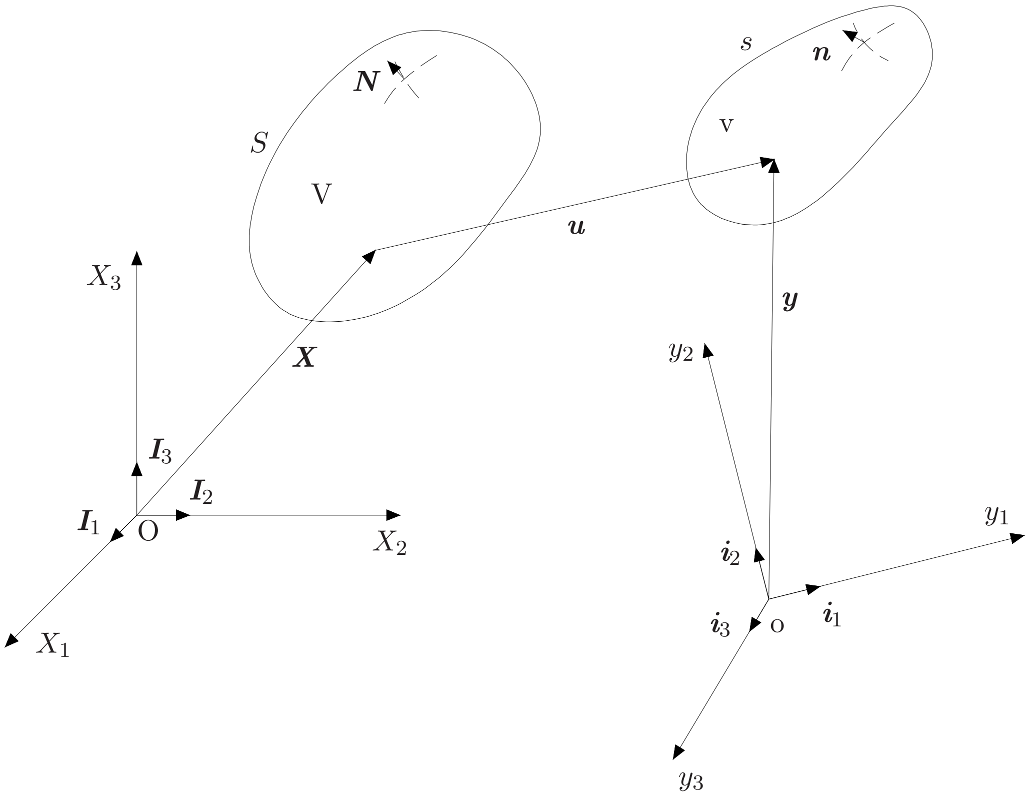

Figure A.1: Description of a deformable body

A.1 Kinematics of a deformable body

The theory of electroelasticity studies a continuum body that, starting from a reference configuration, undergoes rigid body motion and deformations. In the reference configuration the body is delimited by a surface S which contains a volume V. The surface can be described by an outward unit vector $\boldsymbol{N}$ that is always normal to it. At any subsequent time t, the body is in its present configuration; the same quantities are labeled respectively, s, v, and $\boldsymbol{n}$ (see Fig A.1).

A.1.1 Coordinate systems

The position of a continuum body can be described in its reference configuration by the position of all its points. A vector $\boldsymbol{X}$ carries out this task. While a rigid body can be fully described by six coordinates, a deformable body needs more information for a full description. This is why a vector $\boldsymbol{y}$ comes into play. The description of the position of the deformable body in the present time is given by $\boldsymbol{y}$. The vector $\boldsymbol{y}$ may be expressed in a different coordinate system than $\boldsymbol{X}$. In the most generic case

$$\boldsymbol{y} = Y_1\boldsymbol{I}_1 + Y_2\boldsymbol{I}_2 + Y_3\boldsymbol{I}_3 = Y_K\boldsymbol{I}_K$$

$$\boldsymbol{y} = y_1\boldsymbol{i}_1 + y_2\boldsymbol{i}_2 + y_3\boldsymbol{i}_3 = y_k\boldsymbol{i}_k$$

where $\boldsymbol{I}_K$ and $\boldsymbol{i}_k$ are the unit vectors of respectively the reference and present coordinate systems. The position vectors $\boldsymbol{X}$ and $\boldsymbol{y}$ can be expressed using the index notation as

$$X_I = \delta_{MI}X_M$$

$$y_i = \delta_{mi}y_m$$

With this notation, the position $\boldsymbol{y}$ can be written as

$$y_M = \delta_{Mi}y_i\boldsymbol{I}_K$$

where

$$\delta_{Mi} = \boldsymbol{I}_M \cdot \boldsymbol{i}_i$$

Since there will be no need for a moving present coordinate system, the reference and the present coordinate systems are chosen to be coincident (see Fig A.2). Therefore the following relations hold

$$\boldsymbol{I}_1 = \boldsymbol{i}_1, \boldsymbol{I}_2 = \boldsymbol{i}_2, \boldsymbol{I}_3 = \boldsymbol{i}_3$$

$$\delta_{kl} = \delta_{KL} = \delta_{kL}$$

A.1.2 Displacements

Due to rigid body motion or deformation a point can change its position. This translation is described by the displacement vector $\boldsymbol{u}$ such that the relation

$$\boldsymbol{y} = \boldsymbol{X} + \boldsymbol{u} \tag{A.1}$$

is satisfied. The present position $\boldsymbol{y}$ is a function of $\boldsymbol{X}$ and $\boldsymbol{u}$. Let it be expressed in the present coordinate system while $\boldsymbol{X}$ and $\boldsymbol{u}$ in the reference one; the Eq. A.1 can be written as

$$y_i = \delta_{iM}\left(X_M + u_M\right) \tag{A.2}$$

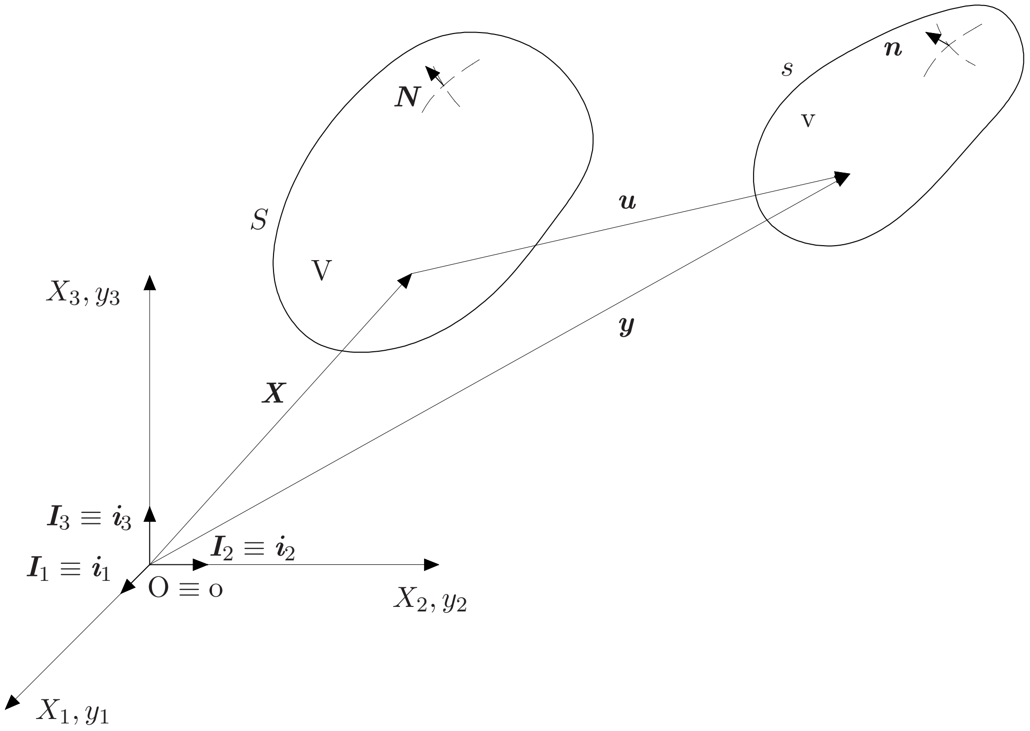
s
n
N
v
S
u
V
X_3, y_3
y
X
I_3 ≡ i_3
I_2 ≡ i_2
I_1 ≡ i_1
O ≡ o
X_2, y_2
X_1, y_1

Figure A.2: Simplified description of a deformable body

The differential of $\boldsymbol{y}$ is a material line element in the present configuration which comes from an original configuration $d\boldsymbol{X}$. The two are related by

$$dy_i|_{t \text{ fixed}} = y_{i,K} dX_K \tag{A.3}$$

The spatial derivative of $\boldsymbol{y}$ with respect to $\boldsymbol{X}$ gives the deformation gradient

$$y_{k,K} = \delta_{kK} + \delta_{kL} u_{L,K} \tag{A.4}$$

a matrix whose determinant J will be very important. It can be shown that the determinant can be calculated as

$$J = \frac{1}{6}\left(2\frac{\partial y_K}{\partial X_L}\frac{\partial y_L}{\partial X_M}\frac{\partial y_M}{\partial X_K} - 3\frac{\partial y_K}{\partial X_K}\frac{\partial y_L}{\partial X_M}\frac{\partial y_M}{\partial X_L} + \left(\frac{\partial y_M}{\partial X_M}\right)^3\right)$$

The relative position of two neighbouring points in their reference configuration is given by $d\boldsymbol{X} = \boldsymbol{X}^2 - \boldsymbol{X}^1$. In the present configuration their relative position is expressed by $d\boldsymbol{y} = \boldsymbol{y}^2 - \boldsymbol{y}^1$. The distance between these two points in either states can be computed from the following relations

$$dS^2 = dX_K dX_K = \delta_{KL} dX_K dX_L$$

$$ds^2 = dy_i dy_i = y_{i,K} dX_K y_{i,L} dX_L = C_{KL} dX_K dX_L$$

where $C_{KL} = y_{i,K} y_{i,L}$ is the deformation tensor. The determinant of the deformation tensor C_{KL} is equal to J^2. The elongation of this material element $ds^2 - dS^2$ can be related to the strain tensor by

$$ds^2 - dS^2 = 2S_{KL} dX_K dX_L$$

that can be written as

$$S_{KL} = \frac{1}{2}\left(C_{KL} - \delta_{KL}\right) = \frac{1}{2}\left(y_{i,K} y_{i,L} - \delta_{KL}\right) \tag{A.5}$$

Substituting Eq. A.4 into Eq. A.5 yields

$$S_{KL} = \frac{1}{2}\left(u_{K,L} + u_{L,K} + u_{M,K} u_{M,L}\right) \tag{A.6}$$

This strain tensor S_{KL} is symmetric.

A similar reasoning allows writing the relations between areas and volumes in the reference and present state. This can be accomplished considering respectively two and three material line elements. The resulting relations are

$$da_i = JX_{L,i}dA_L \tag{A.7}$$

$$d\mathrm{v} = Jd\mathrm{V} \tag{A.8}$$

where da_i is the projection of the infinitesimal area da along the n_i direction in the present state, dA_L is the projection of the infinitesimal area dA along the N_L direction in the reference state, v is the present volume and V is the reference one.

A.1.3 Velocity and acceleration

Velocity and acceleration of a material point can be calculated by differentiating Eq. A.2 with respect to time. It has to be noticed that since the position of a material point depends only on time, the expressions of the velocity $\boldsymbol{v}$ and the acceleration $\dot{\boldsymbol{v}}$ can be simplified in

$$v_i = \frac{Dy_i}{Dt} = \dot{y}_i = \left.\frac{\partial y(\boldsymbol{X},t)}{\partial t}\right|_{\boldsymbol{X}\ \text{fixed}} \tag{A.9}$$

$$\dot{v}_i = \frac{Dv_i}{Dt} = \ddot{y}_i = \left.\frac{\partial^2 y(\boldsymbol{X},t)}{\partial \tau^2}\right|_{\boldsymbol{X}\ \text{fixed}} \tag{A.10}$$

since the terms $\frac{\partial X_j}{\partial t}$ vanish. The derivative with respect to time of $X_{L,j}$ can be calculated as

$$\frac{D}{Dt}\left(X_{L,j}\right) = -v_{i,K}X_{K,j}X_{L,i} \tag{A.11}$$

The velocity gradient

$$\nabla \cdot \boldsymbol{v} = v_{i,i}$$

is a tensor that can be decomposed into a symmetric deformation rate tensor d_{ij} and the anti-symmetric spin tensor ω_{ij} defined as

$$d_{ij} = \frac{1}{2}\left(v_{i,j} + v_{j,i}\right) \tag{A.12}$$

$$\omega_{ij} = \frac{1}{2}\left(v_{i,j} - v_{j,i}\right) \tag{A.13}$$

The differentiation of Eq. A.5 with respect to time gives the relation between the strain rate $\dot{S}_{KL}$ and the deformation rate d_{ij}

$$\dot{S}_{KL} = d_{ij} y_{i,K} y_{j,L} \tag{A.14}$$

It can be shown that the derivative of the determinant J is equal to

$$\dot{J} = J v_{k,k} \tag{A.15}$$

A.2 Balance laws

Balance laws are physic laws based on experimental evidences. They are postulated as they constitute the basis for the formulation of the theory of continuum. Gauss'a and Faraday's law, conservation of mass, linear and angular momentum, and energy are used for developing the theory of electroelasticity.

A.2.1 Interactions

The interaction between a body and an electric field are due to the body crystal structure. This interaction can be studied the electric field induced phenomena by modelling the continuum as two interpenetrating bodies: one carrying the mass and the positive charges and the other massless carrying the negative charges. The results are an electric body force $\boldsymbol{F}^E$ and an electric body moment $\boldsymbol{C}^E$ acting upon an infinitesimal volume dV; an electric body power per unit mass w^E is generated as well. Their expressions are

$$F_j^E = \rho_e E_j + P_i E_{j,i} \tag{A.16}$$

$$C_i^E = \varepsilon_{ijk} P_j E_k \tag{A.17}$$

$$w^E = \rho E_i \dot{\pi}_i \tag{A.18}$$

where ρ_e is the present free charge density, E_j is the j component of the electric field $\boldsymbol{E}$, P_i is the i component of the polarization $\boldsymbol{P}$. $\dot{\pi}_i$ is the i component of the time derivative of the polarization per unit mass

$$\boldsymbol{\pi} = \frac{\boldsymbol{P}_i}{\rho} \tag{A.19}$$

A.2.2 Gauss's law

Gauss's law states that a flux of an electric field $\boldsymbol{E}$ through a closed surface s is equal to the total electric charge present in the volume v bound by the surface s divided by the electric constant ε_0. When considering a dielectric material, which is polarizable, the equivalent formulation

$$\oint_s \boldsymbol{D} \cdot d\boldsymbol{a} = \int_{\mathrm{v}} \rho_e d\mathrm{v} \tag{A.20}$$

is more convenient.

Eq. A.20 can be written in differential form using the divergence theorem

$$\oint_s \boldsymbol{D} \cdot d\boldsymbol{a} = \int_{\mathrm{v}} \nabla \cdot \boldsymbol{D} \, d\mathrm{v}$$

which can be written using the index notation as

$$\oint_s D_i da_i = \oint_s n_i D_i da = \int_{\mathrm{v}} D_{i,i} \, d\mathrm{v}$$

yielding the differential formulation

$$D_{i,i} - \rho_e = 0 \tag{A.21}$$

A.2.3 Faraday's law

The maxwell-Faraday's equation for quasi-static fields states that the line integral of the electric field $\boldsymbol{E}$ along any closed path is zero

$$\oint_l \boldsymbol{E} \cdot d\boldsymbol{l} = 0 \tag{A.22}$$

Using the Stoke's theorem the equation can be written as

$$\oint_l \boldsymbol{E} \cdot d\boldsymbol{l} = \int_s (\nabla \times \boldsymbol{E}) \cdot d\boldsymbol{a} = 0$$

that must hold for any surface s whose boundary is l. Therefore

$$\nabla \times \boldsymbol{E} = \boldsymbol{0}$$

that can be written in index notation as

$$\varepsilon_{ijk} E_{k,j} \boldsymbol{i}_i = \boldsymbol{0} \tag{A.23}$$

using the permutation tensor ε_{ijk}.

A.2.4 Conservation of mass

The conservation of mass implies that the derivative of the total mass with respect to time is zero

$$\frac{D}{Dt}\int_{\mathrm{v}} \rho d\mathrm{v} = 0 \tag{A.24}$$

According to Leibniz's rule for differentiation under the integral sign, the expression Eq. A.24 can be easily solved once the domain of integration is constant. This can be accomplished using Eq. A.8

$$\frac{D}{Dt}\int_{\mathrm{v}} \rho d\mathrm{v} = \frac{D}{Dt}\int_{\mathrm{V}} \rho J d\mathrm{V} = \int_{\mathrm{V}} \frac{D}{Dt}(\rho J)\, d\mathrm{V} = \int_{\mathrm{V}} \left(\dot{\rho} J + \rho \dot{J}\right) d\mathrm{V}$$

Introducing Eq. A.15 yields

$$\int_{\mathrm{V}} \left(\dot{\rho} J + \rho \dot{J}\right) d\mathrm{V} = \int_{\mathrm{V}} \left(\dot{\rho} J + \rho J v_{k,k}\right) d\mathrm{V} = J \int_{\mathrm{V}} \left(\dot{\rho} + \rho v_{k,k}\right) d\mathrm{V} = 0$$

that must hold for any volume V, therefore

$$\dot{\rho} + \rho v_{k,k} = 0 \tag{A.25}$$

A.2.5 Conservation of linear momentum

The conservation of linear momentum can be written as

$$\frac{D}{Dt}\int_{\mathrm{v}} \rho \boldsymbol{v}\, d\mathrm{v} = \int_{\mathrm{v}} \left(\rho \boldsymbol{f} + \boldsymbol{F}^E\right) d\mathrm{v} + \int_{s} \boldsymbol{t}\, da \tag{A.26}$$

where $\boldsymbol{f}$ is a mechanical body force per unit mass and $\boldsymbol{t}$ is a mechanical force per unit area acting on the surface s of the body. It can be shown that

$$\frac{D}{Dt}\int_{\mathrm{v}} \rho v_i\, d\mathrm{v} = \int_{\mathrm{v}} \rho \frac{Dv_i}{Dt}\, d\mathrm{v} \tag{A.27}$$

Introducing the Cauchy stress tensor σ_{ji}, whose relation to the surface force per unit area $\boldsymbol{t}$ is $t_i = \sigma_{ji} n_j$, Eq. A.26 can be written as

$$\int_{\mathrm{v}} \rho \frac{Dv_i}{Dt}\, d\mathrm{v} = \int_{\mathrm{v}} \left(\rho f_i + F_i^E\right) d\mathrm{v} + \int_s \sigma_{ji} n_j da$$

Applying the divergence theorem and considering that the relation must hold for any volume v, the differential form of the conservation of the linear momentum is obtained

$$\rho \dot{v}_i = \rho f_i + F_i^E + \sigma_{ji,j} \tag{A.28}$$

A.2.6 Conservation of angular momentum

The conservation of angular momentum can be written as

$$\frac{D}{Dt} \int_{\mathrm{v}} \boldsymbol{y} \times \rho \boldsymbol{v}\, d\mathrm{v} = \int_{\mathrm{v}} \left(\boldsymbol{y} \times \left(\rho \boldsymbol{f} + \boldsymbol{F}^E\right) + \boldsymbol{C}^E\right) d\mathrm{v} + \int_s \boldsymbol{y} \times \boldsymbol{t}\, da \tag{A.29}$$

With the introduction of the permutation tensor ε_{ijk} the term on the left-hand side is

$$\frac{D}{Dt} \int_{\mathrm{v}} \rho \varepsilon_{ijk} y_j v_k\, d\mathrm{v} = \int_{\mathrm{v}} \rho \varepsilon_{ijk} y_j \dot{v}_k\, d\mathrm{v}$$

The contribution of the surface force $\boldsymbol{t}$ can be written as

$$\int_s \varepsilon_{ijk} y_j t_k\, da = \int_s \varepsilon_{ijk} y_j \sigma_{lk} n_l\, da = \int_{\mathrm{v}} \left(\varepsilon_{ijk} y_j \sigma_{lk}\right)_{,l} d\mathrm{v} =$$

$$= \int_{\mathrm{v}} \varepsilon_{ijk} \left(y_j \sigma_{lk}\right)_{,l} d\mathrm{v} = \int_{\mathrm{v}} \varepsilon_{ijk} \left(\delta_{jl} \sigma_{lk} + y_j \sigma_{lk,l}\right) d\mathrm{v} = \int_{\mathrm{v}} \varepsilon_{ijk} \left(\sigma_{jk} + y_j \sigma_{lk,l}\right) d\mathrm{v}$$

that can be substituted into Eq. A.29 yielding the index equation of conservation of angular momentum in the integral form

$$\int_{\mathrm{v}} \rho \varepsilon_{ijk} y_j \dot{v}_k\, d\mathrm{v} = \int_{\mathrm{v}} \left(\varepsilon_{ijk} y_j \left(\rho f_k + F_k^E\right) + C_i^E\right) d\mathrm{v} + \int_{\mathrm{v}} \varepsilon_{ijk} \left(\sigma_{jk} + y_j \sigma_{lk,l}\right) d\mathrm{v}$$

Some elements can be grouped and, considering the conservation of linear momentum (Eq. A.28), the following result is obtained

$$\int_{\mathrm{v}} \left(\varepsilon_{ijk} \sigma_{jk} + C_i^E\right) d\mathrm{v} = \int_{\mathrm{v}} \varepsilon_{ijk} y_j \left(\rho \dot{v}_k - \rho f_k - F_k^E - \sigma_{lk,l}\right) d\mathrm{v} = 0$$

Since the conservation of angular momentum must hold for any volume v

$$\varepsilon_{ijk} \sigma_{jk} + C_i^E = 0 \tag{A.30}$$

A.2.7 Conservation of energy

The conservation of energy is a scalar equation that can be formulated as

$$\frac{D}{Dt}\int_{\mathrm{v}} \rho\left(\frac{1}{2}\boldsymbol{v}\cdot\boldsymbol{v}+e\right) d\mathrm{v} = \int_{\mathrm{v}} \left(\left(\rho\boldsymbol{f}+\boldsymbol{F}^E\right)\cdot\boldsymbol{v}+w^E\right) d\mathrm{v} + \int_s \boldsymbol{t}\cdot\boldsymbol{v}\, da \tag{A.31}$$

The term on the left hand side can be written in index notation as

$$\int_{\mathrm{v}} \rho\left(v_i\dot{v}_i+\dot{e}\right) d\mathrm{v}$$

The contribution to energy balance due to the surface force $\boldsymbol{t}$ can be written in terms of the Cauchy stress tensor σ_{ji} as

$$\int_s t_k v_k\, da = \int_s \sigma_{lk} n_l v_k\, da = \int_v \left(\sigma_{lk}v_k\right)_{,l} d\mathrm{v} = \int_v \left(\sigma_{lk,l}v_k+\sigma_{lk}v_{k,l}\right) d\mathrm{v}$$

Relation Eq. A.28 can be substituted into Eq. A.31 yielding a more compact expression

$$\int_{\mathrm{v}} \left(\sigma_{lk}v_{k,l}+w^E-\rho\dot{e}\right) d\mathrm{v} = 0$$

that implies

$$\rho\dot{e} = \sigma_{lk}v_{k,l}+\rho E_i\dot{\pi}_i \tag{A.32}$$

A.2.8 Electrostatic stress tensor and total stress tensor

The electrostatic stress tensor σ_{ij}^E is defined as a function of $\boldsymbol{y}$ whose divergence yields the electric body force F_j^E. The relation between the two is

$$\sigma_{ij,i}^E = F_j^E \tag{A.33}$$

The choice of σ_{ij}^E is not unique; it is chosen to be

$$\sigma_{ij}^E = D_iE_j - \frac{1}{2}\varepsilon_0 E_kE_k\delta_{ij} \tag{A.34}$$

A total stress tensor τ_{ij} can be defined as the sum of σ_{ij} and σ_{ij}^E. This tensor can be decomposed into a symmetric tensor σ_{ij}^S and an anti-symmetric one σ_{ij}^M (the Maxwell stress tensor) such as

$$\tau_{ij} = \sigma_{ij} + \sigma^{E}_{ij} = \sigma^{S}_{ij} + \sigma^{M}_{ij} \tag{A.35}$$

where

$$\sigma^{S}_{ij} = \sigma_{ij} + P_i E_j \tag{A.36}$$

$$\sigma^{M}_{ij} = \varepsilon_0 \left(E_i E_j - \frac{1}{2} E_k E_k \delta_{ij} \right) \tag{A.37}$$

The definition of the electrostatic stress tensor σ^{E}_{ij} can be introduced in Eq. A.28 yielding

$$\rho \dot{v}_i = \rho f_i + \sigma^{E}_{ji,j} + \sigma_{ji,j}$$

$$\rho \dot{v}_i = \rho f_i + \left(\sigma^{E}_{ji} + \sigma_{ji} \right)_{,j}$$

$$\rho \dot{v}_i = \rho f_i + \tau_{ji,j}$$

The definition of the electric body couple $\boldsymbol{C}^{E}$ and of total stress tensor τ_{ij} can be introduced in Eq. A.30 yielding

$$\varepsilon_{ijk} \left(\sigma_{jk} + P_j E_k \right) = 0$$

$$\varepsilon_{ijk} \left(\sigma_{jk} + \sigma^{E}_{jk} \right) = 0$$

$$\varepsilon_{ijk} \tau_{jk} = 0$$

A.2.9 Free energy

The free energy ψ is a function of the internal energy per unit mass e, the electric field $\boldsymbol{E}$ and the polarization per unit mass $\boldsymbol{\pi}$

$$\psi = e - E_i \pi_i \tag{A.38}$$

The expression of the free energy can be substituted into Eq. A.32 yielding

$$\rho \dot{\psi} = \sigma_{lk} v_{k,l} - P_i \dot{E}_i$$

A.2.10 Material form of the balance laws

The expressions derived from the balance laws are

$$\begin{cases} D_{i,i} - \rho_e = 0 \\ \varepsilon_{ijk} E_{k,j} = 0 \\ \dot{\rho} + \rho v_{k,k} = 0 \\ \rho \dot{v}_i = \rho f_i + \tau_{ji,j} \\ \varepsilon_{ijk} \tau_{jk} = 0 \\ \rho \dot{\psi} = \sigma_{lk} v_{k,l} - P_i \dot{E}_i \end{cases} \tag{A.39}$$

As it can be noticed from the lower case indexes, these relations are function of $\boldsymbol{y}$ which refers to an unknown configuration. To be of practical use, relations Eq. A.39 need be expressed using the reference coordinates $\boldsymbol{X}$.

Gauss's law

$$\int_s D_i da_i = \int_{\mathrm{v}} \rho_e d\mathrm{v}$$

$$\int_S D_i J X_{L,i} dA_L = \int_{\mathrm{V}} \rho_e J d\mathrm{V}$$

$$\int_S D_i J X_{L,i} N_L dA = \int_{\mathrm{V}} \rho_e J d\mathrm{V}$$

$$\int_{\mathrm{V}} \left(D_i J X_{L,i}\right)_{,L} d\mathrm{V} = \int_{\mathrm{V}} \rho_e J d\mathrm{V}$$

Defining the material dielectric displacement $\mathcal{D}$ as

$$\mathcal{D}_L = D_i J X_{L,i} \qquad D_i = J^{-1} y_{i,L} \mathcal{D}_L$$

yields

$$\mathcal{D}_{L,L} = \rho_E$$

where ρ_E is the free charge per unit volume in the undeformed configuration.

Faraday's law

$$\int_l E_i dl_i = \int_L E_i y_{i,K} dL_K = \int_S \varepsilon_{IJK} \left(E_i y_{i,K}\right)_{,J} dA_I = 0$$

Defining the material electric field $\mathcal{E}$ as

$$\mathcal{E}_K = E_i y_{i,K} \qquad E_i = \mathcal{E}_K X_{K,i}$$

whose relation to the electric potential ϕ is

$$\mathcal{E}_K = -\phi_{,i} y_{i,K} = -\phi_{,K}$$

Faraday's law can be written

$$\int_S \varepsilon_{IJK} \mathcal{E}_{K,J} dA_I = 0$$

$$\varepsilon_{IJK} \mathcal{E}_{K,J} = 0$$

Conservation of mass

$$\int_{\mathrm{v}} \rho d\mathrm{v} = \int_{\mathrm{V}} \rho_0 d\mathrm{V}$$

$$\int_{\mathrm{V}} \rho J d\mathrm{V} = \int_{\mathrm{V}} \rho_0 d\mathrm{V}$$

$$\rho_0 = \rho J$$

where ρ_0 is the mass density in the reference state.

Conservation of linear momentum

$$\int_{\mathrm{v}} \rho \dot{v}_i d\mathrm{v} = \int_{\mathrm{v}} \rho f_i d\mathrm{v} + \int_s \tau_{ji} da$$

$$\int_{\mathrm{V}} \rho \dot{v}_i J d\mathrm{V} = \int_{\mathrm{V}} \rho f_i J d\mathrm{V} + \int_S \tau_{ji} J X_{L,j} dA_L$$

$$\int_{\mathrm{V}} \rho \dot{v}_i J d\mathrm{V} = \int_{\mathrm{V}} \rho f_i J d\mathrm{V} + \int_V \left(\tau_{ji} J X_{L,j}\right)_{,L} d\mathrm{V}$$

$$\rho_0 \dot{v}_i = \rho_0 f_i + \left(\tau_{ji} J X_{L,j}\right)_{,L}$$

Defining $K_{Lj} = \tau_{ji} J X_{L,j}$ yields

$$\rho_0 \dot{v}_i = \rho_0 f_i + K_{Lj,L}$$

Conservation of angular momentum

The total stress τ_{ji} can be expressed in terms of K_{Lj} by

$$\tau_{ji} = J^{-1} y_{i,L} K_{Lj}$$

Substituting it into the quation of conservation of angular momentum listed in Eq. A.39 gives

$$\varepsilon_{ijk}\tau_{jk} = \varepsilon_{kij} J^{-1} y_{i,L} K_{Lj} = 0$$

$$\varepsilon_{kij} y_{i,L} K_{Lj} = 0$$

Conservation of energy

The definition of a symmetric stress tensor T^S_{KL} and the material polarization vector $\mathcal{P}$

$$T^S_{KL} = J X_{K,k} X_{L,l} \sigma^S_{kl} \qquad \sigma^S_{kl} = J^{-1} y_{k,K} y_{l,L} T^S_{KL}$$

$$\mathcal{P}_K = J X_{K,k} P_k \qquad P_k = J^{-1} y_{k,K} \mathcal{P}_K$$

allows writing the conservation of energy with respect to the reference coordinates as

$$\rho_0 \dot{\psi} = \dot{S}_{KL} T^S_{KL} - \mathcal{P}_K \dot{\mathcal{E}}_L$$

The balance laws assume, in the material form, the followig expression

$$\begin{cases} \mathcal{D}_{L,L} = \rho_E \\ \varepsilon_{IJK} \mathcal{E}_{K,J} = 0 \\ \rho_0 = \rho J \\ \rho_0 \dot{v}_i = \rho_0 f_i + K_{Lj,L} \\ \varepsilon_{kij} y_{i,L} K_{Lj} = 0 \\ \rho_0 \dot{\psi} = \dot{S}_{KL} T^S_{KL} - \mathcal{P}_K \dot{\mathcal{E}}_L \end{cases}$$

that is expressed using the reference coordinates.

A.3 Constitutive equations

The conservation of energy equation gives hints on the dependency between the system's variables. Strain and electric field can be considered to be the independent variables. Free energy, stress and polarization can be expressed as function of these variables

$$\begin{aligned} \psi &= \psi\left(S_{KL}, \mathscr{E}_K\right) \\ T^S_{KL} &= T^S_{KL}\left(S_{KL}, \mathscr{E}_K\right) \\ \mathscr{P}_K &= \mathscr{P}_K\left(S_{KL}, \mathscr{E}_K\right) \end{aligned}$$

Based upon this assumption, the conservation of energy can be written as

$$\rho_0\left(\frac{\partial\psi}{\partial S_{KL}}\dot{S}_{KL} + \frac{\partial\psi}{\partial\mathscr{E}_L}\dot{\mathscr{E}}_L\right) = \dot{S}_{KL}T^S_{KL} - \mathscr{P}_K\dot{\mathscr{E}}_L$$

$$\left(T^S_{KL} - \rho_0\frac{\partial\psi}{\partial S_{KL}}\right)\dot{S}_{KL} = \left(\rho_0\frac{\partial\psi}{\partial\mathscr{E}_L} + \mathscr{P}_K\right)\dot{\mathscr{E}}_L$$

For these equations hold for any $\dot{S}_{KL}, \dot{\mathscr{E}}_L$ the following relations must be verified

$$T^S_{KL} = \rho_0\frac{\partial\psi}{\partial S_{KL}}$$

$$\mathscr{P}_K = -\rho_0\frac{\partial\psi}{\partial\mathscr{E}_L}$$

The explicit expression of the free energy ψ can be found and it is dependent on twelve tensors, ranking from second to fourth order.

A.4 Initial-boundary-value problem

The balance equation must hold for any part of the body and at any time. Faraday's law is automatically satisfied since the electric field can be computed from the divergence of a potential ϕ. The conservation of angular momentum is always verified since the total stress tensor τ_{ij} is symmetric. The constitutive equations are derived from the conservation of energy, therefore it already taken into account. The present mass density ρ can be calculated once the deformed configuration is known. The only equations left are the Gauss's law and the conservation of linear momentum

$$\begin{cases} \mathcal{D}_{L,L} = \rho_E \\ \rho_0 \dot{v}_i = \rho_0 f_i + K_{Lj,L} \end{cases}$$

The free energy formulation, along with the balance equations, allow writing the system of equations as a function of four unknowns $y_i\left(X_L, t\right)$ and $\phi\left(X_L, t\right)$.

Appendix B

Linear Piezoelectricity

The hypothesis upon which the theory of linear piezoelectricity is based on are that the displacement vector is small for any point of the electroelastic body, the electric field intensity is small, and that the electric field variations are much faster than the body dynamics.

B.1 Constitutive equations

The constitutive equations are nine independent equations that relate strain S, stress T, electric field E, and electric displacement D. They usually are expressed as

$$\begin{aligned} T_{ij} &= c^E_{ijkl} S_{kl} - e_{ijk} E_k \\ D_i &= e_{ijk} S_{kl} + \varepsilon^S_{ij} E_k \end{aligned} \tag{B.1}$$

and they describe the material's behaviour under static conditions.

B.2 Dynamic equations

The dynamics of a continuum of piezoelectric material can be described by a set of four differential equation in its displacement from reference configuration $\boldsymbol{u}$ and the electric potential φ

$$\begin{cases} c^E_{ijkl} u_{k,li} + e_{kij} \varphi_{,ki} = \rho \ddot{u}_j \\ e_{ijk} u_{i,jk} - \varepsilon^S_{ij} \varphi_{,ij} = 0 \end{cases} \tag{B.2}$$

where $\ddot{u}$ is the second derivative of u with respect to time.

ij or kl	p or q
11	1
22	2
33	3
23, 32	4
13, 31	5
12, 21	6

Table B.1: Compact index notation

B.3 Compressed matrix representation

The symmetry properties of the material constants, of the stress tensor, and of the strain tensor allow writing the constitutive equations in a more compact form. The stress and strain tensors have six independent components, out of the nine that constitute each of them. The number of independent coefficients of material constants is 36, 18, and 6 for respectively c^E_{ijkl}, e_{kij}, and ε^S_{ij}.

Introducing a simple correspondence between indexes (see Tab B.1)

$$T_{ij} \rightarrow T_p, \qquad S_{ij} \rightarrow S_q$$

$$c_{ijkl} \rightarrow c_{pq}, \qquad e_{ikl} \rightarrow e_{iq}$$

the constitutive equations can be written in matrix-vector form. This simplification is in accordance with the IEEE standard 176-1987 [1]. The stress tensor can be written in vector form as

$$\{T\} = \{T_{11}\ T_{22}\ T_{33}\ T_{23}\ T_{13}\ T_{12}\}^{\mathrm{T}}$$

while the strain vector is defined as

$$\{S\} = \{S_{11}\ S_{22}\ S_{33}\ 2S_{23}\ 2S_{13}\ 2S_{12}\}^{\mathrm{T}}$$

where the elements of the vector S are

$$
\begin{aligned}
S_{11} &= \tfrac{\partial u_1}{x_1} \\
S_{22} &= \tfrac{\partial u_2}{x_2} \\
S_{33} &= \tfrac{\partial u_3}{x_3} \\
S_{23} &= \tfrac{\partial u_2}{x_3} \\
S_{13} &= \tfrac{\partial u_1}{x_3} \\
S_{12} &= \tfrac{\partial u_1}{x_2}
\end{aligned}
$$

The matrix form of the constitutive equations (see Eq. B.1) is

$$
\begin{cases}
T_p = c^E_{pq} S_q - e_{kp} E_k \\
D_i = e_{iq} S_q + \varepsilon^S_{ik} E_k
\end{cases}
\tag{B.3}
$$

B.4 Relation between material constants

The following relations between material constants hold

$$
\begin{array}{ll}
c^E_{pr} s^E_{qr} = \delta_{pq} & c^D_{pr} s^S_{qr} = \delta_{pq} \\
\beta^S_{pr} \varepsilon^S_{qr} = \delta_{pq} & \beta^T_{pr} \varepsilon^T_{qr} = \delta_{pq} \\
c^D_{pq} = c^E_{pq} + e_{rp} h_{rq} & s^D_{pq} = s^E_{pq} + d_{rp} g_{rq} \\
\varepsilon^T_{pq} = \varepsilon^S_{pq} + d_{pr} e_{qr} & \beta^T_{pq} = \beta^S_{pq} - g_{pr} h_{qr} \\
e_{pq} = d_{pr} c^E_{rq} & d_{pq} = \varepsilon^T_{pr} g^E_{rq} \\
g_{pq} = \beta^T_{pr} d_{rq} & h_{pq} = g_{pr} c^D_{rq}
\end{array}
\tag{B.4}
$$

B.5 The elasto-piezo-dielectric matrix

Depending on crystal structure, some elements of c_{pq}, e_{iq}, and ε_{ik} are zero. The elastic-piezo-dielectric matrix helps finding out which entries are null. Most piezoelectric materials present a perovskite structure, a crystal structure that belongs to the `4mm` point group. Figure B.1 shows the symmetric elasto-piezo-dielectric matrix for the `4mm` point group. A connecting line between elements means equality.

The non-zero coefficients for a perovskite-like piezoelectric material are c_{11}, c_{12}, c_{13}, c_{33}, c_{44}, e_{31}, e, e_{15}, ε_{11}, and ε_{33}. The element c_{66} is equal to $\frac{1}{2}(c_{11} - c_{12})$ [34].

These constants can be calculated from the more readily available values of s_{pq} and d_{iq}. The following relations hold

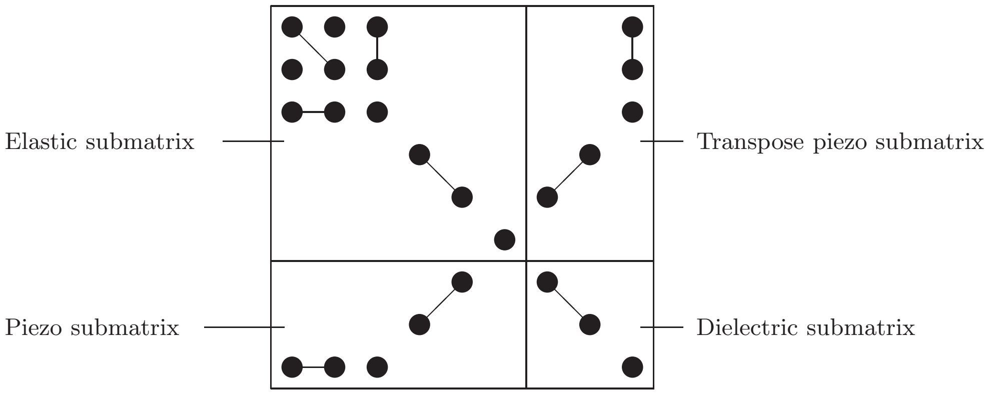
Elastic submatrix
Transpose piezo submatrix
Piezo submatrix
Dielectric submatrix

Figure B.1: The `4mm` elasto-piezo-dielectric matrix non-zero entries

$$\begin{cases} c_{11} = (s_{11}^{E} s_{33} - s_{13}^{2})/(s_{33}s_{11}^{2} - 2s_{13}^{2}s_{11} - s_{12}^{2}s_{33} + 2s_{13}^{2}s_{12}) \\ c_{12} = -(s_{12}s_{33} - s_{13}^{2})/(s_{33}s_{11}^{2} - 2s_{13}^{2}s_{11} - s_{12}^{2}s_{33} + 2s_{13}^{2}s_{12}) \\ c_{13} = -s_{13}/(s_{11}s_{33} - 2s_{13}^{2} + s_{12}s_{33}) \\ c_{33} = (s_{11} + s_{12})/(s_{11}s_{33} - 2s_{13}^{2} + s_{12}s_{33}) \\ c_{44} = 1/s_{44} \\ c_{66} = 1/s_{66} \\ e_{15} = d_{15}c_{44} \\ e_{31} = d_{31}c_{11} + d_{32}c_{12} + d_{33}c_{13} \\ e_{33} = (d_{31} + d_{32})c_{13} + d_{33}c_{33} \end{cases} \tag{B.5}$$

for perovskite-like materials. The superscript E has been omitted in the previous equations for sake of clarity.

B.6 Constitutive and dynamic equations

Since the elasto-piezo-dielectric matrix has many null entries, the constitutive and dynamic equation can be written explicitly in a rather compact form (Eq. B.6 and Eq. B.7).

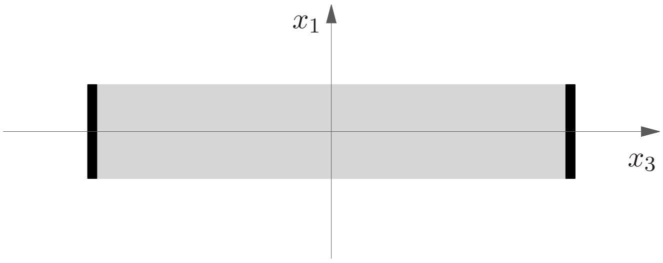

Figure B.2: Rod model

$$\begin{cases}
T_1 = c^E_{11}S_1 + c^E_{12}S_2 + c^E_{13}S_3 - e_{31}E_3 \\
T_2 = c^E_{12}S_1 + c^E_{11}S_2 + c^E_{13}S_3 - e_{31}E_3 \\
T_3 = c^E_{13}(S_1 + S_2) + c^E S_3 - e_{33}E_3 \\
T_4 = c^E_{44}S_4 + e_{15}E_2 \\
T_5 = c^E_{44}S_5 + e_{15}E_1 \\
T_6 = c^E_{66}S_6 \\
D_1 = e_{15}S_5 + \varepsilon^S_{11}E_1 \\
D_2 = e_{15}S_4 + \varepsilon^S_{11}E_2 \\
D_3 = e_{31}(S_1 + S_2) + e_{33}S_3 + \varepsilon^S_{33}E_3
\end{cases} \tag{B.6}$$

$$\begin{cases}
c^E_{11}u_{1,11} + (c^E_{12} + c^E_{66})u_{2,12} + (c^E_{13} + c^E_{44})u_{3,13} + c^E_{66}u_{1,22} + c^E_{44}u_{1,33} + \\
\quad +(e_{31} + e_{15})\varphi_{,13} = \rho\ddot{u}_1 \\
c^E_{66}u_{2,11} + (c^E_{12} + c^E_{66})u_{1,12} + c^E_{11}u_{2,22} + (c^E_{13} + c^E_{44})u_{3,23} + c^E_{44}u_{2,33} + \\
\quad +(e_{31} + e_{15})\varphi_{,23} = \rho\ddot{u}_2 \\
c^E_{44}u_{3,11} + (c^E_{44} + c^E_{13})u_{1,31} + c^E_{44}u_{3,22} + (c^E_{13} + c^E_{44})u_{2,23} + \\
\quad +c^E_{33}u_{3,33} + e_{15}(\varphi_{,11} + \varphi_{,22}) + e_{33}\varphi_{,33} = \rho\ddot{u}_3 \\
e_{15}(u_{3,11} + u_{3,22}) + (e_{15} + e_{31})u_{1,13} + (e_{15} + e_{31})u_{2,32} + eu_{3,33} - \\
\quad -e_{11}(\varphi_{,11} + \varphi_{,22}) - \varepsilon^S_{33}\varphi_{,33} = 0
\end{cases} \tag{B.7}$$

B.7 Slender rod in axial mode

The rod is electroded on the end faces while the lateral surface is completely free and unloaded. The rod might be mechanically loaded along the poled axis, that is axis 3 (see Fig. B.2).

Some simplifications can be introduced, that the only non-zero stress is $T_3 = f$. Furthermore, the electric field's only component is E_3. Given this set of hypothesis, the most appropriate constitutive equations are

$$\begin{cases} S_p = s^E_{pq} T_q + d_{kp} E_k \\ D_i = d_{iq} T_q + \varepsilon^T_{ik} E_k \end{cases} \tag{B.8}$$

The constitutive equations can be written taking into account the simplifications previously made, yielding

$$\begin{cases} S_1 = s^E_{13} T_3 + d_{31} E_3 \\ S_2 = s^E_{13} T_3 + d_{31} E_3 \\ S_3 = s^E_{33} T_3 + d_{33} E_3 \\ D_3 = d_{33} T_3 + \varepsilon^T_{33} E_3 \end{cases} \tag{B.9}$$

B.7.1 Electromechanical coupling coefficient

The piezoelectric effect allows converting mechanical energy into electrical energy and vice versa. Through the direct piezoelectric effect mechanical energy is converted into electrical one, and the opposite happens in case of the converse piezoelectric effect.

Energy can be accumulated in a piezoelectric solid either as mechanical or electrical energy. It can be introduced indifferently by mechanical or electric loading. The electromechanical coupling coefficient, usually labeled k, measures the ratio of stored mechanical/electrical energy over the input electrical/mechanical one. Subscript and superscript specify the loading conditions and the piezoelectric mode. The value of the electromechanical coupling coefficient depends on the directions upon which forces and electric field are applied. Often mechanical coupling coefficients are expressed relative to the one calculated for a slender rod.

Direct effect

Considering a force F applied to the end faces so that a stress f is induced, the work done is different whether the electrodes are shorted or not (see Fig. B.3). In case the electrodes are shorted, the electric potential is equal on the end faces and thus the electric field E_3 is zero. The following equations hold:

$$\begin{cases} S_1 = s^E_{13} f \\ S_2 = s^E_{13} f \\ S_3 = s^E_{33} f \\ D_3 = d_{33} f \end{cases}$$

The work done at constant electric field per unit volume can be calculated as

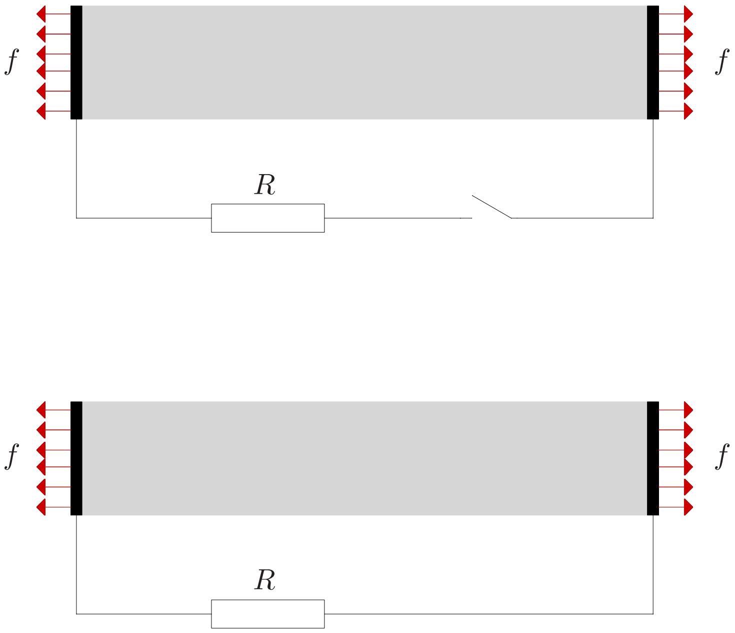

Figure B.3: Mechanically loaded piezoelectric rod

$$w_m^E = \frac{1}{2} s_{33}^E f^2 \tag{B.10}$$

and there is no electric energy accumulated into the material.

When the electrodes are open, there is no net charge on the electrodes, thus $D_3 = 0$ at both ends of the rod. The constitutive equations can be written now as

$$\begin{cases} S_1 = \left(s_{13}^E - \frac{d_{13} d_{33}}{\varepsilon_{33}^T} \right) f \\ S_2 = \left(s_{13}^E - \frac{d_{13} d_{33}}{\varepsilon_{33}^T} \right) f \\ S_3 = \left(s_{33}^E - \frac{d_{33}^2}{\varepsilon_{33}^T} \right) f \\ E_3 = -\frac{d_{33}}{\varepsilon_{33}^T} f \end{cases}$$

The mechanical work done at constant electric displacement per unit volume can be calculated as

$$w_m^D = \frac{1}{2} \left(s_{33}^E - \frac{d_{33}^2}{\varepsilon_{33}^T} \right) f^2 \tag{B.11}$$

while the electric energy stored per unit volume is equal to

$$w_e = \frac{1}{2} \frac{d_{33}^2}{\varepsilon_{33}^T} f^2 \tag{B.12}$$

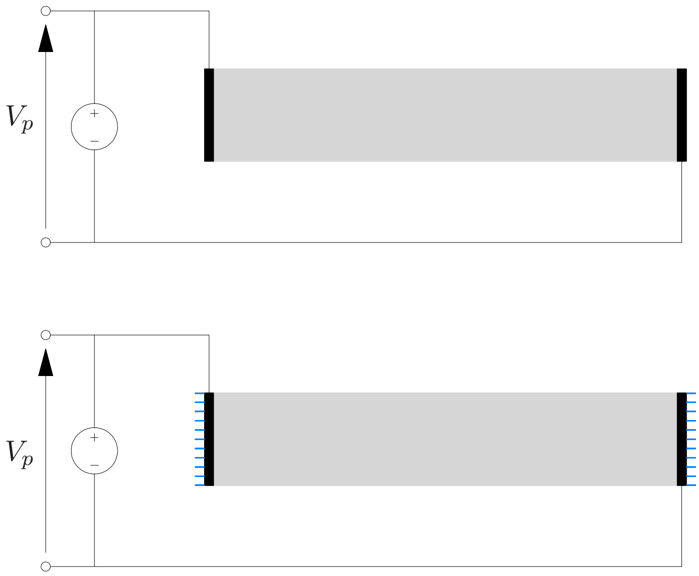

Figure B.4: Electrically loaded piezoelectric rod

It is worth noticing that the mechanical work done is larger at constant electric field; at constant electric displacement part of the input energy is converted into electrical one via the direct piezoelectric effect. Indeed:

$$w_m^E - w_m^D = w_e$$

The ratio between the stored electrical energy and the input mechanical energy yields the electromechanical coupling coefficient k_{33}^{l}, that is

$$k_{33}^{\mathrm{l}} = \sqrt{\frac{w_e}{w_m^E}} = \frac{d_{33}}{\sqrt{s_{33}^E \varepsilon_{33}^T}} \tag{B.13}$$

Converse effect

The deformation of the rod can be induced by an electric field as well. When the electrodes are connected to a voltage source and there is no mechanical force acting on the rod, the induced deformation can be easily calculated. Indeed, the stress T_3 is zero and the electric field E_3 is equal to $-V_p/l$, being l the rod length. The deformation is thus

$$\begin{cases} S_1 = -d_{31}\frac{V_p}{l} \\ S_2 = -d_{31}\frac{V_p}{l} \\ S_3 = -d_{33}\frac{V_p}{l} \\ D_3 = -\varepsilon_{33}^T\frac{V_p}{l} \end{cases}$$

and the electric energy per unit volume stored is

$$w_e^T = \frac{1}{2}\frac{\varepsilon_{33}^T}{l^2}{V_p}^2 \tag{B.14}$$

In case the rod is constrained so that no deformation S_3 is allowed, the constitutive equations are

$$\begin{cases} S_1 = -\left(\frac{d_{33}s_{13}^E}{s_{33}^E} + d_{31}\right)\frac{V_p}{l} \\ S_2 = -\left(\frac{d_{33}s_{13}^E}{s_{33}^E} + d_{31}\right)\frac{V_p}{l} \\ T_3 = \frac{d_{33}}{s_{33}^E}\frac{V_p}{l} \\ D_3 = \left(\frac{d_{33}^2}{s_{33}^E} - \varepsilon_{33}^T\right)\frac{V_p}{l} \end{cases}$$

The electric energy stored per unit volume can be calculated as

$$w_e^S = \frac{1}{2Al}V_p\int D_3 dA = \frac{1}{2l^2}\left(\frac{d_{33}^2}{s_{33}^E} - \varepsilon_{33}^T\right){V_p}^2 \tag{B.15}$$

where A is the area of rod cross-section. The mechanical work that can be done releasing the constraints on the end faces is

$$w_m = \frac{1}{2}\frac{d_{33}^2}{s_{33}^E}\frac{{V_p}^2}{l^2} \tag{B.16}$$

It is worth noticing that

$$w_e^S - w_e^T = w_m$$

The ratio between the stored mechanical energy and the input electrical energy yields the electromechanical coupling coefficient

$$k_{33}^1 = \sqrt{\frac{w_m}{w^T}} = \frac{d_{33}}{\sqrt{s_{33}^E\varepsilon_{33}^T}} \tag{B.17}$$

As anticipated, the ratio between stored and input energy does not depend on the type of input energy (see Eq. B.13 and Eq. B.17).

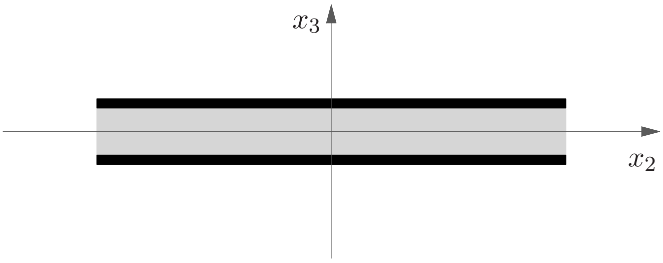

Figure B.5: Thin plate model

B.8 Thin plate in stretch mode

A thin plate of piezoelectric material shall present electrodes on the upper and lower faces, perpendicular to the direction 3 (see Fig. B.5). It is assumed that the only non-zero deformation is S_3 and the electric field lines are directed along the axis 3.

The constitutive and dynamic equations Eq. B.1 and Eq. B.2 can be simplified respectively as

$$\begin{cases} T_1 = c_{13}^E S_3 - e_{31} E_3 \\ T_2 = c_{13}^E S_3 - e_{31} E_3 \\ T_3 = c_{33}^E S_3 - e_{33} E_3 \\ D_3 = e_{33} S_3 + \varepsilon_{33}^S E_3 \end{cases} \tag{B.18}$$

$$\begin{cases} c_{33}^E u_{3,33} + e_{33} \varphi_{,33} = \rho \ddot{u}_3 \\ e_{33} u_{3,33} - \varepsilon_{33}^S \varphi_{,33} = 0 \end{cases} \tag{B.19}$$

B.8.1 Coupling coefficient of a thin plate

The electromechanical coupling coefficient for a thin plate in stretch mode is labeled k_{33}^{t}. As for the piezoelectric rod model, the direct and converse effects shall be analysed.

Direct effect

Considering a force F that induces a constant stress f on the plate upper and lower surfaces, the conversion of energy will be analysed (see Fig. B.6). When the electrodes are shorted they are at the same electric potential and thus the electric field E_3 is zero. The constitutive equations Eq. B.18 can be written as

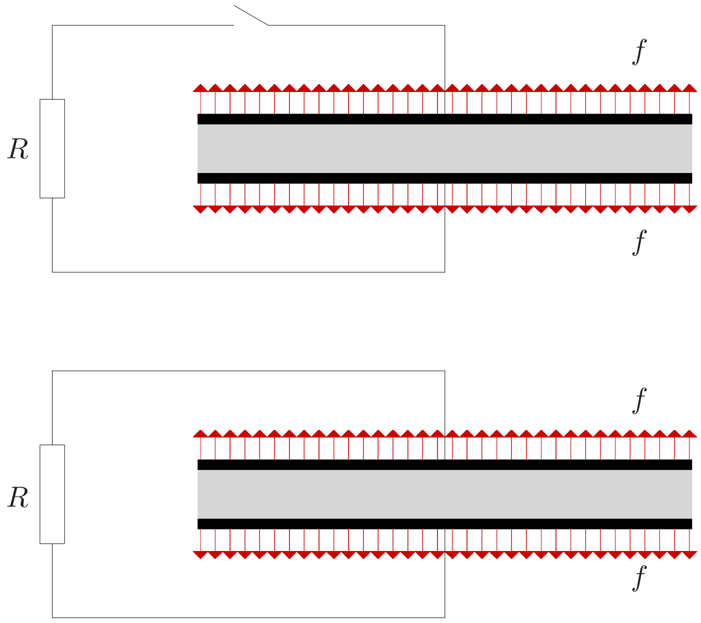

Figure B.6: Mechanically loaded piezoelectric thin plate

$$\begin{cases} T_1 = c_{13}^E S_3 \\ T_2 = c_{13}^E S_3 \\ f = c_{33}^E S_3 \\ D_3 = e_{33} S_3 \end{cases}$$

which can be easily solved as

$$\begin{cases} T_1 = \frac{c_{13}^E}{c_{33}^E} f \\ T_2 = \frac{c_{13}^E}{c_{33}^E} f \\ S_3 = \frac{1}{c_{33}^E} f \\ D_3 = \frac{e_{33}}{c_{33}^E} f \end{cases}$$

The mechanical work done at constant electric field per unit volume is

$$w_m^E = \frac{1}{2c_{33}^E} f^2 \tag{B.20}$$

When the electrodes are open, the net charge must be zero and therefore the electric displacement D_3 is zero. Given a constant stress f along the axis 3, the following equations hold

$$\begin{cases} T_1 = c_{13}^E S_3 - e_{13} E_3 \\ T_2 = c_{13}^E S_3 - e_{13} E_3 \\ p = c_{33}^E S_3 - e_{33} E_3 \\ 0 = e_{33} S_3 + \varepsilon_{33}^S E_3 \end{cases}$$

which find a solution in

$$\begin{cases} T_1 = \frac{e_{33}}{e_{33}^2 + \varepsilon_{33}^S c_{33}^E} \left(\varepsilon_{33}^S c_{13}^E + e_{33} e_{13} \right) f \\ T_2 = \frac{e_{33}}{e_{33}^2 + \varepsilon_{33}^S c_{33}^E} \left(\varepsilon_{33}^S c_{13}^E + e_{33} e_{13} \right) f \\ S_3 = \frac{\varepsilon_{33}^S}{e_{33}^2 + \varepsilon_{33}^S c_{33}^E} f \\ E_3 = -\frac{e_{33}}{e_{33}^2 + \varepsilon_{33}^S c_{33}^E} f \end{cases}$$

The mechanical work done at constant electric displacement per unit volume is

$$w_m^D = \frac{1}{2} \frac{\varepsilon_{33}^S}{e_{33}^2 + \varepsilon_{33}^S c_{33}^E} f^2 \tag{B.21}$$

and the electromechanical coupling coefficient k_{33}^{t} is

$$k_{33}^{\mathrm{t}} = \sqrt{\frac{w_m^E - w_m^D}{w_m^E}} = \sqrt{1 - \frac{\varepsilon_{33}^S c_{33}^E}{e_{33}^2 + \varepsilon_{33}^S c_{33}^E}} = \frac{e_{33}}{\sqrt{\varepsilon_{33}^S c_{33}^D}} \tag{B.22}$$

where some relations of Eq. B.4 between constants have been used. The available electrical energy that can be used connecting the electrodes to an electric load can be easily calculated as

$$w_e = \frac{1}{2} \frac{e_{33}^2}{c_{33}^E \left(e_{33}^2 + \varepsilon_{33}^S c_{33}^E \right)} f^2 \tag{B.23}$$

It is worth noticing that

$$w_e = w_m^T - w_m^S$$

Converse effect

Considering the thin plate mechanically unloaded and with the electrodes connected to a voltage source V_p (see Fig. B.7), the piezoelectric plate is permeated by an electric field whose intensity is equal to V_p/t. The constitutive equations can be written as

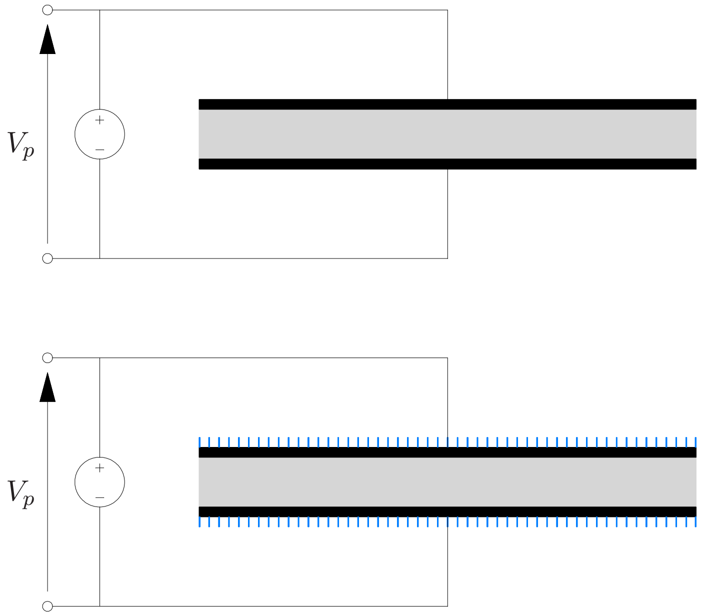

Figure B.7: Electrically loaded piezoelectric thin plate

$$\begin{cases} T_1 = \left(-c_{13}^E \frac{e_{33}}{c_{33}^E} + e_{13}\right) \frac{V_p}{t} \\ T_2 = \left(-c_{13}^E \frac{e_{33}}{c_{33}^E} + e_{13}\right) \frac{V_p}{t} \\ S_3 = -\frac{e_{33}}{c_{33}^E} \frac{V_p}{t} \\ D_3 = -\left(\frac{e_{33}^2}{c_{33}^E} + \varepsilon_{33}^S\right) \frac{V_p}{t} \end{cases} \tag{B.24}$$

The stored electric energy at constant stress per unit volume can be calculated as

$$w_e^T = \frac{1}{2}\left(\frac{e_{33}^2}{c_{33}^E} + \varepsilon_{33}^S\right) \frac{{V_p}^2}{t^2} \tag{B.25}$$

Should the plate be constrained, so that no deformation is induced, the constitutive equations are

$$\begin{cases} T_1 = -e_{13} \frac{V_p}{t} \\ T_2 = -e_{13} \frac{V_p}{t} \\ T_3 = -e_{33} \frac{V_p}{t} \\ D_3 = \varepsilon_{33}^S \frac{V_p}{t} \end{cases}$$

and the stored electrical energy at constant strain per unit volume is

$$w_e^S = \frac{1}{2} \varepsilon_{33}^S \frac{{V_p}^2}{t^2} \tag{B.26}$$

The available mechanical energy that can be used releasing the constraint can be easily computed as

$$w_m = \frac{1}{2}\frac{e_{33}^2}{c_{33}^E}\frac{{V_p}^2}{t^2} \tag{B.27}$$

It is worth noticing that

$$w_m = w_e^T - w_e^S$$

The electromechanical coupling coefficient can be calculated as

$$k_{33}^{\mathrm{t}} = \sqrt{\frac{w_e^T - w_e^S}{w_e^T}} = \sqrt{1 - \frac{\varepsilon_{33}^S c_{33}^E}{e_{33}^2 + \varepsilon_{33}^S c_{33}^E}} = \frac{e_{33}}{\sqrt{\varepsilon_{33}^S c_{33}^D}} \tag{B.28}$$

and it has the same value as the one calculated in Eq. B.22.

Appendix C

Piezoelectric ceramics

The following Tab. C.1 reports all the material characteristics of the piezoelectric materials manufactured by Physik Instrumente. All the materials share the following properties: specific thermal capacity c_h (350 J kg^{-1}K^{-1}), specific thermal conductivity c_t (1.1 W m^{-1}K^{-1}), Poisson's coefficient ν (0.34), thermal expansion coefficient in the polarization direction and perpendicular respectively $\alpha_{\|}$ ($-4 \div -6 \cdot 10^{-6}$ K^{-1}) and $\alpha_{\perp}$ ($4 \div 8 \cdot 10^{-6}$ K^{-1}), and the maximum compressive stress R (>600 MPa).

The *soft* piezoelectric materials are those that show stronger piezoelectric effect, i.e. larger deformations are induced by an electric field (especially in the 33 mode) with respect to the *hard* piezoelectric materials (see for comparison the d_{33} coefficient values in Tab. C.1). On the contrary soft piezoelectric materials present a very large hysteresis of the strain - electric field curve, thus they are not particularly suited for deviced working at very high frequencies. Indeed hysteresis causes large energy losses. More performing in this respect are the hard piezoelectric materials; quantitative comparison can be made by looking up the mechanical quality factor: the larger it is the smaller the hysteresis losses.

Material type				**151**	**255**	**155**	**153**	**152**	**181**	**141**	**241**	**300**	**110**
				(soft piezoelectric)					(hard piezoelectric)				(lead-free)
Physical and dielectric properties													
Density		ρ	g/cm^3	7.8	7.8	7.8	7.6	7.7	7.8	7.8	7.8	7.8	5.5
Curie temperature		T_c	°C	250	350	345	185	340	330	295	270	370	150
Relative permittivity	∥ polarity	$\varepsilon_{33}^T/\varepsilon_0$	-	2400	1750	1450	4200	1350	1200	1250	1650	1050	950
	⊥ polarity	$\varepsilon_{11}^T/\varepsilon_0$	-	1980	1650	1400			1500	1500	1550	950	
Dielectric loss factor		$\tan\delta$	10^{-3}	20	20	20	30	15	3	5	5	3	15
Electromechanical properties													
Coupling factors		k_p	-	0.62	0.62	0.62	0.62	0.48	0.56	0.55	0.50	0.48	0.30
		k_t	-	0.53	0.47	0.48			0.46	0.48	0.46	0.43	0.42
		k_{31}	-	0.38	0.35	0.35			0.32	0.31	0.32	0.25	0.18
		k_{33}	-	0.69	0.69	0.69		0.58	0.66	0.66	0.64	0.46	
		k_{15}	-		0.66				0.63	0.67	0.63	0.32	
Piezoelectric charge constants		d_{31}	10^{-12} C/N	-210	-180	-165			-120	-140	-130	-80	-50
		d_{33}		500	400	360	600	300	265	310	290	155	120
		d_{15}			550				475	475	265	155	
Piezoelectric voltage constants		g_{31}	10^{-3} V m/N	-11.5	-11.3	-12.9			-11.2	-13.1	-9.8	-9.5	
		g_{33}		22	25	27	16	25	25	29	21	16	-11.9
Acousto-mechanical properties													
Frequency constants		N_p	Hz m	1950	2000	1960	1960	2250	2270	2250	2190	2350	3150
		N_1		1500	1420	1500			1640	1610	1590	1700	2300
		N_3		1750		1780			2010	1925	1550	1700	2500
		N_t		1950	2000	1990	1960	1920	2110	2060	2140	2100	
Elastic constants (compliance)		s_{11}^E	10^{-12} m^2/N	15	16.1	15.6			11.8	12.4	12.6	11.1	
		s_{33}^E		19	20.7	19.7			14.2	13	14.3	11.8	
Elastic constants (stiffness)		c_{33}^D	10^{10} N/m^2	10		11.1			16.6	15.8	13.8	16.4	
Mechanical quality factor		Q_m	-	100	80	80	50	100	2000	1500	1200	1400	250
Temperature stability													
Temperature stability of ε_{33}^T in the range $[-20\ °\mathrm{C}, 150\ °\mathrm{C}]$		$\Delta\varepsilon_{33}^T/\varepsilon_{33}^T$	10^{-3}/K	6	4	6	5	2	3	5		2	
Aging stability relative change of the parameter													
Relative dielectric constant		c_ε	%		-1	-2				-4			-5
Coupling factor		c_K			-1	-2				-2			-8

Table C.1: PZT materials characterics - Physik Instrumente®

Bibliography

[1] IEEE Std 176-1987 Standard on Piezoelectricity, 1988.

[2] Christian Belly, Frank Claeyssen, Ronan Le Letty, and Thomas Porchez. Benefits from amplification of piezo actuation in inertial stepping motors and application for high performance linear micro motors. In *Proceedings of ACTUATOR10 - International Conference and Exhibition on New Aactuators and Drive Systems*, pages 198 – 201, Bremen, Germany, 2010.

[3] Dan Borza, Didier Lemosse, and Emmanuel Pagnacco. Full-field experimental-numerical study of mechanical static strain and stress in piezoelectric multilayer compression-type actuators. *Composite Structures*, 82(1):36 – 49, 2008.

[4] M. Brunot. Structures piézoélectriques à couches multiples. *Annales des Télécommunications*, 31:45–73, February 1976.

[5] Christopher Cadou and Bing Zhang. Performance modeling of a piezo-hydraulic actuator. *Journal of Intelligent Material Systems and Structures*, 14(3):149 – 160, 2003.

[6] Jared Diamond. *Guns, Germs, and Steel. The Fates of Human Societies.* W.W. Norton and Company, 1997.

[7] `http://www.dytran.com`, 2010.

[8] Eric Flint, Chen Liang, and Craig A. Rogers. Electromechanical analysis of piezoelectric stack active member power consumption. *Journal of Intelligent Material Systems and Structures*, 6(1):117 – 124, 1995.

[9] `http://www.fluke.com`, 2010.

[10] V. Giurgiutiu, Z. Chaudhry, and C.A. Rogers. The Analysis of Power Delivery Capability of Induced Strain Actuators for Dynamic Applications. In *Proceeding of the Scond International Conference on Intelligent Materials*, 1994.

[11] Michael Goldfarb and Nikola Celanovic. Modeling piezoelectric stack actuators for control of micromanipulation. *IEEE Control Systems Magazine*, 17(3):69 – 79, 1997.

[12] X. Gong and Z. Suo. Reliability of ceramic multilayer actuators: a nonlinear finite element simulation. *Journal of the Mechanics and Physics of Solids*, 44(5):751 – 769, 1996.

[13] `http://ieee.org`, 2010.

[14] C. Liang, F.P. Sun, and C.A. Rogers. Coupled Electro-Mechanical Analysis of Adaptive Material systems - Determination of the Actuator Power Consumption and System Energy Transfer. *Journal of Intelligent Material Systems and Structures*, 5(1):12 – 20, 1994.

[15] C. Liang, F.P. Sun, and C.A. Rogers. Impedance method for dynamic analysis of active material systems. *Journal of Vibration and Acoustics, Transactions of the ASME*, 116(1):120 – 128, 1994.

[16] Dirk Mehlfeldt, Hartmut Weckenmann, and Gunter Stohr. Modeling of piezoelectrically actuated fuel injectors. *Mechatronics*, 18(5-6):264 – 272, 2008.

[17] `http://www.micro-epsilon.com`, 2010.

[18] A.R. Mitchell and D.F. Griffiths. *The Finite Difference Method in Partial Differential Equations*. John Wiley & Sons, 1980.

[19] E. H. Moore. On the reciprocal of the general algebraic matrix. *Bulletin of the American Mathematical Society 26*, 1920.

[20] Kim Tiow Ooi. Simulation of a piezo-compressor. *Applied Thermal Engineering*, 24(4):549 – 562, 2004.

[21] Roger Penrose. A generalized inverse for matrices. *Proceedings of the Cambridge Philosophical Society 51*, 1955.

[22] `http://www.physikinstrumente.com`, 2010.

[23] `http://www.piezomechanik.com`, 2010.

[24] G. Pinte, S. Devos, B. Stallaert, W. Symens, J. Swevers, and P. Sas. A piezo-based bearing for the active structural acoustic control of rotating machinery. *Journal of Sound and Vibration*, 329(9):1235 – 1253, 2010.

[25] Radu Pomirleanu and Victor Giurgiutiu. Full-stroke Static and Dynamic Analysis of High-power Piezoelectric Actuators. *Journal of Intelligent Material Systems and Structures*, 13, 2002.

[26] P. Righettini, B. Zappa, R. Strada, and M. Forlani. Development of a high precision high stroke positioning system. In *Proceedings of the 10th International Workshop on Research and Education in Mechatronics REM 2009*, Glasgow, UK, 2009.

[27] `http://www.ti.com`, 2010.

[28] K. Uchino, J.H. Zheng, Y.H. Chen, X.H. Du, J. Ryu, Y. Gao, S. Ural, S. Priya, and S. Hirose. Loss mechanisms and high power piezoelectrics. *Journal of Materials Science*, 41(1):217 – 228, 2006.

[29] Kenji Uchino. *Piezoelectric Actuators and Ultrasonic Motors*. Kluwer Academic Publishers, 1997.

[30] Kenji Uchino. Piezoelectric actuators 2006 - Expansion from IT/robotics to ecological/energy applications. *Journal of Electroceramics*, 2008.

[31] Kenji Uchino and Jayne R. Giniewicz. *Micromechatronics*. Marcel Dekker, Inc., 2003.

[32] B.L. Wang and J.C. Han. An analytical model for electrode-ceramic interaction in multilayer piezoelectric actuators. *Acta Mechanica Sinica/Lixue Xuebao*, 23(2):199 – 208, 2007.

[33] B. Yan, S.E. Prasad, R. Blacow, and D. Waechter. A linear high-voltage high-power amplifier for use with piezoelectric actuators. In *Proceedings of the 6th CanSmart Workshop SMART MATERIALS AND STRUCTURES*, 2003.

[34] Jiashi Yang. *An introduction to the theory of piezoelectricity*. Springer, 2005.